

# Global Biogeochemical Cycles®



## RESEARCH ARTICLE

10.1029/2022GB007644

### Key Points:

- Sulfide oxidation sources approximately 80% of dissolved  $\text{SO}_4^{2-}$  in the Koyukuk River, Alaska, and may act as a positive feedback on modern warming
- Inversion calculations reveal weathering is a  $\text{CO}_2$  sink on timescales of ~5–10 kyr and a  $\text{CO}_2$  source on timescales of ~10 kyr to ~10 Myr
- Increases in the absolute and relative abundance of  $\text{SO}_4^{2-}$  in the Koyukuk River and Yukon River over the past decades suggests thaw-induced sulfide oxidation

### Supporting Information:

Supporting Information may be found in the online version of this article.

### Correspondence to:

P. C. Kemeny,  
[preston.kemeny@gmail.com](mailto:preston.kemeny@gmail.com);  
[pkemeny@uchicago.edu](mailto:pkemeny@uchicago.edu)

### Citation:












Kemeny, P. C., Li, G. K., Douglas, M., Berelson, W., Chadwick, A. J., Dalleska, N. F., et al. (2023). Arctic permafrost thawing enhances sulfide oxidation. *Global Biogeochemical Cycles*, 37, e2022GB007644. <https://doi.org/10.1029/2022GB007644>

Received 9 NOV 2022  
 Accepted 19 SEP 2023

### Author Contributions:

**Conceptualization:** Preston Cosslett Kemeny, Woodward W. Fischer, A. Joshua West  
**Data curation:** Preston Cosslett Kemeny  
**Formal analysis:** Preston Cosslett Kemeny  
**Funding acquisition:** Michael P. Lamb, Woodward W. Fischer, A. Joshua West

## Arctic Permafrost Thawing Enhances Sulfide Oxidation

Preston Cosslett Kemeny<sup>1,2</sup> , Gen K. Li<sup>2,3</sup> , Madison Douglas<sup>2</sup> , William Berelson<sup>4</sup>, Austin J. Chadwick<sup>2</sup> , Nathan F. Dalleska<sup>2</sup> , Michael P. Lamb<sup>2</sup>, William Larsen<sup>5</sup> , John S. Magyar<sup>2</sup> , Nick E. Rollins<sup>4</sup>, Joel Rowland<sup>6</sup> , M. Isabel Smith<sup>4</sup> , Mark A. Torres<sup>5</sup> , Samuel M. Webb<sup>7</sup>, Woodward W. Fischer<sup>2</sup>, and A. Joshua West<sup>4</sup> 

<sup>1</sup>Department of the Geophysical Sciences, The University of Chicago, Chicago, IL, USA, <sup>2</sup>Division of Geological and Planetary Sciences, California Institute of Technology, Pasadena, CA, USA, <sup>3</sup>Department of Earth Science, University of California Santa Barbara, Santa Barbara, CA, USA, <sup>4</sup>Department of Earth Sciences, University of Southern California, Los Angeles, CA, USA, <sup>5</sup>Department of Earth, Environmental, and Planetary Sciences, Rice University, Houston, TX, USA, <sup>6</sup>Earth and Environmental Sciences Division, Los Alamos National Laboratory, Los Alamos, NM, USA, <sup>7</sup>Stanford Synchrotron Radiation Lightsource, SLAC National Accelerator Laboratory, Menlo Park, CA, USA

**Abstract** Permafrost degradation is altering biogeochemical processes throughout the Arctic.

Thaw-induced changes in organic matter transformations and mineral weathering reactions are impacting fluxes of inorganic carbon (IC) and alkalinity (ALK) in Arctic rivers. However, the net impact of these changing fluxes on the concentration of carbon dioxide in the atmosphere ( $p\text{CO}_2$ ) is relatively unconstrained. Resolving this uncertainty is important as thaw-driven changes in the fluxes of IC and ALK could produce feedbacks in the global carbon cycle. Enhanced production of sulfuric acid through sulfide oxidation is particularly poorly quantified despite its potential to remove ALK from the ocean-atmosphere system and increase  $p\text{CO}_2$ , producing a positive feedback leading to more warming and permafrost degradation. In this work, we quantified weathering in the Koyukuk River, a major tributary of the Yukon River draining discontinuous permafrost in central Alaska, based on water and sediment samples collected near the village of Huslia in summer 2018. Using measurements of major ion abundances and sulfate ( $\text{SO}_4^{2-}$ ) sulfur ( $^{34}\text{S}/^{32}\text{S}$ ) and oxygen ( $^{18}\text{O}/^{16}\text{O}$ ) isotope ratios, we employed the MEANDIR inversion model to quantify the relative importance of a suite of weathering processes and their net impact on  $p\text{CO}_2$ . Calculations found that approximately 80% of  $\text{SO}_4^{2-}$  in mainstem samples derived from sulfide oxidation with the remainder from evaporite dissolution. Moreover,  $^{34}\text{S}/^{32}\text{S}$  ratios,  $^{13}\text{C}/^{12}\text{C}$  ratios of dissolved IC, and sulfur X-ray absorption spectra of mainstem, secondary channel, and floodplain pore fluid and sediment samples revealed modest degrees of microbial sulfate reduction within the floodplain. Weathering fluxes of ALK and IC result in lower values of  $p\text{CO}_2$  over timescales shorter than carbonate compensation ( $\sim 10^4$  yr) and, for mainstem samples, higher values of  $p\text{CO}_2$  over timescales longer than carbonate compensation but shorter than the residence time of marine  $\text{SO}_4^{2-}$  ( $\sim 10^7$  yr). Furthermore, the absolute concentrations of  $\text{SO}_4^{2-}$  and  $\text{Mg}^{2+}$  in the Koyukuk River, as well as the ratios of  $\text{SO}_4^{2-}$  and  $\text{Mg}^{2+}$  to other dissolved weathering products, have increased over the past 50 years. Through analogy to similar trends in the Yukon River, we interpret these changes as reflecting enhanced sulfide oxidation due to ongoing exposure of previously frozen sediment and changes in the contributions of shallow and deep flow paths to the active channel. Overall, these findings confirm that sulfide oxidation is a substantial outcome of permafrost degradation and that the sulfur cycle responds to permafrost thaw with a timescale-dependent feedback on warming.

## 1. Introduction

Perennially frozen sediment or bedrock with variable ice content, called permafrost, underlies 15% of land in the Northern Hemisphere and is currently warming and thawing in many locations (Biskaborn et al., 2019; Hinzman et al., 2005; Lachenbruch & Marshall, 1986; Obu, 2021; Osterkamp & Romanovsky, 1999; Serreze et al., 2000). Permafrost degradation manifests as warming and thickening of the active layer (Anisimov et al., 1997; Brown et al., 2000; Hinkel & Nelson, 2003; Jiang et al., 2012; Nelson et al., 2021; Shiklomanov et al., 2012; Streletskiy et al., 2008; Yi et al., 2018), which is the layer of annual thaw overlying the perennially frozen ground. Active layer deepening is changing the hydrology of Arctic landscapes (Bense et al., 2009; Lamontagne-Hallé et al., 2018; Walvoord & Kurylyk, 2016; Walvoord & Striegl, 2007; Woo, 1986) and the ecological and biogeochemical regimes that they support (Frey & McClelland, 2009; Jorgenson et al., 2001, 2006, 2013; O'Donnell et al., 2012; Osterkamp et al., 2000). Biotic and inorganic feedbacks throughout permafrost environments can exacerbate or mitigate landscape

© 2023. The Authors.

This is an open access article under the terms of the [Creative Commons Attribution-NonCommercial-NoDerivs License](https://creativecommons.org/licenses/by/4.0/), which permits use and distribution in any medium, provided the original work is properly cited, the use is non-commercial and no modifications or adaptations are made.

**Investigation:** Preston Cosslett Kemeny, Gen K. Li, Madison Douglas, William Berelson, Austin J. Chadwick, Nathan F. Dalleska, Michael P. Lamb, William Larsen, John S. Magyar, Nick E. Rollins, Joel Rowland, M. Isabel Smith, Mark A. Torres, Samuel M. Webb, Woodward W. Fischer, A. Joshua West

**Methodology:** Preston Cosslett Kemeny

**Software:** Preston Cosslett Kemeny

**Supervision:** Woodward W. Fischer, A. Joshua West

**Validation:** Preston Cosslett Kemeny

**Visualization:** Preston Cosslett Kemeny

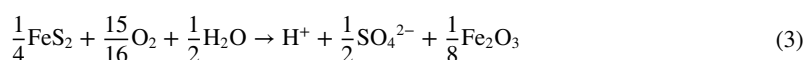
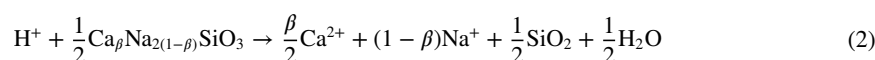
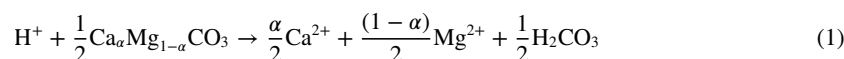
**Writing – original draft:** Preston Cosslett Kemeny

**Writing – review & editing:** Preston Cosslett Kemeny, Gen K. Li, Madison Douglas, William Berelson, Austin J. Chadwick, Nathan F. Dalleska, Michael P. Lamb, William Larsen, John S. Magyar, Nick E. Rollins, Joel Rowland, M. Isabel Smith, Mark A. Torres, Samuel M. Webb, Woodward W. Fischer, A. Joshua West

changes by impacting fluxes of greenhouse gases such as carbon dioxide (atmospheric partial pressure expressed as  $p\text{CO}_2$ ) and methane ( $\text{CH}_4$ ) (Grosse et al., 2016; Schuur et al., 2015). A wide range of biogeochemical processes are relevant for considering the response of landscapes and biogeochemical cycles to permafrost degradation (Tank et al., 2023), including gas emissions following organic carbon ( $\text{C}_{\text{org}}$ ) transformations (Billings et al., 1982; Koven et al., 2013; Oechel et al., 1993; Reeburgh & Whalen, 1992; Schuur et al., 2008, 2009, 2013), changes in the length of the growing season or type of vegetation (Aurela et al., 2004; Heijmans et al., 2022; Myneni et al., 1997; Sturm et al., 2001; Waelbroeck et al., 1997; Walker et al., 2006), shifts in the surface energy budget (Chapin et al., 2005; Randerson et al., 2006), and changes in the rate of river migration (Douglas et al., 2022; Ielpi et al., 2023; Rowland et al., 2023). Overall, the joint impact of such processes will determine where, and for what duration, permafrost degradation will act as a positive or negative feedback on climate change (Koven et al., 2011). While it previously seemed that ecological feedbacks might result in net carbon storage over the coming decades (Abbott et al., 2016; McGuire et al., 2018; Schuur et al., 2015), this prediction has been complicated by new research into abrupt thaw such as thermokarst formation (Olefeldt et al., 2016; Turetsky et al., 2020; Zolcos et al., 2018, 2019) and evidence that emissions can rapidly outpace biomass accumulation in certain circumstances (Schuur et al., 2021).

Many studies have focused on understanding and quantifying the fate of the approximately 1,500 Pg of organic carbon stored in northern deposits (Canadell et al., 2021; Miner et al., 2022). However, the impact of landscape transformations on  $p\text{CO}_2$  also depends on the flux of alkalinity (ALK) into Earth's ocean-atmosphere system. Formally a titration, ALK reflects the negative charge taken up by dissolved carbon and other acids and is often approximated as the difference between the charge-equivalent sums of major cations and anions (Zeebe & Wolf-Gladrow, 2001). Because shifts in the ratio of ocean ALK to ocean-atmosphere inorganic carbon (IC) can repartition carbon between the oceans and atmosphere, the flux ratio of landscape-derived ALK to landscape-derived IC ( $\Delta\text{ALK}/\Delta\text{IC}$ ) impacts  $p\text{CO}_2$  (Broecker & Sanyal, 1998; Hilton & West, 2020). Note that here we use  $\Delta\text{IC}$  to refer to changes in the sum of atmospheric  $\text{CO}_2$  and dissolved inorganic carbon (DIC), analogous to the use of  $\Delta\text{DIC}$  in prior studies (Kemeny & Torres, 2021; Kemeny et al., 2021a; Torres et al., 2016), in order to reduce confusion between the in situ DIC of particular water samples and the calculated impact of chemical weathering on the total IC content of the ocean-atmosphere system. Modern  $p\text{CO}_2$  is relatively insensitive to equal changes in marine ALK and DIC, meaning that sets of landscape processes that lead to  $\Delta\text{ALK} \approx \Delta\text{IC}$  will, on short timescales, impact the total amount of carbon in the ocean-atmosphere system without altering  $p\text{CO}_2$ . Understanding the impact of warming and landscape change on processes that generate or consume ALK is a major knowledge gap for predicting and modeling permafrost carbon-climate feedbacks (Drake et al., 2018b; Frey & McClelland, 2009; Kang et al., 2022; Tank et al., 2012a, 2012b, 2016, 2023; Toohey et al., 2016).

Weathering of carbonate minerals is a major source of dissolved cations to the Yukon River Basin (Brabets et al., 2000) and produces ALK and IC in a 2:1 ratio (Equation 1, with  $\alpha$  as a compositional constant). The weathering of silicate minerals, important in certain tributaries of the Yukon River (Kang et al., 2022), generates ALK without producing IC (Equation 2, with  $\beta$  as a compositional constant). The production of sulfuric acid ( $\text{H}_2\text{SO}_4$ ) through weathering of sulfur-bearing minerals such as pyrite ( $\text{FeS}_2$ ) removes ALK from the ocean-atmosphere system without impacting IC (Equation 3). Here we follow standard convention and use “sulfide oxidation” to refer to chemical weathering processes that release  $\text{SO}_4^{2-}$  and consume ALK, such as the oxidation of pyrite, but note that “sulfuric acid production” is more accurate because atmospheric  $p\text{CO}_2$  is impacted by release of  $\text{SO}_4^{2-}$  without a partner cation rather than by the oxidation itself (Kemeny et al., 2021a). Aerobic oxidation of organic carbon (Equation 4) and organic sulfur ( $\text{S}_{\text{org}}$ ) to  $\text{CO}_2$  and  $\text{SO}_4^{2-}$  impacts ALK and IC in a ratio dependent on the stoichiometry of the organic matter. If silicate and carbonate weathering are enhanced through permafrost degradation, the associated ALK fluxes would offset a portion of  $\text{CO}_2$  emissions from  $\text{C}_{\text{org}}$  oxidation. In contrast, increases in  $\text{C}_{\text{org}}$  oxidation or  $\text{H}_2\text{SO}_4$  production could act as a positive feedback on rising  $p\text{CO}_2$  by increasing IC or by removing ALK from the ocean-atmosphere system, respectively.



The relative abundance of chemical weathering products in rivers can be used to infer the types and magnitudes of the weathering reactions happening in their catchments, the net  $\Delta\text{ALK}/\Delta\text{IC}$  ratio of weathering, and the timescale-dependent impacts of weathering on  $p\text{CO}_2$  (Gaillardet et al., 1999; Garrels & Mackenzie, 1967; Kemeny & Torres, 2021; Négrel et al., 1993). Chemical weathering fluxes only impact  $p\text{CO}_2$  for the duration over which the landscape-produced ALK and IC fluxes remain in the ocean-atmosphere system. For example, on timescales longer than  $\sim 5\text{--}10$  kyr, the characteristic timescale presumed for carbonate compensation (Archer et al., 1997), the impact of carbonate weathering is reversed through the production and burial of marine carbonate. The timescale for the impact of sulfide oxidation to be reversed is often assumed to be the approximately 10 Myr residence time of modern sulfate ( $\text{SO}_4^{2-}$ ), although this value should be viewed cautiously due to long-term increases in the concentration of marine  $\text{SO}_4^{2-}$  and our developing understanding of linkages between marine  $\text{SO}_4^{2-}$  concentration and output fluxes (Lerman et al., 2007; Lowenstein et al., 2003; Spence & Telmer, 2005; Torres et al., 2014).

Several lines of evidence suggest an important role for changing sulfur fluxes in Arctic rivers. At a  $C_{\text{org}}/S$  molar ratio of 337, the median value for the sediment samples we report here, the 1,500 Pg  $C_{\text{org}}$  in high-latitude deposits would constitute  $\sim 370$  Tmol S, a large reservoir. Within the Yukon River Basin, Toohey et al. (2016) suggested that sulfuric acid production increased between 1982 and 2014 based on observations of increasing fluvial  $\text{SO}_4^{2-}$  fluxes. Without constraints from  $\text{SO}_4^{2-}$   $^{34}\text{S}/^{32}\text{S}$  and  $^{18}\text{O}/^{16}\text{O}$  isotope ratios, however, Toohey et al. (2016) could not determine whether the rising  $\text{SO}_4^{2-}$  fluxes resulted from enhanced sulfide oxidation or from enhanced dissolution of evaporite deposits (Burke et al., 2018; Burt et al., 2021; Calmels et al., 2007; Relph et al., 2021; van Stempvoort et al., 2023). In the Mackenzie River, Zolkos et al. (2018) identified extensive sulfide oxidation associated with the development of thermokarst. These prior studies establish that permafrost deposits can be a substantial reservoir of sulfur vulnerable to transformation under a warming climate and motivate additional research into the relationships among permafrost thaw, sulfide oxidation, and  $p\text{CO}_2$ .

Here we expand on such prior research by reporting a suite of geochemical observations in water and sediment samples collected from sites along the Koyukuk River, a major tributary to the Yukon River that drains discontinuous permafrost in central Alaska (Brabets et al., 2000; Obu et al., 2019). To distinguish among chemical weathering reactions and microbial transformations, as well as to quantify the impacts of weathering on  $p\text{CO}_2$ , we measured the concentrations of calcium ( $\text{Ca}^{2+}$ ), magnesium ( $\text{Mg}^{2+}$ ), sodium ( $\text{Na}^+$ ), potassium ( $\text{K}^+$ ), chloride ( $\text{Cl}^-$ ),  $\text{SO}_4^{2-}$ , DIC, and dissolved organic carbon (DOC) in river water, as well as sulfate  $^{34}\text{S}/^{32}\text{S}$  ( $\delta^{34}\text{S}_{\text{SO}_4}$ ), sulfate  $^{18}\text{O}/^{16}\text{O}$  ( $\delta^{18}\text{O}_{\text{SO}_4}$ ), water  $^{18}\text{O}/^{16}\text{O}$  ( $\delta^{18}\text{O}_{\text{H}_2\text{O}}$ ), water D/H ( $\delta\text{D}_{\text{H}_2\text{O}}$ ), DIC  $^{13}\text{C}/^{12}\text{C}$  ( $\delta^{13}\text{C}_{\text{DIC}}$ ), DOC  $^{13}\text{C}/^{12}\text{C}$  and  $^{14}\text{C}$  activity ( $\delta^{13}\text{C}_{\text{DOC}}$  and  $F_{\text{mod-DOC}}$ ), and sediment  $^{34}\text{S}/^{32}\text{S}$  ( $\delta^{34}\text{S}_{\text{sediment}}$ ), in addition to sulfur X-ray absorption spectra. We used the MEANDIR inversion model to quantify contributions to river solutes from distinct weathering processes and to calculate the  $\Delta\text{ALK}/\Delta\text{IC}$  ratio of chemical weathering (Kemeny & Torres, 2021). Finally, we compared our measurements against historical observations from the Koyukuk River and the Yukon River to evaluate how the relative importance of weathering processes has changed over the preceding decades.

## 2. Methods

### 2.1. Field Methods

#### 2.1.1. Field Sites and Hydrographic Context

We collected water and sediment samples from the Koyukuk River and its floodplain between 28 June and 9 July 2018, with sampling focused near the village of Huslia (Figure 1; Figure S1 for drone imagery in Supporting Information S1). The Koyukuk River catchment comprises 10.9% of the Yukon River catchment by drainage area and contributes 12% of discharge at Pilot Station (Brabets et al., 2000). Near Huslia, the Koyukuk River is a single-threaded channel that meanders through discontinuous permafrost with a mean depth of 12.4 m and an average width of about 250 m (Figure 1d). The mean width of the Koyukuk River has remained relatively constant since at least 1978 (Rowland et al., 2019), and the region surrounding Huslia was unglaciated throughout the last ice age. Fluvial landforms comprise the floodplain, including scroll bar levees, oxbow lakes, sloughs, and km-scale meanders in the active channel (Figure 1d and Figure S1 in Supporting Information S1). Exposures of undercut banks provide evidence of permafrost, which was confirmed during fieldwork through identification of frozen sediment and ice lenses within sediment cores (Douglas et al., 2021, 2022). Permafrost in scroll bar deposits is likely to be epigenetic (Drury, 1956; Mann et al., 1995), while permafrost within oxbow lakes,



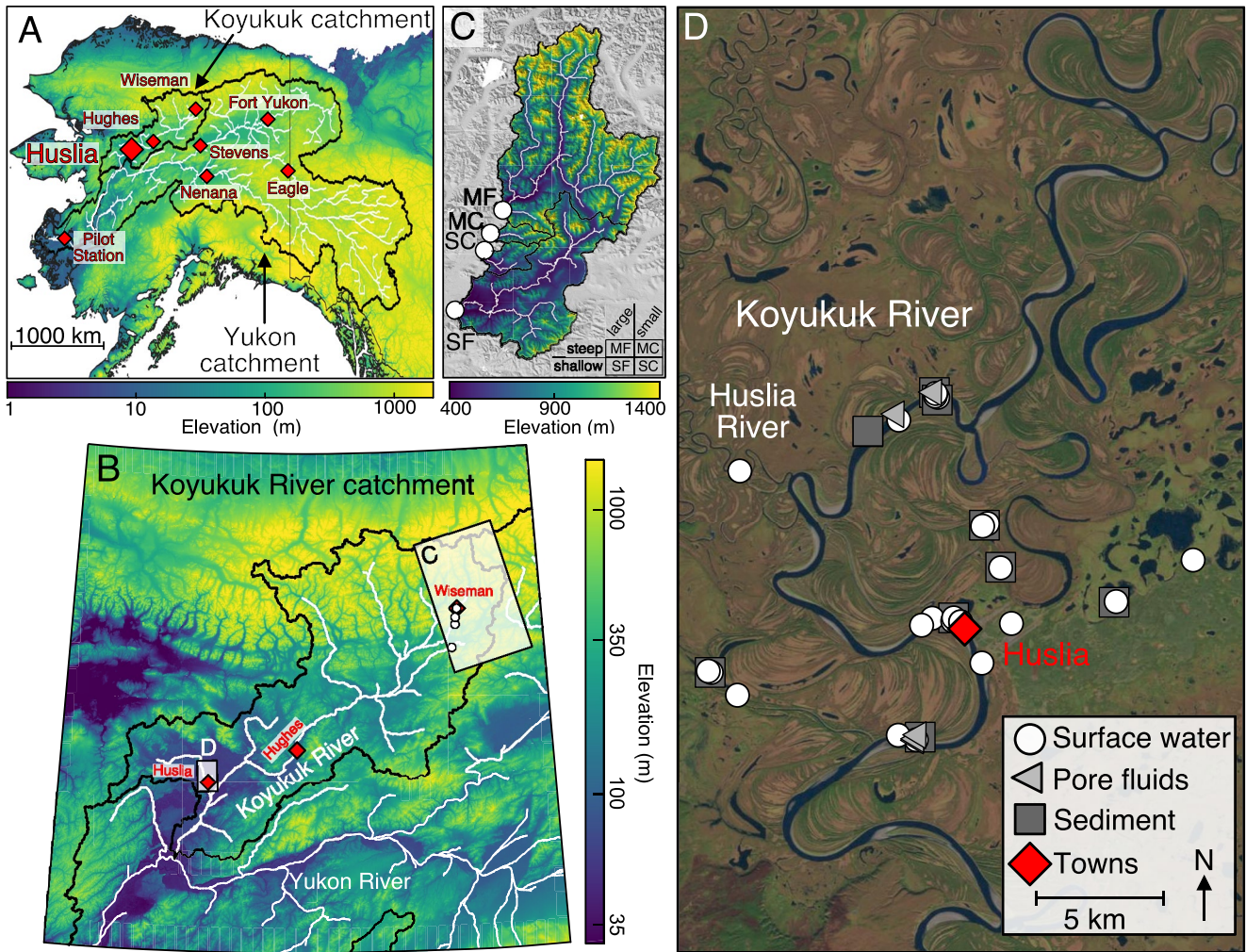


**Figure 1.** Site context and sample maps. (a) The Koyukuk River is a major tributary to the Yukon River within central Alaska. Sampling was focused near the village of Huslia (large red diamond), and data were compared with prior observations at United States Geological Survey (USGS) sites (small red diamonds). (b) The Koyukuk River catchment with indicated locations of Huslia, Hughes, and Wiseman. (c) The Middle Fork (MF), Marion Creek (MC), Slate Creek (SC), and South Fork (SF) headwater catchments vary in size and steepness. (d) Locations of water samples (circles), pore fluid (triangles), and sediment samples (squares) collected near Huslia. Sediment samples include both permafrost and non-permafrost deposits. Elevation data are (a) ASTER GDEM V2 (EPSG: 4087), (b) USGS NED Digital Surface Model (EPSG: 3338), and (c) Arctic DEM from the Polar Geospatial Center (EPSG: 3413). Panel (d) is a Global Land Survey image (EPSG: 32605).

thermocarst lakes, or the shallow section of peat bogs may more often be syngenetic (Jorgenson et al., 2020; Kanevskiy et al., 2014; Kreig & Reger, 1982). Drone and satellite-based optical images did not show evidence of extensive ground collapse features in the Huslia area. Excess ground ice and thermocarst is present on relatively older terrain that preferentially occurs away from the active river channel; the hydrological connectivity between this older terrain and the active river is largely unconstrained.

We measured water discharge five times over the course of the field campaign by performing three to fourteen bank-to-bank transects across the Koyukuk River using a Teledyne Riopro Acoustic Doppler Current Profiler. Discharge declined from about 2,390 m<sup>3</sup>/s to about 1,220 m<sup>3</sup>/s over the course of the field campaign (Figure 2a). This decrease was corroborated by pressure sensor measurements, which tracked a 1.9 m decline in river stage over the same duration. We compared the discharge observations to those at Hughes, located on the Koyukuk River ~260 km along-river distance northeast of Huslia, where daily or monthly discharge measurements made by the United States Geological Survey (USGS) are available (Figure 2b). Discharge at Hughes is typically very low from November through April, increases sharply in May and June with the spring freshet, and remains elevated throughout July, August, and September. Based on these nearby historical data, we inferred that samples



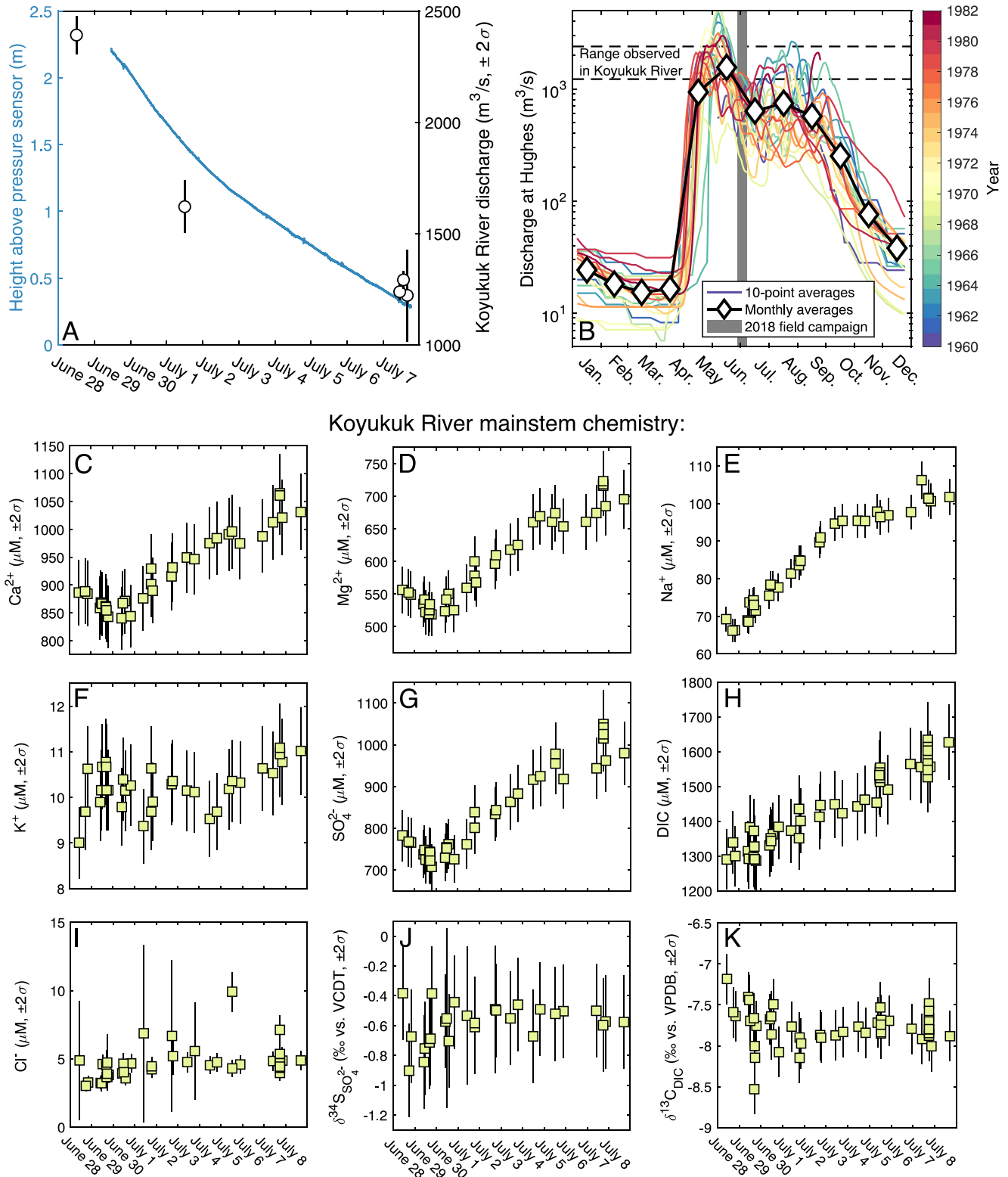


**Figure 2.** Discharge and major ion concentrations in the Koyukuk River. (a) River stage (blue curve) and measured discharge (black symbols) during the 2018 fieldwork. (b) Discharge at Hughes between 1960 and 1982 with monthly averages (diamonds connected by thick black lines) and 10-point moving averages color-coded by year (rainbow curves). Discharge was typically highest in May and June, elevated throughout July, August, and September, and low from October through April. Measured (c)  $\text{Ca}^{2+}$ , (d)  $\text{Mg}^{2+}$ , (e)  $\text{Na}^+$ , (f)  $\text{K}^+$ , (g)  $\text{SO}_4^{2-}$ , (h) DIC, (i)  $\text{Cl}^-$ , (j)  $\delta^{34}\text{S}_{\text{SO}_4}$ , and (k)  $\delta^{13}\text{C}_{\text{DIC}}$  in mainstem samples. The concentrations of  $\text{Ca}^{2+}$ ,  $\text{Mg}^{2+}$ ,  $\text{Na}^+$ ,  $\text{SO}_4^{2-}$ , and DIC increased with declining discharge over the course of the field campaign.

collected from the Koyukuk River in late June and early July represent flow conditions on the falling arm of the freshet and prior to the full seasonal thaw of the active layer.

One year later, in August 2019, we collected water samples from the Middle Fork (MF), South Fork (SF), Marion Creek (MC), and Slate Creek (SC) sites near Wiseman, AK, ~650 km along-river distance northeast of Huslia within the headwaters of the Koyukuk River (Figures 1b and 1c). These headwater catchments consisted of bedrock streams with sediment primarily supplied by alluvial fans in the Brooks Range. The streams did not have wide floodplains and we identified permafrost in the eroding banks of the MF site. The catchment areas upstream of the MF (3,207 km<sup>2</sup>) and SF (1,838 km<sup>2</sup>) sample sites are substantially larger than those upstream of the MC (128 km<sup>2</sup>) and SC (191 km<sup>2</sup>) sample sites, while the median slopes of the catchment upstream of the MF (20.8°) and the MC (24.1°) sample sites are much higher than those of the SF (10.7°) and SC (11.2°) sample sites. No pore fluid or sediment samples were collected near the headwaters.

The headwaters of the Koyukuk River in the Brooks Range drain an upper crustal assemblage of lithologies including Paleozoic-Precambrian metasediments, Jurassic-Devonian mafic volcanic and intrusive rocks, Cretaceous shale, siltstone, metasediment, and granite, and assorted carbonates (Beikman, 1980; Harrison et al., 2011; Patton et al., 2009; Till et al., 2008; Wilson et al., 2015). The geologic map of Harrison et al. (2011) includes a Silurian-Devonian sedimentary unit containing evaporite horizons within the Brooks Range that is not recorded in other maps; the existence of evaporite minerals throughout the Yukon River Basin has previously been both observed and inferred (Brabets et al., 2000; Clautice & Mowatt, 1981). Even without surface exposure, weathering of subsurface evaporites could contribute to fluvial dissolved load. The Koyukuk River flows through Cretaceous shale and greywacke as it descends from the Brooks Range toward Huslia (Beikman, 1980) and through Cretaceous igneous lithologies near Hughes (Patton et al., 2009). The geology near Huslia is mapped as either Lower Cretaceous intermediate volcanic rock (Beikman, 1980) or Quaternary alluvial and eolian deposits (Patton et al., 2009; Wilson et al., 2015), and exposure of cross-stratified beds >3 m tall and interpreted to be aeolian were visible beneath the village (Wolfe et al., 2011). The Koyukuk River is currently reworking its own floodplain and bar deposits and no bedrock exposures were seen or sampled during the 2018 field campaign.

### 2.1.2. Sample Collection

Water sampling was primarily focused along the active channel ( $n = 49$ ) of the Koyukuk River, with additional samples collected from secondary channels ( $n = 5$ ) of the Koyukuk River and the active channel of the Huslia River ( $n = 4$ ). The secondary channels, which we will refer to as sloughs, are likely former channels of the Koyukuk River that have been partially abandoned through cutoff. Unlike features such as oxbow lakes, the sloughs generally retain upstream and downstream connections to the main channel. The sloughs mostly appeared to be flowing during the field campaign, albeit slowly relative to the active channel. To further constrain chemical weathering and sulfur cycling, water samples were also collected from lakes surrounding Huslia ( $n = 6$ ), from meteoric precipitation ( $n = 4$ ), from pore fluids drawn from bank and floodplain sediment ( $n = 19$ ), and from the Koyukuk River headwaters ( $n = 4$ ).

Twenty-four of the mainstem samples and all of the headwater, slough, and lake samples were surface waters collected into 50 mL plastic syringes that were sampled either from shore or onboard small boats. When possible, we used a Hydrolab multiprobe to measure the temperature, conductivity, and pH of water samples. The samples were filtered through 0.22  $\mu\text{m}$  porosity 25 mm diameter nylon syringe filters into MQ-washed 60 mL polypropylene bottles for anion analysis, acid-washed 60 mL polypropylene bottles for cation analysis, and two 12 mL Labco exetainer vials for DIC and water isotope analysis. Sample containers were rinsed with filtrate prior to collection and cation splits were acidified with two drops of 16 N high-purity nitric acid ( $\text{HNO}_3$ ). Additional samples for cation and anion analysis collected near an upstream confluence were filtered into exetainer vials instead of polypropylene bottles but were later determined to have substantial blanks and were excluded from further analyses (Figure S2 in Supporting Information S1). The four precipitation samples were collected into a bowl in Huslia, ~1.5 km inland of the mainstem river, and were syringe filtered.

In addition to the syringe-filtered samples, 25 mainstem Koyukuk River samples and the four samples from the Huslia River were collected as filtrate in the course of filtering water for suspended sediment analyses. For these samples, approximately 8 L of river water was collected using a Van Dorn sampler from either the river surface or from within the water column and temporarily stored in 10 L plastic bags. To accommodate different sampling objectives, the water was then passed through either a 0.2  $\mu\text{m}$  142 mm diameter nitrocellulose mixed ester (MCE) filter or a 0.2  $\mu\text{m}$  142 mm diameter polyethersulfone (PES) filters. MCE filters were used for all 25 mainstem samples and one sample from the Huslia River, and PES filters were used for the other three samples from the

Huslia River. MQ blanks collected for filtering with nylon and PES filters had negligible  $\text{SO}_4^{2-}$  concentrations and suggest no sulfur leaching from the PES filters. Sediment was later harvested from MCE and PES filters by sonicating them in MQ water and gently scraping with a spatula. Due to the potential sulfur contamination that can occur when scraping the PES filters, we report sulfur observations only for sediment harvested from MCE filters.

Filtrate from three mainstem, one lake, and one Huslia River sample was collected into five 1 L amber bottles for measurement of the  $^{14}\text{C}$  activity of DOC. The filtrate was acidified with 20 drops of high-purity HCl. Two of these mainstem samples were passed through PES filters and the other three samples through MCE filters.

Pore fluid samples of bank and floodplain sediment were collected using Rhizosphere Rhizon samplers with 0.15  $\mu\text{m}$  pore size. Most of these pore fluids ( $n = 14$ ) were collected from multiple depths  $<1$  m deep at three neighboring sites (Figure S6 in Supporting Information S1). The remaining pore fluids were collected from two additional sites on the bank of the active channel (Figure 1d). Samples for different chemical analyses were collected based on available volume, and cation splits were acidified with 16 N  $\text{HNO}_3$ .

Sediment samples were collected from the Koyukuk River banks and floodplain near Huslia to study sulfur and carbon cycling across the alluvial system (Figure 1d; Douglas et al., 2021, 2022). All sediment samples collected from each individual site were classified as permafrost when ice cement or ice lenses were visible and as non-permafrost when ice cement was not recovered to the depth of collection. Unfrozen cut banks and point bars were sampled by hand, cores were augered into unfrozen material, and we used a Snow, Ice, and Permafrost Research Establishment (SIPRE) corer when necessary. Sediment samples were stored in Whirlpak bags and kept frozen until processing. Previously, Douglas et al. (2021) reported observations of microbial community composition in a subset of these sediment samples and Douglas et al. (2022) reported stratigraphic sections and observations of grain size,  $\delta^{13}\text{C}_{\text{org}}$ , and  $^{14}\text{C}$  activity.

## 2.2. Laboratory Methods

### 2.2.1. Ion Chromatography Measurements

Major ion concentrations were measured by ion chromatography in the Resnick Water and Environment Laboratory at the California Institute of Technology. Concentrations of  $\text{Ca}^{2+}$ ,  $\text{Mg}^{2+}$ ,  $\text{Na}^+$ , and  $\text{K}^+$  were measured on a Dionex ICS-2000 with guard column (CG12A  $2 \times 50$  mm), separator column (CS12A  $2 \times 250$  mm), suppressed conductivity, and a 20 mM isocratic methanesulfonic acid eluent. Concentrations of  $\text{Cl}^-$  and  $\text{SO}_4^{2-}$  were measured on a Dionex ISC-3000 with guard column (AG29  $2 \times 50$  mm), separator column (AS29  $2 \times 250$  mm), suppressed conductivity, and an isocratic 4.5 mM  $\text{Na}_2\text{CO}_3/2.5$  mM  $\text{NaHCO}_3$  eluent. Measurement precision was quantified through replicate analysis of samples, the MAURI-09, SUPER-05, and CRANBERRY-05 reference materials from Environment and Climate Change Canada, and the in-house river water consistency standard Switzer Falls (Burke et al., 2018) (Table S1 in Supporting Information S1). Quantified as the least reproducible value across materials, the  $1\sigma$  precision of  $\text{SO}_4^{2-}$  (3.9%),  $\text{Mg}^{2+}$  (3.2%),  $\text{Na}^+$  (2.4%), and  $\text{K}^+$  (4.4%) were consistent with expectations (Table S1 in Supporting Information S1). Although the Relative Standard Deviation (RSD) of  $\text{Cl}^-$  measurements in SUPER-05 (2.1%) and MAURI-09 (7.3%) were also reasonable, the mean precision of  $\text{Cl}^-$  in replicate sample measurements was worse (14.4%) and likely reflects that the concentration of  $\text{Cl}^-$  is  $<10$   $\mu\text{M}$  in  $>90\%$  of the samples. The  $1\sigma$  RSD for  $\text{Ca}^{2+}$  was 3.3% in CRANBERRY-05 ( $n = 2$ ) and 12.1% in MAURI-09 ( $n = 3$ ), with a mean value of 1.1% across 15 sets of sample replicates with 2–3 measurements each. An anomalously poor  $\text{Ca}^{2+}$  precision was previously observed for MAURI-09 and does not appear to represent the precision of the  $\text{Ca}^{2+}$  concentration measurements. The precision of each major ion measurement was taken as the larger of replicate sample measurements or the least reproducible consistency standard for that element, excluding the  $\text{Ca}^{2+}$  measurements of MAURI-09. For comparison to measured DIC, the concentration of  $\text{HCO}_3^-$  was calculated as the charge-equivalent difference between the sum of  $\text{Ca}^{2+}$ ,  $\text{Mg}^{2+}$ ,  $\text{Na}^+$ , and  $\text{K}^+$  and the sum of  $\text{SO}_4^{2-}$  and  $\text{Cl}^-$ . Note that the following analyses reference both the sum of dissolved cations ( $\Sigma^+ = \text{Ca}^{2+} + \text{Mg}^{2+} + \text{Na}^+ + \text{K}^+$ , in charge equivalents) and the sum of dissolved cations and  $\text{SO}_4^{2-}$  ( $\Sigma^\pm = \Sigma^+ + \text{SO}_4^{2-}$ , in charge equivalents).

### 2.2.2. MC-ICP-MS Measurements of $\delta^{34}\text{S}_{\text{SO}_4}$

The  $^{34}\text{S}/^{32}\text{S}$  isotope ratio of dissolved  $\text{SO}_4^{2-}$  was measured to distinguish between  $\text{SO}_4^{2-}$  derived from sulfide oxidation and  $\text{SO}_4^{2-}$  derived from evaporite dissolution. The  $\delta^{34}\text{S}_{\text{SO}_4}$  values ( $^{34}\text{R}_{\text{sample}}/^{34}\text{R}_{\text{standard}} - 1$ , where  $^{34}\text{R}$  is the  $^{34}\text{S}/^{32}\text{S}$  ratio of  $\text{SO}_4^{2-}$  and  $\delta^{34}\text{S}$  is reported in ‰) of 56 water samples were measured by Multicollector Induc-



tively Coupled Plasma Mass Spectrometry (MC-ICP-MS; Neptune Plus) at the California Institute of Technology (Burke et al., 2018; Paris et al., 2013, 2014). Sample aliquots containing approximately 7.5–470 nmol  $\text{SO}_4^{2-}$  were evaporated within Savillex PFA vials,  $\text{SO}_4^{2-}$  was chromatographically isolated using AG 1-X8 anion exchange resin, column effluent was matrix matched to an in-house  $\text{Na}_2\text{SO}_4$  standard, and  $^{34}\text{S}/^{32}\text{S}$  ratios were measured as sets of 50 cycles with sample-standard bracketing. Anomalous  $^{34}\text{S}/^{32}\text{S}$  measurements were identified statistically ( $>3\sigma$ ) and removed from the analysis, as were individual cycles associated with large changes in signal strength and entire sets of cycles following substantial fluctuations in mass biasing. The standard deviation of error-normalized deviations ranged from 2.2 to 9.0 across six analytical sessions (John & Adkins, 2010). We report  $\delta^{34}\text{S}$  values using the means of  $^{34}\text{S}/^{32}\text{S}$  ratios corrected for both instrument blank and procedural blank, the latter of which averaged 0.44 nmol of  $\text{SO}_4^{2-}$ . Consistency standards included seawater, which was measured as having a  $\delta^{34}\text{S}_{\text{SO}_4}$  value of  $21.1 \pm 0.3\text{‰}$  ( $n = 34$ ,  $2\sigma$ ), and the in-house reference material Switzer Falls, which was measured as having a  $\delta^{34}\text{S}_{\text{SO}_4}$  value of  $4.2 \pm 0.2\text{‰}$  ( $n = 38$ ,  $2\sigma$ ) (Burke et al., 2018). Among 14 samples independently processed twice, the mean of twice the difference in  $\delta^{34}\text{S}$  between the two external replicates was 0.3‰. Overall, 16 samples were measured more than twice, 32 samples were measured twice, and 8 samples were measured only once. The precision of  $\text{SO}_4^{2-}$   $\delta^{34}\text{S}$  for each sample is reported as the larger of either the standard deviation of blank-corrected  $^{34}\text{S}/^{32}\text{S}$  determinations or the reproducibility of seawater ( $2\sigma = 0.3\text{‰}$ ).

### 2.2.3. IRMS Measurement of $\delta^{18}\text{O}_{\text{SO}_4}$

The  $^{18}\text{O}/^{16}\text{O}$  isotope ratio of dissolved  $\text{SO}_4^{2-}$  was also measured to distinguish  $\text{SO}_4^{2-}$  generated through sulfide oxidation from that sourced through dissolution of evaporites. The  $\delta^{18}\text{O}_{\text{SO}_4}$  values of 14 mainstem river, slough, headwater, and pore fluid water samples were measured at the Environmental Isotope Laboratory in the Department of Geosciences at the University of Arizona. Unacidified water samples were passed through a 0.45  $\mu\text{m}$  filter to remove particulates, HCl was added to prevent subsequent precipitation of  $\text{BaCO}_3$ , the solution was put on a hot plate, 0.5 M  $\text{BaCl}_2$  was added to induce precipitation of  $\text{BaSO}_4$ , the solution was passed through a second 0.45  $\mu\text{m}$  filter, the filter was dried, and  $\text{BaSO}_4$  was recovered by scratching the powder off the filter without digging into the underlying material. The recovered powder was combusted in a ThermoQuest Finnigan TC/EA at 1375°C in the presence of excess carbon, and the  $^{18}\text{O}/^{16}\text{O}$  ratio of produced CO was measured on a Thermo Electron Delta V mass spectrometer. Values of  $\delta^{18}\text{O}_{\text{SO}_4}$  were corrected to the VSMOW scale using an in-house barium sulfate standard, which was calibrated against NBS-127, and are reported with a precision of 0.8‰ ( $2\sigma$ ). Due to limited sample volumes (~50 mL), most samples did not contain sufficient  $\text{SO}_4^{2-}$  for recovery of  $\text{BaSO}_4$ , meaning that the  $\delta^{18}\text{O}_{\text{SO}_4}$  measurements only capture the isotopic signals of samples with high  $\text{SO}_4^{2-}$  concentrations.

### 2.2.4. Spectroscopic Measurements of Water $\delta^{18}\text{O}$ and $\delta\text{D}$

The  $^{18}\text{O}/^{16}\text{O}$  ratios of water samples were measured to estimate the  $\delta^{18}\text{O}$  of  $\text{SO}_4^{2-}$  formed during sulfide oxidation. Water  $\delta^{18}\text{O}$  and  $\delta\text{D}$  were measured using a Picarro cavity ring-down laser spectrometer at Rice University in July 2018. Instrument drift was corrected using an in-house standard analyzed throughout the run and a memory correction was performed following Van Geldern and Barth (2012). Measurements were calibrated using the international reference standards VSMOW2 and SLAP2, and reference materials included CIT17 ( $\delta^{18}\text{O} = -9.8 \pm 0.2\text{‰}$  ( $2\sigma$ );  $\delta\text{D} = -73.8 \pm 1.2\text{‰}$  ( $2\sigma$ )) and IA-R064 ( $\delta^{18}\text{O} = -12.3 \pm 0.3\text{‰}$  ( $2\sigma$ );  $\delta\text{D} = -98.3 \pm 2.3\text{‰}$  ( $2\sigma$ )). CIT17 was measured as having a  $\delta^{18}\text{O}$  value of  $-9.7 \pm 0.4\text{‰}$  ( $n = 6$ ,  $2\sigma$ ) and a  $\delta\text{D}$  value of  $-74.6 \pm 2.2\text{‰}$  ( $n = 6$ ,  $2\sigma$ ), and IA-R064 was measured as having  $\delta^{18}\text{O}$  of  $-12.4 \pm 0.2\text{‰}$  ( $n = 5$ ,  $2\sigma$ ) and  $\delta\text{D}$  of  $-97.6 \pm 1.2\text{‰}$  ( $n = 5$ ,  $2\sigma$ ). Sample precision was taken as the larger of the precision among repeated injections and the least reproducible  $\delta^{18}\text{O}$  and  $\delta\text{D}$  measurements of CIT17 and IA-R064 (0.4‰ ( $2\sigma$ ) for  $\delta^{18}\text{O}$  and 2.2‰ ( $2\sigma$ ) for  $\delta\text{D}$ ). Water isotope ratios were measured immediately after the 2018 field season; the  $\delta^{18}\text{O}$  and  $\delta\text{D}$  values of the four headwaters samples were not measured as they were collected opportunistically in 2019.

### 2.2.5. Spectroscopic Measurements of DIC and $\delta^{13}\text{C}$

The concentration and  $^{13}\text{C}/^{12}\text{C}$  ratio of DIC were measured to constrain the relative importance of carbonate weathering,  $\text{C}_{\text{org}}$  oxidation, and  $\text{CO}_2$  degassing. The DIC concentration and  $\delta^{13}\text{C}_{\text{DIC}}$  values of 61 samples were measured using a Picarro cavity ring-down laser spectrometer at the University of Southern California in August 2018 following the method of Subhas et al. (2015). Values of  $\delta^{13}\text{C}_{\text{DIC}}$  were calibrated to the VPDB scale using OPT Calcite ( $\delta^{13}\text{C} = 2.47\text{‰}$ , 12.002 wt% C) in the first analytical session and using AR-15 ( $\delta^{13}\text{C} = -9.65 \pm 0.03\text{‰}$ , 8.23  $\pm$  0.1 wt% C) in three subsequent sessions, while the concentration of DIC was calibrated using OPT

Calcite in all four analytical sessions. Both OPT-Calcite and AR-15 are in-house standards that were previously calibrated to the VPDB scale at UC Davis. When not being used as an accuracy standard, OPT Calcite was measured as having a  $\delta^{13}\text{C}$  value of  $2.4 \pm 0.3\text{‰}$  ( $n = 11, 2\sigma$ ). AR-15 was measured as having a carbon abundance of  $8.2 \pm 0.5 \text{ wt\%}$  ( $n = 20, 2\sigma$ ). The precision of  $\delta^{13}\text{C}_{\text{DIC}}$  measurements was taken as the reproducibility of OPT-calcite  $\delta^{13}\text{C}$  ( $0.3\text{‰}$ ,  $2\sigma$ ) and the precision of DIC concentration was reached through multiplying measured DIC concentration by the RSD of repeated AR-15 measurements ( $6.7\%$ ,  $2\sigma$ ).

### 2.2.6. Accelerator Mass Spectrometry Measurements of $\delta^{13}\text{C}_{\text{DOC}}$ and $F_{\text{mod-DOC}}$

The  $^{14}\text{C}$  activity and  $^{13}\text{C}/^{12}\text{C}$  ratio of DOC in five samples was measured to constrain the timescale over which  $\text{C}_{\text{org}}$  oxidation might impact  $p\text{CO}_2$ . The  $^{14}\text{C}$  activity and  $^{13}\text{C}/^{12}\text{C}$  ratio of DOC were measured at the Accelerator Mass Spectrometry Lab at the University of Arizona. Organic carbon was extracted at the AMS facility approximately 1 month after collection and processed following the method of Leonard et al. (2013). We report the  $^{13}\text{C}/^{12}\text{C}$  measurements as  $\delta^{13}\text{C}_{\text{DOC}}$  and the  $^{14}\text{C}$  measurements as fraction modern ( $F_{\text{mod-DOC}}$ ).

### 2.2.7. EA-IRMS Measurements of Sediment $\delta^{34}\text{S}$

The  $^{34}\text{S}/^{32}\text{S}$  ratio of sediment samples was measured to study sulfur cycling in the floodplain surrounding Huslia. The  $\delta^{34}\text{S}$  of 17 sediment samples from nine unique sites was measured at the California Institute of Technology across three analytical sessions during August 2020. Collected sediment samples were oven-dried, homogenized with agate mortar and pestle, and split by coning-and-quartering or in a riffle splitter (Douglas et al., 2022). The sediment was then weighed and burned in the presence of  $\text{V}_2\text{O}_5$  within a Thermo Flash Elemental Analyzer and the gas was directed through a Conflo-IV interface into a Thermo Delta V mass spectrometer. Samples were corrected for capsule blank and calibrated to the VCDT scale using IAEA-S1 and IAEA-S2. Overall, 11 samples were measured two times, five samples were measured three times, and the sample KY18-Bank1-Peat was measured six times. The precision of sediment  $\delta^{34}\text{S}$  was taken as the larger of either repeat  $\delta^{34}\text{S}$  determinations or the precision of sample KY18-Bank1-Peat, which was measured as having a  $\delta^{34}\text{S}$  value of  $1.6 \pm 0.5\text{‰}$  ( $n = 6, 2\sigma$ ). The sulfur abundance of sediment ranged from 0.023 wt% to 0.176 wt%. The precision of sulfur abundance measurements was taken as the larger of either repeat determinations or the 17% RSD of repeated KY18-Bank1-Peat measurements ( $0.176 \pm 0.03 \text{ wt\%}$ ,  $n = 6, 2\sigma$ ).

### 2.2.8. X-Ray Absorption Near-Edge Structure Measurements

X-ray Absorption Near-Edge Structure (XANES) spectroscopy provided  $\mu\text{m}$ -scale information on the redox state and electronic structure of sulfur in samples of floodplain and suspended sediment. XANES measurements across the sulfur K-edge were conducted on beamline 14-3 of the Stanford Synchrotron Radiation Lightsource at the SLAC National Accelerator Laboratory during four analytical sessions between February 2019 and March 2020. The energy of the incident X-ray beam was obtained using a Si(111) crystal in the monochromator and calibrated by defining the first pre-edge feature of sodium-thiosulfate at 2,472.02 eV. Fluorescence from the sample was monitored using a 4-element Vortex Si drift detector (Hitachi) using Xspress3 pulse processing electronics (Quantum Detectors). Samples were prepared by inverting sediment vials onto sulfur-free mylar tape, which was then covered with mylar film, secured to sample trays, and mounted inside a helium-purged chamber.

Our workflow consisted of first mapping a region of each sample at an incident energy at or above the sulfur K-edge at relatively coarse resolution to identify areas of high sulfur abundance, and then either collecting spectra at those positions or further characterizing interesting regions through high-resolution mapping at multiple incident energies characteristic of the resonances of specific sulfur moieties. In turn, a principal component analysis of the resulting maps was used to identify areas of spectral diversity that were then targeted for collection of complete spectra. The normalized fluorescence signals of 1–3 replicate spectra were averaged and baseline corrected using the program SIXPACK (Webb, 2005, 2020). Spectra collected on floodplain sediment are likely representative of the sample as they were homogenized prior to analysis, while spectra collected on suspended sediment might be biased as the sediment was not homogenized after harvesting from filters. Spectra from 96 positions were collected, but 12 of the 43 spectra on suspended sediment and 9 of the 53 spectra on floodplain sediment were removed from the analysis because they exhibited substantial baseline noise indicative of low sulfur abundance. The remaining 75 spectra, collected from six unique suspended sediment samples and 8 unique deposit samples, were fit to five transmission reference spectra from the European Synchrotron Radiation Facility ID21 sulfur XANES spectra database: oxidized glutathione (disulfide), cysteine (thiol), methionine sulfoxide (sulfoxide), taurine (sulfonate), and anhydrite (sulfate) (Bohic et al., 2008). The fitting was performed

**Table 1**  
*Parameters for the Three End-Member Isotope Mass Balance Model Used to Calculate the  $\delta^{18}\text{O}$  of Sulfuric Acid Produced During Sulfide Oxidation and the  $\delta^{34}\text{S}$  of Sulfuric Acid Sources*

Calculation variable	Minimum	Maximum	Reference
Gypsum $\delta^{34}\text{S}_{\text{SO}_4}$	10‰	30‰	Claypool et al. (1980)
Gypsum $\delta^{18}\text{O}_{\text{SO}_4}$	10‰	20‰	Claypool et al. (1980)
Precipitation $\text{SO}_4^{2-}/\text{Cl}^-$ ( $\mu\text{M}/\mu\text{M}$ )	0.07	1.21	Measured
Precipitation $\delta^{34}\text{S}_{\text{SO}_4}$	3.8‰	6.7‰	Measured
Precipitation $\delta^{18}\text{O}_{\text{SO}_4}$	8.3‰	9.1‰	Lloyd (1967), Waldeck et al. (2019)
$\delta^{18}\text{O}$ of $\text{O}_2$ consumed during oxidation reaction	23.5‰	70‰	Kim et al. (2017), Relph et al. (2021)
Fraction $\text{O}_2$ -derived oxygen	0%	25%	Balci et al. (2007), Killingsworth et al. (2018), Burt et al. (2021)
Oxygen isotope fractionation between $\text{SO}_4^{2-}$ and $\text{O}_2$ : $\epsilon_{\text{SO}_4-\text{O}_2}$	-11.4‰	-8.7‰	Lloyd (1968), Taylor et al. (1984b), Balci et al. (2007)
Oxygen isotope fractionation between $\text{SO}_4^{2-}$ and $\text{H}_2\text{O}$ : $\epsilon_{\text{SO}_4-\text{H}_2\text{O}}$	0‰	4.1‰	Taylor et al. (1984b), van Everdingen and Krouse (1985), Balci et al. (2007)

*Note.* We used measured values for the mean and standard deviation of sample  $\delta^{34}\text{S}_{\text{SO}_4}$ ,  $\delta^{18}\text{O}_{\text{SO}_4}$ , and  $\delta^{18}\text{O}_{\text{H}_2\text{O}}$ , as well as for precipitation  $\delta^{34}\text{S}_{\text{SO}_4}$  and  $\text{SO}_4^{2-}/\text{Cl}^-$ . For headwater samples lacking measurements of  $\delta^{18}\text{O}_{\text{H}_2\text{O}}$  we used the mean and standard deviation of  $\delta^{18}\text{O}_{\text{H}_2\text{O}}$  in mainstem samples. The  $\delta^{18}\text{O}_{\text{SO}_4}$  of precipitation was assumed to equal marine  $\delta^{18}\text{O}_{\text{SO}_4}$ .

in MATLAB as an optimization to minimize proportional misfit, with the contributions from reference spectra constrained to be positive and without constraint on their sum, and with equal weighting for all points between 2,470 eV and 2,490 eV where the relative fluorescence response was  $\geq 0.1$  (Manceau & Nagy, 2012; Priezel et al., 2011). The normalized fractional contributions of the disulfide, thiol, and sulfoxide reference spectra were then summed to reach the statistic  $F_{\text{red}}$ , which approximately reflects the fractional importance of reduced sulfur moieties to each spectrum (Kemeny et al., 2021b; Torres et al., 2020).

### 2.3. Data Analyses

#### 2.3.1. Thermodynamic Calculations in PHREEQC

We performed three thermodynamic calculations of aqueous carbon speciation using PHREEQC version 3 for macOS with the phreeqc.dat database (Parkhurst & Appelo, 2013). First, we calculated the equilibrium  $\text{CO}_2$  concentration for each river water sample at an atmospheric  $p\text{CO}_2$  of 410 ppm and measured temperature. Second, we calculated DIC speciation for each sample at the measured temperature and pH and compared in situ  $\text{CO}_2$  to the equilibrium value. The in situ  $\text{CO}_2$  concentration exceeded the equilibrium  $\text{CO}_2$  concentration in most samples and motivated including degassing within inversion calculations. We then calculated the  $\delta^{13}\text{C}$  of  $\text{CO}_2$ ,  $\text{HCO}_3^-$ , and  $\text{CO}_3^{2-}$  within each sample using the fractionation factors of Mook (1986) and took the difference between calculated  $\delta^{13}\text{C}_{\text{CO}_2}$  and measured  $\delta^{13}\text{C}_{\text{DIC}}$  as the range of allowable degassing fractionation factors within the inversion calculations. Third, we calculated the amount of DIC that must be added to each sample to decrease pH to 5.0 or 6.0 without the addition or removal of any major ions. This DIC must be added in the form of  $\text{CO}_2$  as we held ALK constant and thus established, for a given initial pH, an approximate upper limit on the amount of  $\text{CO}_2$  that could have degassed from each sample prior to collection.

#### 2.3.2. Monte Carlo Mixing Model for Calculating $\delta^{34}\text{S}$ of Sulfuric Acid Sources

Because the  $\delta^{34}\text{S}$  of sulfur-bearing phases in the Koyukuk River catchment is unknown, we used a three end-member Monte Carlo isotope mass balance model to calculate the  $\delta^{34}\text{S}$  of a theoretical end-member representing the mass-weighted  $\text{SO}_4^{2-}$  contributions of all end-members that produce sulfuric acid during weathering. The calculation followed Relph et al. (2021) (Table 1). On a given iteration, we first calculated the amount of  $\text{SO}_4^{2-}$  derived from precipitation by assuming that all river  $\text{Cl}^-$  was sourced from precipitation (Equation 5). Second, we calculated the values of river water  $\delta^{34}\text{S}_{\text{SO}_4}$  (Equation 6) and  $\delta^{18}\text{O}_{\text{SO}_4}$  (Equation 7) with precipitation removed, indicated with the superscript \*; due to the low  $\text{Cl}^-/\text{SO}_4^{2-}$  ratios of the river samples, the precipitation correction altered mean  $\delta^{34}\text{S}_{\text{SO}_4}$  by only 0.00–0.10‰ and altered mean  $\delta^{18}\text{O}_{\text{SO}_4}$  by 0.01–0.16‰. The resulting mixing problem was then



solved using  $\delta^{18}\text{O}_{\text{SO}_4^*}$ ,  $\delta^{18}\text{O}_{\text{SO}_4\text{-evaporite}}$ , and  $\delta^{18}\text{O}_{\text{SO}_4\text{-sulfide-ox.}}$  with the latter calculated using the measurements of  $\delta^{18}\text{O}_{\text{H}_2\text{O}}$  and estimates for  $\delta^{18}\text{O}_{\text{O}_2}$ , the fraction of  $\text{SO}_4^{2-}$  oxygen derived from atmospheric  $\text{O}_2$ , and the fractionations between  $\text{SO}_4^{2-}$  and  $\text{O}_2$  ( $\epsilon_{\text{SO}_4\text{-O}_2}$ ) and between  $\text{SO}_4^{2-}$  and  $\text{H}_2\text{O}$  ( $\epsilon_{\text{SO}_4\text{-H}_2\text{O}}$ ) (Table 1; Equations 8 and 9) (Relph et al., 2021). Finally,  $\delta^{34}\text{S}_{\text{SO}_4\text{-sulfide-ox}}$  was calculated from the  $\delta^{18}\text{O}$ -derived mixing fraction (Equation 10). We repeated the calculation  $10^6$  times for each sample using randomly selected parameter values and used the resulting distributions to define the  $\delta^{34}\text{S}$  prior for the sulfide oxidation end-member in the MEANDIR inversions.

$$\text{SO}_4^{2-}\text{precipitation} = \text{IC}_{\text{sample}}^- \times \left( \frac{\text{SO}_4^{2-}}{\text{Cl}^-} \right)_{\text{precipitation}} \quad (5)$$

$$\delta^{34}\text{S}_{\text{SO}_4\text{-mixture}}^* = \frac{\delta^{34}\text{S}_{\text{SO}_4\text{-measured}} \times \text{SO}_4^{2-}\text{measured} - \delta^{34}\text{S}_{\text{SO}_4\text{-precipitation}} \times \text{SO}_4^{2-}\text{precipitation}}{\text{SO}_4^{2-}\text{measured} - \text{SO}_4^{2-}\text{precipitation}} \quad (6)$$

$$\delta^{18}\text{O}_{\text{SO}_4\text{-mixture}}^* = \frac{\delta^{18}\text{O}_{\text{SO}_4\text{-measured}} \times \text{SO}_4^{2-}\text{measured} - \delta^{18}\text{O}_{\text{SO}_4\text{-precipitation}} \times \text{SO}_4^{2-}\text{precipitation}}{\text{SO}_4^{2-}\text{measured} - \text{SO}_4^{2-}\text{precipitation}} \quad (7)$$

$$\delta^{18}\text{O}_{\text{SO}_4\text{-sulfide-ox.}} = f_{\text{O}_2} \times (\delta^{18}\text{O}_{\text{O}_2} + \epsilon_{\text{SO}_4\text{-O}_2}) + (1 - f_{\text{O}_2}) \times (\delta^{18}\text{O}_{\text{H}_2\text{O}} + \epsilon_{\text{SO}_4\text{-H}_2\text{O}}) \quad (8)$$

$$f_{\text{evap}} = \frac{(\delta^{18}\text{O}_{\text{SO}_4\text{-mixture}}^* - \delta^{18}\text{O}_{\text{SO}_4\text{-sulfide-ox.}})}{(\delta^{18}\text{O}_{\text{SO}_4\text{-evaporite}} - \delta^{18}\text{O}_{\text{SO}_4\text{-sulfide-ox.}})} \quad (9)$$

$$\delta^{34}\text{S}_{\text{SO}_4\text{-sulfide-ox.}} = \frac{\delta^{34}\text{S}_{\text{SO}_4\text{-mixture}}^* - f_{\text{evap}} \times \delta^{34}\text{S}_{\text{SO}_4\text{-evaporite}}}{1 - f_{\text{evap}}} \quad (10)$$

### 2.3.3. MEANDIR Inversions Constrain End-Member Contributions and Weathering $\Delta\text{ALK}/\Delta\text{IC}$

The MEANDIR inversion model was used to partition river dissolved load among end-member contributions (Kemeny & Torres, 2021). Observations of dissolved  $\text{Ca}^{2+}$ ,  $\text{Mg}^{2+}$ ,  $\text{Na}^+$ ,  $\text{K}^+$ ,  $\text{Cl}^-$ ,  $\text{SO}_4^{2-}$ , and  $\delta^{34}\text{S}_{\text{SO}_4}$  were inverted for contributions from carbonate weathering, silicate weathering, meteoric precipitation, dissolution of evaporite minerals, sulfide oxidation,  $\text{C}_{\text{org}}$  oxidation, and  $\text{CO}_2$  degassing from the river (Table 2). The composition of the carbonate end-member ranged between calcite and dolomite, the elemental ratios and uncertainty of the precipitation end-member reflected the four rain samples, sulfide oxidation sourced only  $\text{SO}_4^{2-}$ ,  $\text{C}_{\text{org}}$  oxidation sourced only DIC, and degassing removed only DIC (Table 2). Based on low ratios of  $\text{Cl}^-/\text{SO}_4^{2-}$  and  $\text{Cl}^-/\Sigma^+$  but moderate values of  $\delta^{18}\text{O}_{\text{SO}_4\text{-H}_2\text{O}}$  in mainstem samples, the evaporite end-member was assumed to be gypsum and sourced only  $\text{Ca}^{2+}$  and  $\text{SO}_4^{2-}$  with the  $\delta^{18}\text{O}_{\text{SO}_4}$  and  $\delta^{34}\text{S}_{\text{SO}_4}$  values of Phanerozoic evaporites (Claypool et al., 1980). The lithologic heterogeneity of the Koyukuk River catchment precluded use of a constrained prior for the chemical composition of the silicate end-member. Rather, contributions from silicate weathering were quantified by employing four inversion end-members that each provided exclusively either  $\text{Ca}^{2+}$ ,  $\text{Mg}^{2+}$ ,  $\text{Na}^+$ , or  $\text{K}^+$  (Cole et al., 2022). A composite silicate end-member was then constructed after the inversion using the contributions from each of the four single-cation end-members. This approach allowed MEANDIR to define a silicate end-member for each sample that best accommodated the contributions from the other end-members.

Including a degassing end-member in the inversion, motivated by the PHREEQC calculations showing that most samples were supersaturated with respect to  $\text{CO}_2$ , required defining the maximum allowable amount of degassing and a range of carbon isotope fractionation factors. We constrained the former by considering how much DIC must be added to each sample, without addition or removal of ALK, to decrease pH to either 5.0 or 6.0, representing two possible initial states that then evolved through degassing into the sample that we collected. Based on the PHREEQC calculations, an average of 71% of the initial DIC at a pH of 6.0 or 96% of the initial DIC at a pH of 5.0 could have been degassed prior to sample collection. For the scenario described in the main text of this article, we set a maximum fractional loss of DIC through degassing equal to 2.5 times in situ DIC, corresponding to the pH 6.0 case. For sensitivity testing, the inversion was also run with a degassing limit of 25 times in situ DIC, corresponding to the pH 5.0 case, as well as without the degassing end-member (Figures S10–S12, S15 in Supporting Information S1). The inversions including degassing were free to return lower amounts of degassing than the maximum values and, depending on  $\delta^{13}\text{C}_{\text{DIC}}$ , acceptable solutions might not exist near those maximum

**Table 2**  
*End-Member Distributions for MEANDIR Monte Carlo Inversion (Kemeny & Torres, 2021)*

Parameter	Carbonate	Silicate	Gypsum	Precipitation	Sulfide oxidation	C <sub>org</sub> oxidation	Degassing
Ca <sup>2+</sup>	Calculated	Calculated	Calculated	Calculated			
Mg <sup>2+</sup>	0.00–0.33	Calculated		0.07–0.11			
Na <sup>+</sup>		Calculated		0.12–0.27			
K <sup>+</sup>		Calculated		0.03–0.06			
Cl <sup>-</sup>				0.10–0.33			
SO <sub>4</sub> <sup>2-</sup>			0.5	0.13–0.37	1.00		
δ <sup>34</sup> S			10‰–30‰	4.5‰–5.9‰	–20‰ to –0‰		
DIC	0.33					1.00	1.00
δ <sup>13</sup> C	0‰					–30‰ to –24‰	–10.1‰ to –7.6‰
Fractionation (‰)							–2.5× DIC
Min. contribution	0 of norm	0 of norm	0 of norm	0 of norm	0 of norm	0 of norm	0× DIC
Max. contribution	Unbounded	1 of norm	1 of norm	1 of norm	1 of norm	Unbounded	

*Note.* Parameter values are normalized to the sum of Ca<sup>2+</sup>, Mg<sup>2+</sup>, Na<sup>+</sup>, K<sup>+</sup>, SO<sub>4</sub><sup>2-</sup>, and DIC. All distributions are uniform and blank entries indicate a value of zero. The silicate end-member represents four different end-members, each of which only sources Ca<sup>2+</sup>, Mg<sup>2+</sup>, Na<sup>+</sup>, or K<sup>+</sup>, which were aggregated into a composite end-member after the inversion. The degassing end-member made a negative contribution to river DIC. One chemical ratio for each end-member was calculated from the other ratios to ensure internal consistency.

values. Setting a limit on the fractional loss of DIC, as opposed to a fractional contribution to the inversion normalization variable, required a minor modification to the optimization code used in MEANDIR.

We set the carbon isotope fractionation factor for the degassing end-member to range uniformly between  $-10.1‰$  and  $-7.6‰$ . This range reflected the minimum and maximum difference between the calculated  $\delta^{13}\text{C}$  of in situ  $\text{CO}_2$  and measured  $\delta^{13}\text{C}_{\text{DIC}}$  across mainstem and slough samples. This range of fractionation factors and numerical approach does not account for changes in the effective fractionation factor as the dissolved carbon system adjusted to ongoing degassing, nor does it account for the kinetic isotope effect of  $\text{CO}_2$  diffusion across the river-atmosphere boundary (Polensnaere & Abril, 2012). For sensitivity testing, the inversion was thus also run with the degassing fractionation factor ranging from  $-20‰$  to  $0‰$  and from  $-10.1‰$  to  $0‰$  (Figures S13, S14, and S16 in Supporting Information S1).

The MEANDIR inversion model employed a Monte Carlo sampling strategy to account for uncertainty in the chemical composition of water samples and end-members. The inversion normalized observations to the charge-equivalent sum of  $\text{Ca}^{2+}$ ,  $\text{Mg}^{2+}$ ,  $\text{Na}^+$ ,  $\text{K}^+$ ,  $\text{SO}_4^{2-}$ , and DIC, and converted  $\delta^{34}\text{S}_{\text{SO}_4}$  and  $\delta^{13}\text{C}_{\text{DIC}}$  values to  $^{34}\text{S}/^{32}\text{S}$  and  $^{13}\text{C}/^{12}\text{C}$  ratios for the calculations. The optimization used a cost function of proportional misfit with equal weighting on all variables, did not use  $\text{Cl}^-$  critical values, constrained most end-member fractional contributions between 0% and 100%, and only considered simulations successful if they recreated between 95% and 105% of all major ion observations while being within 1‰ of measured  $\delta^{34}\text{S}_{\text{SO}_4}$  and  $\delta^{13}\text{C}_{\text{DIC}}$  values (Kemeny & Torres, 2021). All but two samples were successfully inverted 250 times in our primary inversion results with  $2.5\times$  degassing relative to in situ DIC. The failure to invert two samples, KY18-DP06-S1 and KY18-AKW-22, was due to their very high values of  $\delta^{13}\text{C}_{\text{DIC}}$  relative to their  $(\text{Ca}^{2+} + \text{Mg}^{2+})/\text{DIC}$  ratios.

The weathering  $\Delta\text{ALK}/\Delta\text{IC}$  ratio was quantified from inversion results. We calculated this ratio as a function of the parameters  $R$  and  $Z$ , which included  $\text{Ca}^{2+}$ ,  $\text{Mg}^{2+}$ ,  $\text{Na}^+$ , and  $\text{K}^+$ , where  $R$  is the carbonate fraction of carbonate and silicate weathering  $\text{ALK}$  and  $Z$  is the fraction of carbonate and silicate weathering  $\text{ALK}$  offset through sulfuric acid production (Torres et al., 2016). As discussed below, we quantified the oxidation of  $\text{C}_{\text{org}}$  but did not consider this process to represent a source of  $\text{IC}$  when calculating  $\Delta\text{ALK}/\Delta\text{IC}$ .

#### 2.4. Compilation of Prior Observations From the United States Geological Survey

Water quality observations from the Koyukuk River and the Yukon River were compiled to evaluate temporal changes in river chemistry. Out of 733 USGS sample entries within the catchment of the Koyukuk River, 148 had measurements of  $\text{Ca}^{2+}$ ,  $\text{Mg}^{2+}$ ,  $\text{Na}^+$ ,  $\text{K}^+$ ,  $\text{SO}_4^{2-}$ , and  $\text{Cl}^-$  concentrations. Sixty-one samples were collected between 1955 and 1978 from the mainstem Koyukuk River at the village of Hughes (site number 15564900), and major ion abundance was measured on 23 of the Hughes samples collected between 1955 and 1972. Although we lack methodological information for the measurement of major ion chemistry in these early samples and recognize that the methods used to determine the concentration of  $\text{SO}_4^{2-}$  through time in USGS samples have changed (Mast, 2013), we include the data from 1955 to 1972 in order to provide the longest possible temporal perspective. The compilation also includes USGS water quality records for the Yukon River at Pilot Station (site number 15565447; samples collected from 1954 to 1956 and from 1975 to 2022;  $n = 1,250$  total observations), the Yukon River at Stevens Village (site number 15453500; 1970–1978, 2000–2005;  $n = 215$ ), the Yukon River at Eagle (site number 15356000; 1950–1979, 2000–2005;  $n = 311$ ), the Tanana River at Nenana (site number 15515500; 1954–2021;  $n = 626$ ), and the Porcupine River near Fort Yukon (site number 15389000; 1966–1978, 2001–2005;  $n = 216$ ) (Figures S20–S25 in Supporting Information S1; Schuster, 2003, 2005a, 2005b, 2006, 2007). We also included the 2002–2003 observations of Dornblaser and Halm (2006), the 2004 observations of Halm and Dornblaser (2007), the 2006–2008 observations of Schuster et al. (2010), the 2009–2014 observations of Herman-Mercer (2016), and the 2014–2018 observations of Foks et al. (2020).

When comparing observations from the Koyukuk River through time, it is desirable to adjust measured concentrations to a reference discharge in order to remove artifacts associated with sampling different portions of the hydrograph. We choose a reference value of  $625 \text{ m}^3/\text{s}$ , which is approximately the median value of daily discharge at Hughes reported by the USGS from June through September, and the adjustment was done by applying a power law correction (Equation 11) using the exponent calculated from paired observations of discharge and concentration at Hughes (Equation 12; Figure S8 in Supporting Information S1). Because our new river water samples were not individually associated with discharge measurements, when scaling our geochemical observations, we



considered the full range of observed discharges between 1,220 and 2,390 m<sup>3</sup>/s (Figure 2a). Likewise, because discharge is unavailable for most of the USGS survey data, for these observations we considered the mean and the 5th to 95th percentiles of discharge at Hughes during the month in which each sample was collected.

$$[Z^+]_{\text{reference}} = [Z^+]_{\text{observed}} \times \left( \frac{Q_{\text{observed}}}{Q_{\text{reference}}} \right)^{-bz} \quad (11)$$

$$[Z^+]_{\text{Hughes}} = \kappa_Z \times (Q_{\text{Hughes}})^{-bz} \quad (12)$$

### 3. Results

#### 3.1. Major Ion Chemistry

The cation budget of river water and pore fluid samples was dominated by Ca<sup>2+</sup> and Mg<sup>2+</sup>. The concentration of Ca<sup>2+</sup> in mainstem samples ranged from 840 to 1,065 μM, the concentration of Mg<sup>2+</sup> ranged from 519 to 723 μM, the concentration of Na<sup>+</sup> ranged from 66 to 106 μM, and the concentration of K<sup>+</sup> ranged from 9 to 11 μM (Figure 2). Cation concentrations were higher in the headwater samples, with Ca<sup>2+</sup> and Mg<sup>2+</sup> concentrations exceeding 3 mM in the sample from the MF catchment. Overall, Ca<sup>2+</sup> represented 49%–80% of positive charge in solution, Mg<sup>2+</sup> accounted for 18%–50%, Na<sup>+</sup> comprised 1%–11%, and K<sup>+</sup> took up the remaining 0%–4% (Figure 3a). The highest Mg<sup>2+</sup>/Σ<sup>+</sup> ratios occurred in headwaters and mainstem samples, while pore fluid and slough samples had higher Ca<sup>2+</sup>/Σ<sup>+</sup> ratios and both higher and lower values of (Na<sup>+</sup> + K<sup>+</sup>)/Σ<sup>+</sup>.

For anions, the concentration of SO<sub>4</sub><sup>2-</sup> in mainstem samples ranged from 707 to 1,049 μM and the concentration of Cl<sup>-</sup> ranged from 3 to 10 μM. The concentration of SO<sub>4</sub><sup>2-</sup> was >1 mM in the sample from the SC site, >2.3 mM in the sample from the MC site, and >4.7 mM for the sample from the MF site. As fractions of positive charge, SO<sub>4</sub><sup>2-</sup>/Σ<sup>+</sup> ranged from 6% to 98% and HCO<sub>3</sub><sup>-</sup>/Σ<sup>+</sup> ranged from 2% to 93% in the river water and pore fluid samples while the ratio Cl<sup>-</sup>/Σ<sup>+</sup> was <2% (Figure 3b). Overall, headwater and mainstem water samples had higher SO<sub>4</sub><sup>2-</sup>/Σ<sup>+</sup> and lower Ca<sup>2+</sup>/Σ<sup>+</sup> than pore fluids and slough samples (Figure 3c).

#### 3.2. SO<sub>4</sub><sup>2-</sup> <sup>34</sup>S/<sup>32</sup>S and <sup>18</sup>O/<sup>16</sup>O Ratios and H<sub>2</sub>O <sup>18</sup>O/<sup>16</sup>O and D/H Ratios

Values of δ<sup>34</sup>S<sub>SO<sub>4</sub></sub> ranged from -6.8 to 6.2‰ (Figure 4). Mainstem samples ranged in δ<sup>34</sup>S<sub>SO<sub>4</sub></sub> from -0.9 to -0.4‰, with a mean value of -0.6‰ ± 0.3‰ (*n* = 27, 2σ). The headwater sample from the large and steep MF catchment had a δ<sup>34</sup>S<sub>SO<sub>4</sub></sub> value of -0.6‰, isotopically identical to the mainstem Koyukuk River samples, while the other headwater samples ranged in δ<sup>34</sup>S<sub>SO<sub>4</sub></sub> from -6.8‰ at MC to -4.0‰ at SF. Precipitation δ<sup>34</sup>S<sub>SO<sub>4</sub></sub> values ranged from 4.7‰ to 6.2‰, consistent with the expectation that a fraction of SO<sub>4</sub><sup>2-</sup> in precipitation is sourced from seawater with elevated values of δ<sup>34</sup>S<sub>SO<sub>4</sub></sub>. Slough δ<sup>34</sup>S<sub>SO<sub>4</sub></sub> values were slightly elevated from the mainstem, ranging from 0.2‰ to 2.4‰. Pore fluid δ<sup>34</sup>S<sub>SO<sub>4</sub></sub> was more variable, ranging from -6.0‰ to 3.6‰, but only three samples had δ<sup>34</sup>S<sub>SO<sub>4</sub></sub> values elevated above the average mainstem value.

The δ<sup>18</sup>O<sub>SO<sub>4</sub></sub> values of four mainstem samples were -5.7‰, -4.9‰, -3.8‰, and -3.8‰ (Figure 5). The MF headwater sample, which matched the Koyukuk mainstem for δ<sup>34</sup>S<sub>SO<sub>4</sub></sub>, had a δ<sup>18</sup>O<sub>SO<sub>4</sub></sub> value of -6.0‰. The other three headwater samples, which had lower δ<sup>34</sup>S<sub>SO<sub>4</sub></sub> values, had much higher δ<sup>18</sup>O<sub>SO<sub>4</sub></sub> values ranging from -1.4‰ to 1.2‰. The δ<sup>18</sup>O<sub>SO<sub>4</sub></sub> values of four pore fluid samples ranged from -4.2‰ to -3.2‰, and δ<sup>18</sup>O<sub>SO<sub>4</sub></sub> values in two slough samples were -2.3‰ and -0.5‰.

Values of δ<sup>18</sup>O<sub>H<sub>2</sub>O</sub> in the samples collected near Huslia ranged from -20.4‰ to -17.6‰ and values of δ<sup>18</sup>O<sub>SO<sub>4</sub>-H<sub>2</sub>O</sub> ranged from 14.5‰ to 17.1‰. Slough samples had higher values of δ<sup>18</sup>O<sub>H<sub>2</sub>O</sub> than mainstem samples that partially offset their higher values of δ<sup>18</sup>O<sub>SO<sub>4</sub></sub>. Values of δD<sub>H<sub>2</sub>O</sub> ranged from -157.7‰ to -141.0‰. All samples from the Koyukuk River mainstem and Huslia River were consistent with the local meteoric water line, defined by prior water isotope observations within the catchment (Figure S7 in Supporting Information S1). In contrast, samples from sloughs, lakes, and summertime precipitation fell on a line with lower slope that may reflect a local evaporation line. These δD<sub>H<sub>2</sub>O</sub>-δ<sup>18</sup>O<sub>H<sub>2</sub>O</sub> relationships suggest that samples from the sloughs have undergone evaporation, possibly during periods of low mainstem discharge and relative isolation, or potentially indicate mixing with evaporated lake water.

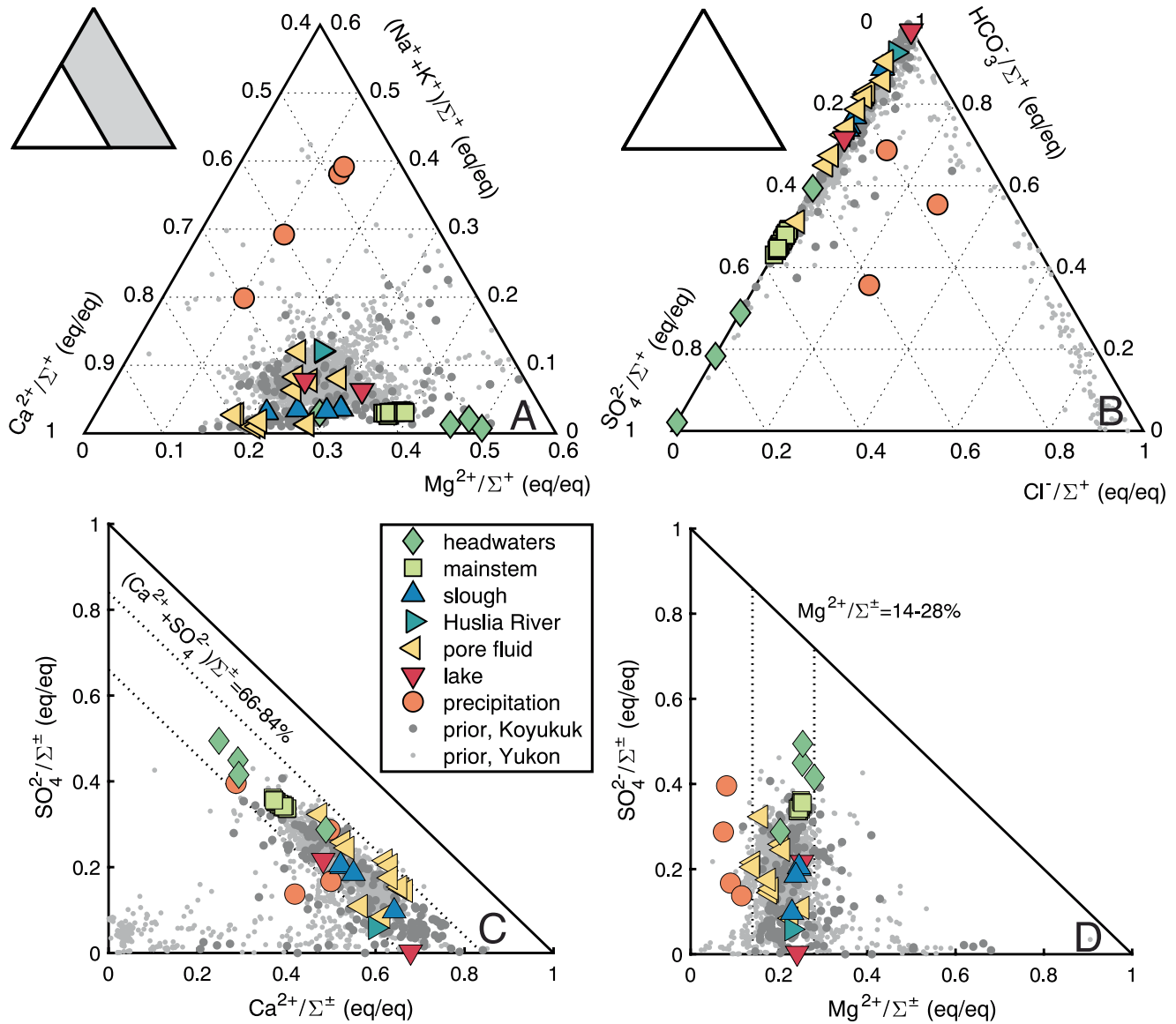


**Figure 3.** Major ion chemistry of samples from the Koyukuk River and Yukon River, including from this study (colored points) and historical datasets (gray points). (a) Cation ternary diagram of  $\text{Ca}^{2+}$ – $\text{Mg}^{2+}$ – $\text{Na}^+ + \text{K}^+$ . The plotted triangle is a subset of the full space, as indicated in the top-left schematic (gray triangle is the full domain and white triangle is the plotted space). The cations  $\text{Ca}^{2+}$  and  $\text{Mg}^{2+}$  dominate positive charge in the Koyukuk River samples. These relative cation abundances agree with prior observations from throughout the Koyukuk River catchment (dark gray circles) and the broader Yukon River Basin (light gray circles). (b) Anion ternary diagram of  $\text{SO}_4^{2-}$ – $\text{Cl}^-$ – $\text{HCO}_3^-$  for the full domain, with  $\text{HCO}_3^-$  calculated through charge balance. Water samples span between dominance of  $\text{SO}_4^{2-}$  and  $\text{HCO}_3^-$ , while the only samples with appreciable  $\text{Cl}^-/\Sigma^+$  are precipitation. Prior samples plotting near  $\text{Cl}^-/\Sigma^+ \sim 1$  were collected near the Alaskan coast. (c) Headwater and mainstem samples have elevated  $\text{SO}_4^{2-}/\Sigma^{\pm}$  and reduced  $\text{Ca}^{2+}/\Sigma^{\pm}$  ratios relative to pore fluid and slough samples. (d) The ratio of  $\text{Mg}^{2+}/\Sigma^{\pm}$  is relatively constant across sample types and, due to the low ratios of  $\text{Na}^+/\Sigma^{\pm}$  and  $\text{K}^+/\Sigma^{\pm}$ , implies that changes in  $\text{Ca}^{2+}/\Sigma^{\pm}$  largely compensate changes in  $\text{SO}_4^{2-}/\Sigma^{\pm}$ . Dashed lines in (c) and (d) reflect bounds of labeled  $(\text{Ca}^{2+} + \text{SO}_4^{2-})/\Sigma^{\pm}$  and  $\text{Mg}^{2+}/\Sigma^{\pm}$ , respectively.

### 3.3. Abundance and Carbon Isotope Ratios of DIC and DOC

The concentration of DIC is expected to approximately match the concentration of  $\text{HCO}_3^-$  in river water samples at circumneutral pH. Consistent with this expectation, the mean absolute proportional difference between DIC and the concentration of  $\text{HCO}_3^-$  derived through charge balance was only 4.0% in the mainstem and slough samples. The difference exceeded 10% for a pore-fluid sample (15% in AKW-27#1) and two lake samples (29% in AKW-22 and 215% in AKW-20); the two lake samples are also notable for having the two highest values of measured  $\delta^{13}\text{C}_{\text{DIC}}$  and relatively low pH values (6.7 in AKW-22 and 5.6 in AKW-20).

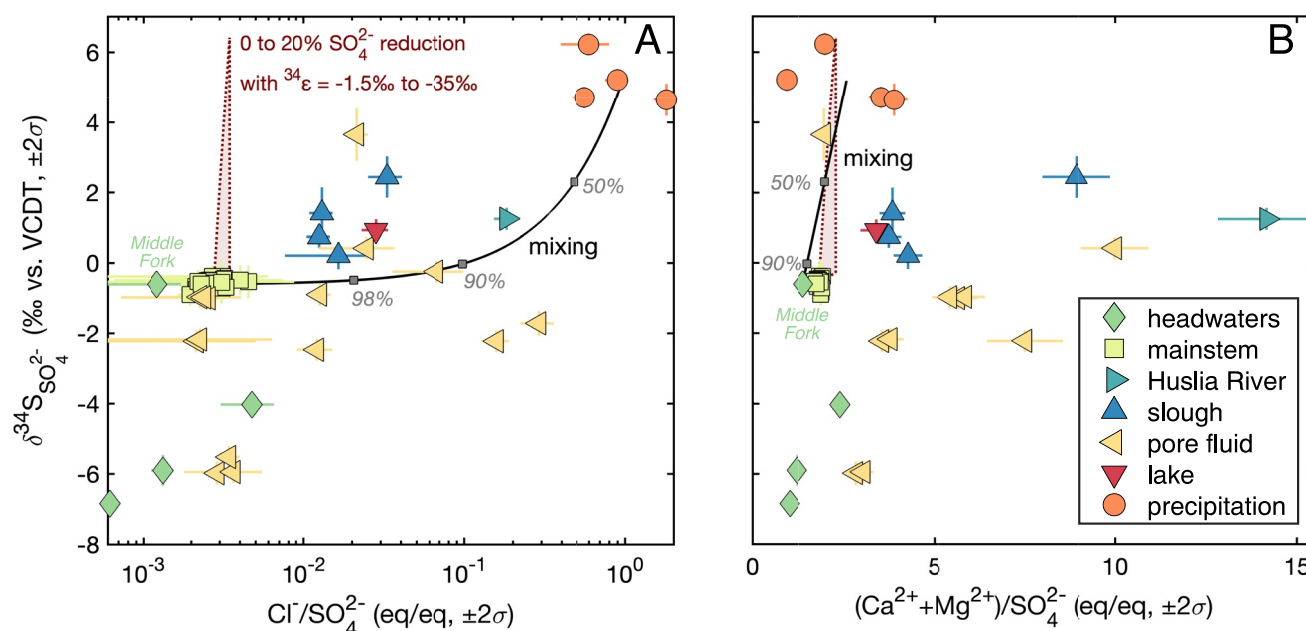


**Figure 4.** Sulfate sulfur isotope mixing diagrams.  $\delta^{34}\text{S}_{\text{SO}_4}$  against (a)  $\text{Cl}^-/\text{SO}_4^{2-}$  and (b)  $(\text{Ca}^{2+} + \text{Mg}^{2+})/\text{SO}_4^{2-}$ . Observations are consistent with a combination of mixing between the Middle Fork headwater sample and precipitation (black line), a modest amount of sulfate reduction that increases slough  $\delta^{34}\text{S}_{\text{SO}_4}$  values and reduces pore fluid  $\delta^{34}\text{S}_{\text{SO}_4}$  values (red shading), and the addition of  $\text{Ca}^{2+}$  and  $\text{Mg}^{2+}$  through floodplain weathering. Gray dots on the mixing curve indicate where 98%, 90%, and 50% of sulfur atoms are sourced from the headwater end-member.

DIC concentrations ranged from 699  $\mu\text{M}$  in a lake sample to 5,925  $\mu\text{M}$  in a pore fluid sample, with mainstem samples ranging from 1,287  $\mu\text{M}$  to 1,634  $\mu\text{M}$  (Figure 6). By assuming equilibrium speciation among the dissolved carbon species at measured temperature and pH values, PHREEQC calculations found that in situ  $\text{CO}_2$  concentrations mostly exceeded values for equilibrium with the atmosphere at a  $p\text{CO}_2$  of 410 ppm. Ratios of in situ/equilibrium  $\text{CO}_2$  exceeded 1 for  $\sim 90\%$  of mainstem samples (20/22), reaching values as high as 7.7, and were equal to 0.9 in the remaining mainstem samples (2/22). Ratios ranged between 5.6 and 11.4 in the slough samples ( $n = 4$ ).

Values of  $\delta^{13}\text{C}_{\text{DIC}}$  ranged from  $-16.7\text{‰}$  to  $-2.7\text{‰}$ . Samples from the mainstem Koyukuk were tightly clustered around a mean  $\delta^{13}\text{C}_{\text{DIC}}$  value of  $-7.8 \pm 0.4\text{‰}$  ( $2\sigma$ ,  $n = 47$ ), similar to two prior observations from the Koyukuk River (Dornblaser and Halm, 2006). Although this value was only slightly elevated from the estimate for the  $\delta^{13}\text{C}$  of atmospheric  $\text{CO}_2$  in 2018,  $-8.5\text{‰}$ , which we approximated from the trend of Keeling et al. (2017), the PHREEQC calculations indicated that most samples had more  $p\text{CO}_2$  than expected for equilibrium with the atmosphere and thus that direct incorporation of atmospheric  $\text{CO}_2$  was unlikely to explain the measured values. Slough samples had lower values of  $\delta^{13}\text{C}_{\text{DIC}}$  than the mainstem,  $-11.7 \pm 1.5\text{‰}$  ( $2\sigma$ ,  $n = 5$ ), suggesting a greater role for  $\text{C}_{\text{org}}$  oxidation, and DIC concentrations were higher in slough samples than in the mainstem. Samples from the Huslia River had low values of  $\delta^{13}\text{C}_{\text{DIC}}$ ,  $-10.7 \pm 0.5\text{‰}$  ( $2\sigma$ ,  $n = 4$ ), but with DIC concentrations lower than mainstem samples (Figure 6). The lowest  $\delta^{13}\text{C}_{\text{DIC}}$  value,  $-16.7\text{‰}$ , occurred in the only analyzed pore fluid, which also had the highest concentration of DIC. The highest and second lowest  $\delta^{13}\text{C}_{\text{DIC}}$  values were both from lakes with low pH values; one at pH 4.6 with a  $\delta^{13}\text{C}_{\text{DIC}}$  value of  $-16.2\text{‰}$ , and the other at pH 5.6 with a  $\delta^{13}\text{C}_{\text{DIC}}$  of  $-2.7\text{‰}$ .

Values of  $\delta^{13}\text{C}_{\text{DOC}}$  ranged from  $-28.8\text{‰}$  to  $-26.5\text{‰}$  and values of  $F_{\text{mod-DOC}}$  ranged from 0.9432 to 1.0191. These  $\delta^{13}\text{C}_{\text{DOC}}$  values were similar to prior measurements of  $\delta^{13}\text{C}$  in sedimentary organic carbon, which ranged from  $-30.5\text{‰}$  to  $-25.5\text{‰}$  (Douglas et al., 2022). For further calculations, we took  $-27.5\text{‰}$  as the value of  $\delta^{13}\text{C}_{\text{DIC}}$  produced through  $\text{C}_{\text{org}}$  respiration.  $F_{\text{mod-DOC}}$  values were higher than in sedimentary organic carbon (Douglas et al., 2022), a relationship consistent with prior observations showing that DOC in rivers flowing through permafrost-affected terrains is often dominated by young organic matter (Barnes et al., 2018; Benner et al., 2004; Drake et al., 2018a; Neff et al., 2006; Schwab et al., 2020; Striegl et al., 2007).



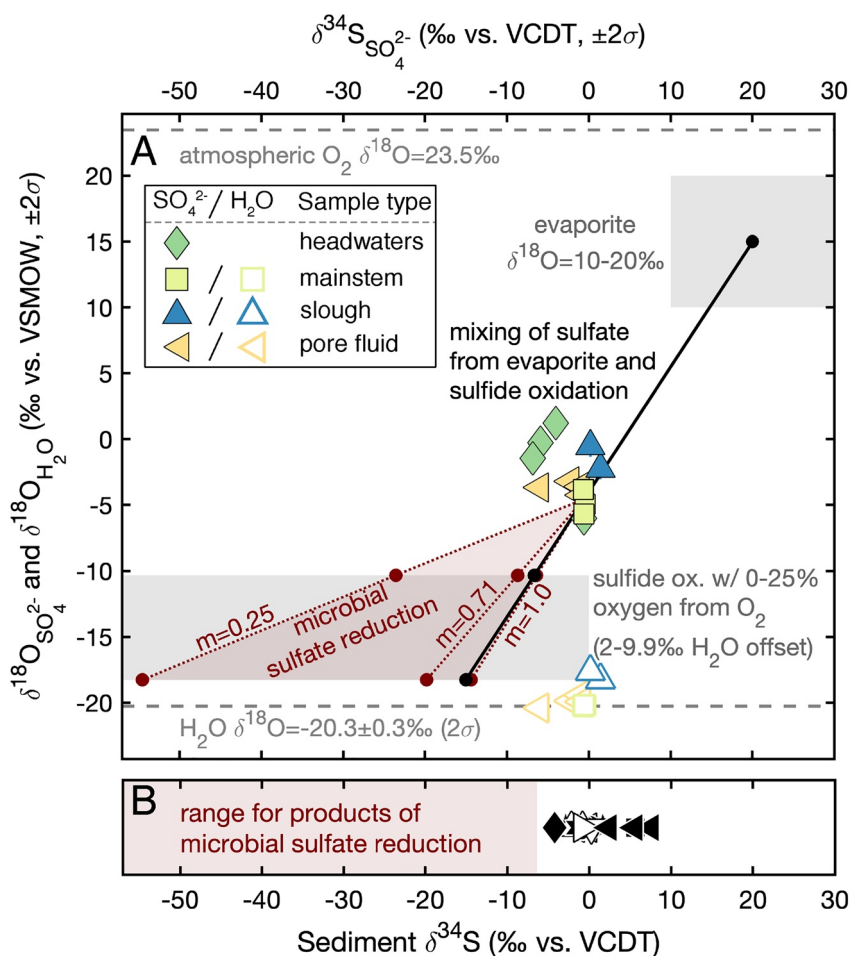


**Figure 5.** Sulfur and oxygen isotope ratios in dissolved  $\text{SO}_4^{2-}$ ,  $\text{H}_2\text{O}$ , and sediment. (a) Sample  $\delta^{18}\text{O}_{\text{SO}_4}$  (closed symbols) and  $\delta^{18}\text{O}_{\text{H}_2\text{O}}$  (open symbols) against  $\delta^{34}\text{S}_{\text{SO}_4}$  with dotted reference lines for the mean value of mainstem  $\delta^{18}\text{O}_{\text{H}_2\text{O}}$  ( $-20.3\text{‰}$ ) and atmospheric  $\delta^{18}\text{O}_{\text{O}_2}$  ( $23.5\text{‰}$ ). Gray shaded regions indicate the expected ranges for Phanerozoic evaporites (Claypool et al., 1980) and for sulfide oxidation incorporating  $\leq 25\%$  atmospheric  $\text{O}_2$  (Killingsworth et al., 2018) when  $\epsilon_{\text{SO}_4\text{-H}_2\text{O}} = 2\text{‰}$  and  $\epsilon_{\text{SO}_4\text{-O}_2} = -10\text{‰}$  (Balci et al., 2007). Note that the plotted sulfide oxidation region captures only a subset of the range attainable in the full three end-member mixing model (Table 1). Analyzed samples have  $\delta^{18}\text{O}_{\text{SO}_4\text{-H}_2\text{O}}$  values above expectations for sulfide oxidation and require either dissolution of sulfate salts or the catchment-scale expression of a fractionating process such as microbial  $\text{SO}_4^{2-}$  reduction. Red shaded region indicates the expected area for microbial sulfate reduction (MSR) with relative oxygen and sulfur isotope fractionations ranging from 0.25 to 1.0 ( $m$  values; Aharon & Fu, 2000; Mandernack et al., 2003; Antler et al., 2013). Note that the plotted linear behavior only approximates the actual non-linear behavior of the system when fully accounting for partial oxygen isotope equilibration (Antler et al., 2013, 2017; Brunner et al., 2005; Turchyn et al., 2010). (b) Predicted  $\delta^{34}\text{S}$  range for products of MSR (red shading) and observed values. Sediment  $\delta^{34}\text{S}$  values are comparable to river water  $\delta^{34}\text{S}_{\text{SO}_4}$  and indicate that sulfate reduction likely does not overtly influence the sulfur isotopic composition of  $\text{SO}_4^{2-}$  in Koyukuk River water samples.

### 3.4. Sedimentary Sulfur Chemistry

Values of  $\delta^{34}\text{S}_{\text{sediment}}$  ranged from  $-4.2\text{‰}$  to  $7.5\text{‰}$  and sediment S contents ranged from 0.02 to 0.18 wt% (Figure 7 and Figure S5 in Supporting Information S1). Neither  $\delta^{34}\text{S}_{\text{sediment}}$  nor S abundance were clearly related to whether or not a sample was from a permafrost deposit. About half of the samples had  $\delta^{34}\text{S}_{\text{sediment}}$  values between  $0\text{‰}$  and  $-2\text{‰}$ , comparable to the  $\delta^{34}\text{S}_{\text{SO}_4}$  of the mainstem river. Samples from core 9 had relatively elevated  $\delta^{34}\text{S}_{\text{sediment}}$  values of  $2.4\text{‰}$ ,  $5.6\text{‰}$ , and  $7.5\text{‰}$ , where the two higher values occurred in peat samples. This site is stratigraphically the oldest analyzed deposit and might reflect secular change in sedimentary chemistry through time or, due to its physical distance from the active channel, could have a larger fraction of sulfur sourced from high- $\delta^{34}\text{S}_{\text{SO}_4}$  precipitation than sites closer to the river.

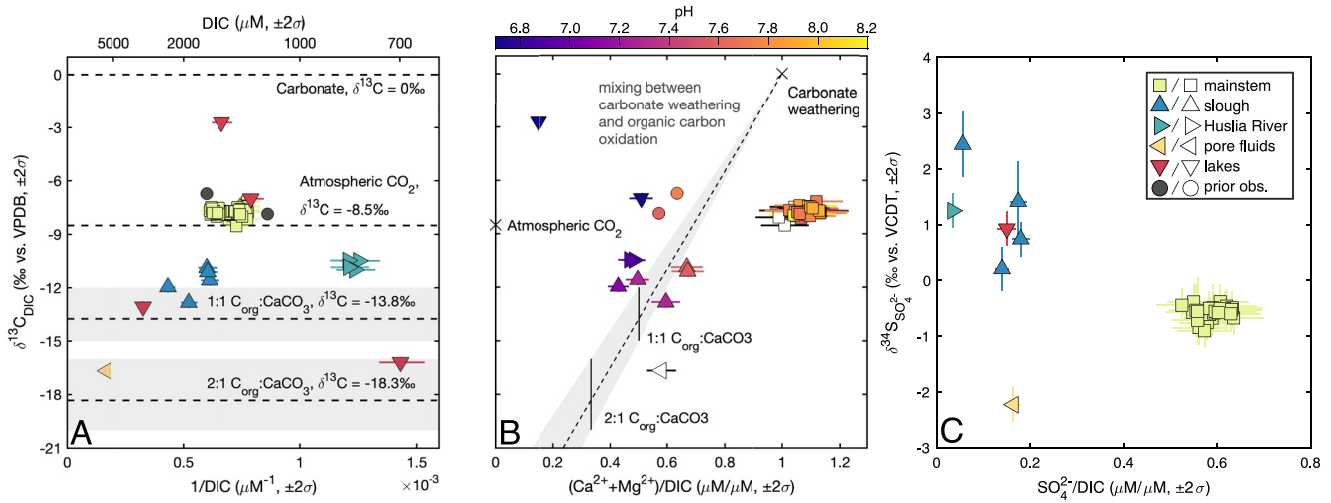


**Figure 6.** DIC concentrations and  $^{13}\text{C}/^{12}\text{C}$  isotope ratios. (a)  $\delta^{13}\text{C}_{\text{DIC}}$  against  $1/\text{DIC}$ . Reference lines are shown for the  $\delta^{13}\text{C}_{\text{DIC}}$  produced from 1:1 and 2:1 combinations of  $\text{C}_{\text{org}}$  oxidation and  $\text{CaCO}_3$  weathering. Mainstem samples from the Koyukuk River cluster near  $-7.8\%$ , and  $\delta^{13}\text{C}$  values in mainstem samples are higher than in the sloughs. The sloughs tended to have higher DIC concentrations than the mainstem, while lake samples exhibited a wide range of both DIC abundances and  $\delta^{13}\text{C}_{\text{DIC}}$  values. (b)  $\delta^{13}\text{C}_{\text{DIC}}$  against  $(\text{Ca}^{2+} + \text{Mg}^{2+})/\text{DIC}$ . The slough data mostly fall near the mixing line between carbonate weathering and  $\text{C}_{\text{org}}$  oxidation. The mainstem samples plot off the mixing line, which implies either inputs of  $\text{Ca}^{2+}$  and  $\text{Mg}^{2+}$  or that a process such as  $\text{CO}_2$  degassing has removed DIC. (c) Sloughs samples had lower  $\text{SO}_4^{2-}/\text{DIC}$  ratios and higher  $\delta^{34}\text{S}_{\text{SO}_4}$  values than mainstem samples.

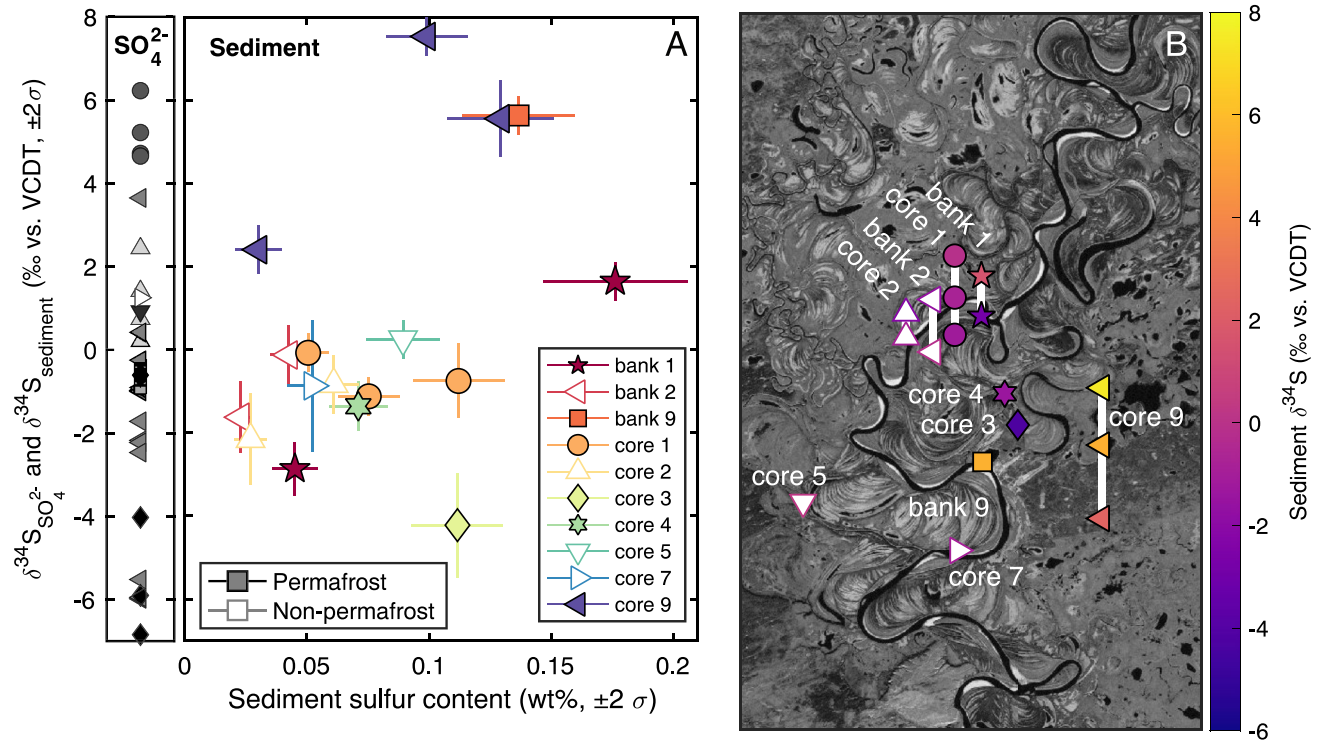


**Figure 7.** Sedimentary sulfur isotope ratios. (a) Values of  $\delta^{34}\text{S}_{\text{sediment}}$  (cross plot) were comparable to values of river  $\delta^{34}\text{S}_{\text{SO}_4}$  (left stack, symbols as in prior figures) and were not correlated with S content or whether samples were collected from permafrost (closed symbols) or non-permafrost (open symbols) deposits. These moderate  $\delta^{34}\text{S}_{\text{sediment}}$  values were consistent with modest amounts of sulfate reduction capable of minor modifications to  $\delta^{34}\text{S}_{\text{SO}_4}$  in sloughs and pore fluids. (b) Sediment  $\delta^{34}\text{S}$  values in landscape context (Landsat 5, 9/24/10). Samples collected from depth profiles are vertically proportional to collection depth and sites that would otherwise overlap are offset horizontally.

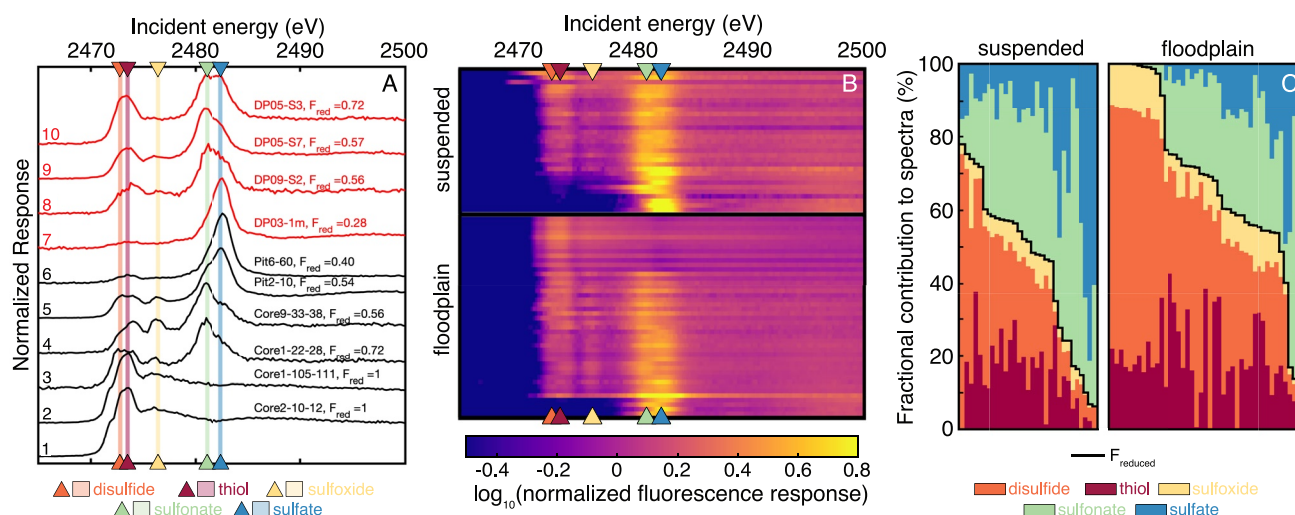


**Figure 8.** X-ray spectroscopy results on floodplain and suspended sediment. (a) 10 example spectra showing a range of sulfur moieties in both suspended sediment (red) and floodplain sediment (black). Vertical colored bars indicate characteristic spectral features of disulfide, thiol, sulfoxide, sulfonate, and sulfate moieties. (b) Waterfall plot of all spectra, where color is the intensity of the fluorescence response. Fluorescence data are displayed logarithmically to highlight the peaks corresponding to disulfide, thiol, and sulfoxide moieties. (c) Fractional contributions of sulfur moieties to measured spectra. Samples of both floodplain and suspended sediment contained a diversity of redox phases. In panels (b) and (c) spectra are arranged within sample types in order of decreasing  $F_{red}$  value.

The synchrotron spectra indicate thiol, disulfide, sulfoxide, sulfonate, and sulfate moieties within floodplain and suspended sediment (Figure 8). The presence of these phases is consistent with production and cycling of organic sulfur within the Koyukuk floodplain. The mean  $F_{red}$  value, which reflects the fractional contribution of reduced sulfur moieties to synchrotron spectra, was 0.70 across the analyzed sediment samples.

### 3.5. Numerical Results

The three end-member mixing model constrained the  $\delta^{34}\text{S}_{\text{SO}_4}$  value expected for sulfuric acid sources between  $-18.2\text{‰}$  and  $-1.8\text{‰}$  in 90% of simulations for mainstem samples. For the Monte Carlo inversion conducted with MEANDIR, we approximated these values and assumed that the sulfide oxidation end-member generates  $\text{SO}_4^{2-}$  with a uniform distribution of  $\delta^{34}\text{S}_{\text{SO}_4}$  values between  $-20$  and  $0\text{‰}$  (Table 2). This range reflects the net contribution-weighted composition of sulfuric acid sources and need not reflect the  $^{34}\text{S}/^{32}\text{S}$  ratio of any particular deposit material and/or geological unit.

The primary river inversion model constrained inputs from precipitation, silicate weathering, gypsum dissolution, carbonate weathering, sulfide oxidation,  $\text{C}_{org}$  oxidation, and  $\text{CO}_2$  degassing (Figure 9; Table S2 in Supporting Information S1). Considering the median fractional contributions across mainstem river and slough samples,  $\text{Cl}^-$  was sourced exclusively from precipitation (100%),  $\text{SO}_4^{2-}$  was derived predominantly from sulfide oxidation (80%) and gypsum dissolution (20%),  $\text{Na}^+$  and  $\text{K}^+$  were sourced predominantly from silicate weathering (94%, 91%) and meteoric precipitation (6%, 9%), DIC was derived from carbonate weathering (73%) and  $\text{C}_{org}$  oxidation (38%) but lost to degassing ( $-11\%$ ),  $\text{Mg}^{2+}$  was sourced predominantly from carbonate weathering (70%) and silicate weathering (29%), and  $\text{Ca}^{2+}$  was derived from carbonate weathering (75%), gypsum dissolution (16%), and silicate weathering (5%). Slough samples had lower median contributions from the sulfide oxidation end-member to river  $\text{SO}_4^{2-}$  than mainstem samples (72% vs. 81%), higher median contributions of carbonate to dissolved  $\text{Ca}^{2+}$  (87% vs. 73%), and higher median contributions from  $\text{C}_{org}$  oxidation to DIC (51% vs. 37%). The inversion-constrained chemistry of the carbonate end-member spanned from calcite to dolomite while the reconstructed silicate end-member had  $\text{Mg}^{2+}/\Sigma^\pm$  ranging from 0.23 to 0.73,  $\text{Ca}^{2+}/\Sigma^\pm$  ranging from 0.09 to 0.22,  $\text{Na}^+/\Sigma^\pm$  ranging from 0.11 to 0.22, and  $\text{K}^+/\Sigma^\pm$  ranging from 0.01 to 0.10 (Figure S9 in Supporting Information S1).

Results from the inversion without  $\text{CO}_2$  degassing were similar to results with  $\text{CO}_2$  degassing for mainstem and slough samples but different for the pore fluid sample (Table S2; Figures S10–S12, S15 in Supporting Information S1). Removing the degassing end-member from the inversion decreased the average median fractional contribution of  $\text{C}_{org}$  oxidation to dissolved DIC from 51% to 47% in slough samples and from 37% to 29% in

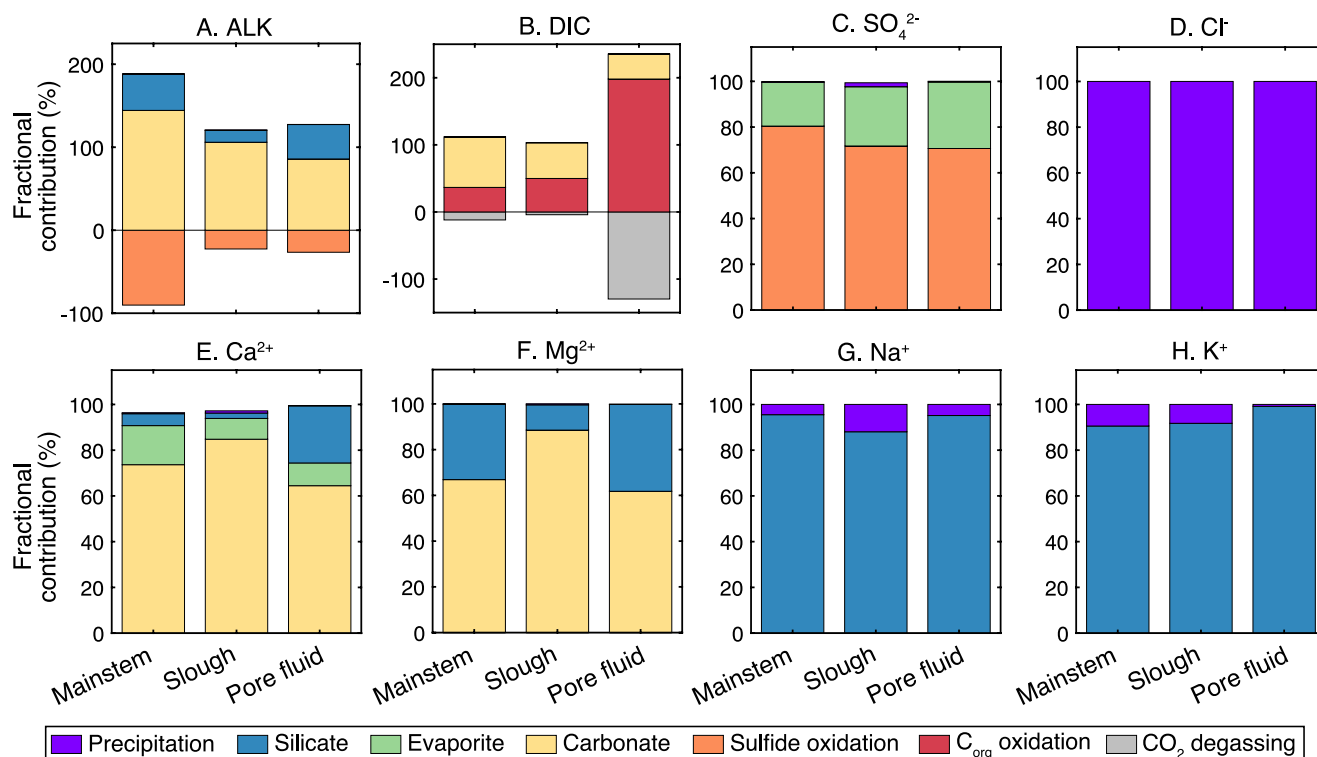


**Figure 9.** Inversion-constrained median end-member contributions to river chemistry. Average fractional contributions of the precipitation, silicate, evaporite, carbonate, sulfide oxidation, C<sub>org</sub> oxidation, and degassing end-members are given for (a) ALK, (b) DIC, (c) SO<sub>4</sub><sup>2-</sup>, (d) Cl<sup>-</sup>, (e) Ca<sup>2+</sup>, (f) Mg<sup>2+</sup>, (g) Na<sup>+</sup>, and (h) K<sup>+</sup> in the mainstem, slough, and pore fluid samples. Note that the sum of median end-member contributions is not constrained to equal 100%.

mainstem samples, and decreased the average median fractional contribution of the carbonate end-member to dissolved Ca<sup>2+</sup> from 73% to 66% in mainstem samples.

### 3.6. Historical Comparison

Comparison of the 2018 Koyukuk River observations with measurements from 1955 to 1972 and from 2003 to 2014 highlighted changes in absolute and relative major ion concentrations (Figure 10). Between 1955–1972 and 2003–2014, the mean June–September concentrations of SO<sub>4</sub><sup>2-</sup>, Ca<sup>2+</sup>, and Mg<sup>2+</sup> increased by 425, 270, and 208 μM, respectively, and further changed between 2003–2014 and 2018 by 140, –24, and 100 μM (Figure 10a–10d). Compared at a reference discharge of 625 m<sup>3</sup>/s (Equations 11 and 12), from 1955–1972 to 2003–2014 the mean concentration of SO<sub>4</sub><sup>2-</sup>, Ca<sup>2+</sup>, and Mg<sup>2+</sup> increased by 570, 394, and 256 μM, respectively, and further increased between 2003–2014 and 2018 by 240, 90, and 188 μM (Figure 10e–10h). The mean SO<sub>4</sub><sup>2-</sup>/Σ<sup>+</sup>, Ca<sup>2+</sup>/Σ<sup>+</sup>, and Mg<sup>2+</sup>/Σ<sup>+</sup> ratios of the discharge-adjusted data changed, respectively, by 0.24, –0.03, and 0.03 between 1955–1972 and 2003–2014, and further changed by 0.07, –0.04, and 0.05 between 2003–2014 and 2018 (Figures 10i–10l).

## 4. Discussion

### 4.1. The Origins and Transformations of River SO<sub>4</sub><sup>2-</sup>

Evaluating the impact of chemical weathering on *p*CO<sub>2</sub> requires distinguishing among multiple sources and fractionating sinks of fluvial SO<sub>4</sub><sup>2-</sup>. Values of δ<sup>34</sup>S<sub>SO<sub>4</sub></sub> and δ<sup>18</sup>O<sub>SO<sub>4</sub></sub> are useful measurements in this effort because processes such as sulfide oxidation, evaporite dissolution, and biological fractionation carry distinct isotopic signatures (Antler et al., 2013; Calmels et al., 2007; Turchyn et al., 2013). Our preferred interpretation of the measured δ<sup>34</sup>S<sub>SO<sub>4</sub></sub> and δ<sup>18</sup>O<sub>SO<sub>4</sub></sub> values is that gypsum dissolution and sulfide oxidation, with only a minor influence from microbial sulfate reduction (MSR), explain the isotopic composition of SO<sub>4</sub><sup>2-</sup> in the mainstem Koyukuk River and its headwaters. In turn, modest amounts of assimilatory and dissimilatory sulfate reduction generate isotopic variations among samples from the mainstem, sloughs, and pore fluids collected near Huslia.



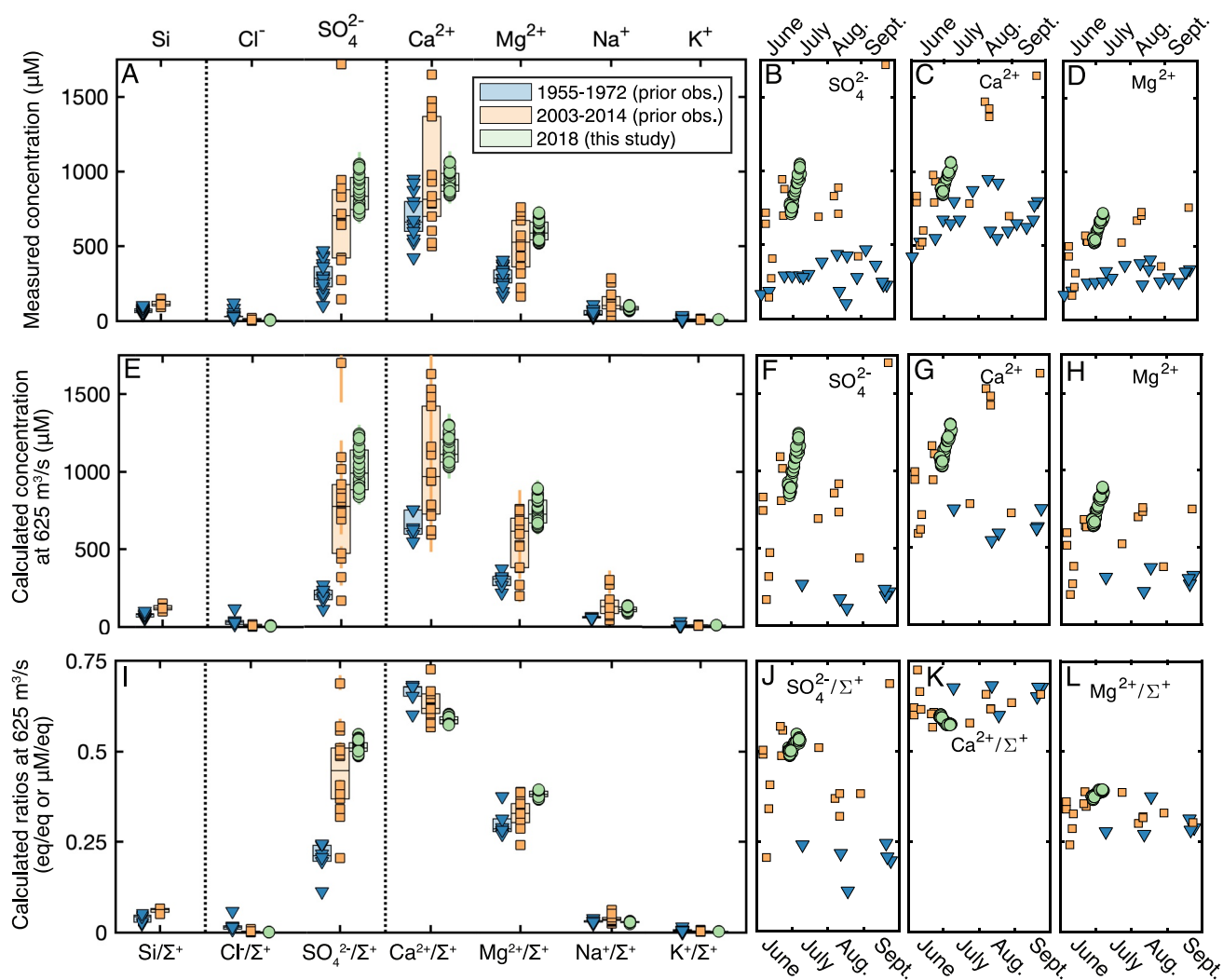


**Figure 10.** Temporal changes in the summertime major ion chemistry of the Koyukuk River. All plotted data are from June through September. (a–d) Measured concentrations and (e–h) concentrations adjusted to 625 m<sup>3</sup>/s. (i–l) Elemental ratios show increases in SO<sub>4</sub><sup>2-</sup>/Σ<sup>+</sup> and Mg<sup>2+</sup>/Σ<sup>+</sup> through time, as well as decreases in Ca<sup>2+</sup>/Σ<sup>+</sup>. Plotting symbols and error bars in (a–d) are mean values and analytical error, where available. Plotting symbols and error bars in (e–l) for the 2018 data reflect the mean and range of observed discharge during fieldwork, and for the 2003–2014 samples reflect the mean and 5th to 95th percentiles of discharge at Hughes in the month of sample collection.

#### 4.1.1. Koyukuk River SO<sub>4</sub><sup>2-</sup> Derives From Sulfide Oxidation and Gypsum Dissolution

##### 4.1.1.1. Measured δ<sup>18</sup>O<sub>SO<sub>4</sub>-H<sub>2</sub>O</sub> Values Exceed Expectations From Sulfide Oxidation

We first evaluated whether SO<sub>4</sub><sup>2-</sup> could derive entirely from sulfide oxidation by comparing observed values of δ<sup>18</sup>O<sub>SO<sub>4</sub></sub> to the values predicted for SO<sub>4</sub><sup>2-</sup> derived from sulfide oxidation. The oxygen atoms in sulfate produced during sulfide oxidation derive from a variable combination of ambient H<sub>2</sub>O and O<sub>2</sub> depending on the oxidation mechanism, with the fraction of O<sub>2</sub>-derived oxygen ≤15%–25% (Balci et al., 2007; Killingsworth et al., 2018), and subject to fractionation between SO<sub>4</sub><sup>2-</sup> and H<sub>2</sub>O (ε<sub>SO<sub>4</sub>-H<sub>2</sub>O</sub>) and between SO<sub>4</sub><sup>2-</sup> and O<sub>2</sub> (ε<sub>SO<sub>4</sub>-O<sub>2</sub></sub>) (Balci et al., 2007; Taylor et al., 1984a). Estimates of ε<sub>SO<sub>4</sub>-H<sub>2</sub>O</sub> range from 0‰ to 4.1‰ (Balci et al., 2007; Lloyd, 1968; Taylor et al., 1984b; van Everdingen and Krouse, 1985) and estimates for ε<sub>SO<sub>4</sub>-O<sub>2</sub></sub> range from -11.4‰ to -8.7‰ (Balci et al., 2007; Lloyd, 1968; Taylor et al., 1984b). The dependence of δ<sup>18</sup>O<sub>SO<sub>4</sub></sub> on δ<sup>18</sup>O<sub>H<sub>2</sub>O</sub> is often removed by evaluating their difference, δ<sup>18</sup>O<sub>SO<sub>4</sub>-H<sub>2</sub>O</sub>, which ranges globally from ~0‰ to nearly 25‰ (Calmels et al., 2007; Relph et al., 2021; Turchyn et al., 2013). Applying the mixing model used to constrain the δ<sup>34</sup>S<sub>SO<sub>4</sub></sub> of sulfuric acid sources (Table 1; Equations 5–10), we calculated that sulfide oxidation produces δ<sup>18</sup>O<sub>SO<sub>4</sub>-H<sub>2</sub>O</sub> values between 2.2 and 14.9‰ in 90% of simulations, with a mean value of 8.2‰. However, given that 25% O<sub>2</sub> incorporation into

$\text{SO}_4^{2-}$  is toward the higher end of possible values and this model allows  $\delta^{18}\text{O}_{\text{O}_2}$  to reach values as high as 70‰ (Relph et al., 2021), the lower end of the estimated range of  $\delta^{18}\text{O}_{\text{SO}_4\text{-H}_2\text{O}}$  values is more likely. Sample  $\delta^{18}\text{O}_{\text{SO}_4\text{-H}_2\text{O}}$  values ranged from 14.5 to 17.1‰ and exceeded the mean model result by 6.3–8.9‰, meaning that the isotopic composition of  $\text{SO}_4^{2-}$  in the Koyukuk River is inconsistent with sulfide oxidation alone (Figure 5). Rather, the ~7.5‰ elevation in  $\delta^{18}\text{O}_{\text{SO}_4\text{-H}_2\text{O}}$  values relative to the mean expectation for sulfide oxidation requires either a  $\text{SO}_4^{2-}$  source with high  $\delta^{18}\text{O}$  values or the catchment-scale expression of a fractionating process such as MSR.

#### 4.1.1.2. Elevated $\delta^{18}\text{O}_{\text{SO}_4\text{-H}_2\text{O}}$ Values are Consistent With Gypsum Dissolution

Our preferred explanation for the elevated  $\delta^{18}\text{O}_{\text{SO}_4\text{-H}_2\text{O}}$  values is that ~20% of the  $\text{SO}_4^{2-}$  in the Koyukuk River derives from the dissolution of evaporative sulfate salts. This interpretation is broadly consistent with the assemblage of sedimentary lithologies in the headwater catchments and with the prior identification of evaporite specifically (Harrison et al., 2011). Sulfate sourced through evaporite dissolution is typically assumed to have  $\delta^{18}\text{O}_{\text{SO}_4}$  values between 10‰ and 20‰ and  $\delta^{34}\text{S}_{\text{SO}_4}$  values between 10‰ and 30‰, matching the range of Phanerozoic evaporites (Claypool et al., 1980). In this case, the low  $\text{Cl}^-/\Sigma^+$  ratios of the headwater and mainstem samples (Figure 3) require the inferred evaporite to contain very little halite.

#### 4.1.1.3. Elevated $\delta^{18}\text{O}_{\text{SO}_4\text{-H}_2\text{O}}$ Values are Inconsistent With Microbial Sulfate Reduction

The second possible interpretation of the elevated  $\delta^{18}\text{O}_{\text{SO}_4\text{-H}_2\text{O}}$  values is motivated by observations from the Marsyandi catchment of the Nepal Himalaya interpreted to reflect that MSR can increase  $\delta^{34}\text{S}_{\text{SO}_4}$  and  $\delta^{18}\text{O}_{\text{SO}_4}$  by preferentially consuming  $\text{SO}_4^{2-}$  isotopologues bearing  $^{32}\text{S}$  and  $^{16}\text{O}$  (Hemingway et al., 2020; Turchyn et al., 2013). By increasing the  $\delta^{34}\text{S}_{\text{SO}_4}$  and  $\delta^{18}\text{O}_{\text{SO}_4}$  values of residual  $\text{SO}_4^{2-}$ , MSR can result in  $\text{SO}_4^{2-}$  isotopic compositions suggestive of evaporite dissolution even when  $\text{SO}_4^{2-}$  is derived from sulfide oxidation. Furthermore, the oxidation of low valent sulfur species back to  $\text{SO}_4^{2-}$  can incorporate environmental oxygen and alter  $\delta^{18}\text{O}_{\text{SO}_4}$  values without necessarily changing  $\delta^{34}\text{S}_{\text{SO}_4}$  values (Mills et al., 2016). Microbial processes have previously been suggested to increase fluvial  $\delta^{34}\text{S}_{\text{SO}_4}$  and  $\delta^{18}\text{O}_{\text{SO}_4}$  values in permafrost settings and other landscapes (Joo et al., 2022; Jones et al., 2020), but there is also evidence that  $\delta^{34}\text{S}_{\text{SO}_4}$  (Kemeny et al., 2021b) and  $\delta^{18}\text{O}_{\text{SO}_4}$  (Burt et al., 2021) can behave conservatively in river systems.

Although we argue in the subsequent section that environmental sulfate reduction likely does explain some variability in  $\delta^{34}\text{S}_{\text{SO}_4}$  values, several lines of analysis argue against MSR as a main mechanism for generating the observed elevation of  $\delta^{18}\text{O}_{\text{SO}_4\text{-H}_2\text{O}}$ . We first need to consider the increase in  $\delta^{34}\text{S}_{\text{SO}_4}$  that would be associated with a microbially driven increase in  $\delta^{18}\text{O}_{\text{SO}_4\text{-H}_2\text{O}}$ . Most straightforward, the 4:1 atom ratio of oxygen to sulfur within sulfate suggests that the magnitude of oxygen isotope fractionation during sulfate reduction would be 25% the magnitude of the sulfur isotope fractionation ( $\Delta\delta^{34}\text{S}_{\text{SO}_4}/\Delta\delta^{18}\text{O}_{\text{SO}_4} = 4$ ), in which case a 7.5‰ increase in  $\delta^{18}\text{O}_{\text{SO}_4\text{-H}_2\text{O}}$  relative to the value formed through sulfide oxidation would require an approximately 30‰ increase in  $\delta^{34}\text{S}_{\text{SO}_4}$  (Grinenko & Ustinov, 1990; Mandernack et al., 2003; Mizutani & Rafter, 1969; Rafter & Mizutani, 1967). However, lower ratios for changes in  $\delta^{34}\text{S}_{\text{SO}_4}$  relative to changes in  $\delta^{18}\text{O}_{\text{SO}_4}$  have been reported at low net sulfate reduction rates and attributed to the influence of partial exchange between  $\text{H}_2\text{O}$  and intermediate sulfur species (Aharon & Fu, 2000; Antler et al., 2013, 2017; Brunner et al., 2005; Fritz et al., 1989; Mills et al., 2016; Mizutani & Rafter, 1973; Turchyn et al., 2010). In samples collected from the Gulf of Mexico, for example, Aharon and Fu (2000) observed the magnitude of oxygen isotope fractionation during sulfate reduction scaling as 71% the magnitude of sulfur isotope fractionation ( $\Delta\delta^{34}\text{S}_{\text{SO}_4}/\Delta\delta^{18}\text{O}_{\text{SO}_4} \sim 1.4$ ). Similarly, Antler et al. (2013) observed  $\Delta\delta^{34}\text{S}_{\text{SO}_4}/\Delta\delta^{18}\text{O}_{\text{SO}_4}$  near 1 in samples collected from the Eastern Mediterranean. At these ratios for relative fractionation, generating a 7.5‰ increase in  $\delta^{18}\text{O}_{\text{SO}_4\text{-H}_2\text{O}}$  would require increasing river  $\delta^{34}\text{S}_{\text{SO}_4}$  by only 7.5–10.5‰ relative to sulfuric acid sources. Given that measured Koyukuk River mainstem  $\delta^{34}\text{S}_{\text{SO}_4}$  values were ~0‰, explaining observations of elevated  $\delta^{18}\text{O}_{\text{SO}_4\text{-H}_2\text{O}}$  values through MSR would thus require that the weighted  $\delta^{34}\text{S}$  of sulfuric acid sources was between approximately -7.5‰ and -30‰, depending on the  $\Delta\delta^{34}\text{S}_{\text{SO}_4}/\Delta\delta^{18}\text{O}_{\text{SO}_4}$  ratio characterizing MSR. As further described below, the existence of sulfuric acid sources with such low values of  $\delta^{34}\text{S}$  is unlikely because we did not observe low- $\delta^{34}\text{S}$  solid phases in floodplain sediment and because the degree of reaction required to generate measured  $\delta^{34}\text{S}_{\text{SO}_4}$  values from such a substrate would be very large.

For MSR to explain sulfur isotope ratios of river  $\text{SO}_4^{2-}$  at a catchment-scale requires storing or exporting reaction products with low  $\delta^{34}\text{S}$  values (Torres et al., 2015). In particular, products of MSR would have  $\delta^{34}\text{S}$  values even lower than the -7.5‰ to -30‰ of the inferred sulfuric acid source. However, our observations of  $\delta^{34}\text{S}_{\text{sediment}}$

were comparable to mainstem river  $\delta^{34}\text{S}_{\text{SO}_4}$  and had only modest sulfur abundances ( $\leq 0.18$  wt%; Figures 5b and 7). It is unlikely that sulfide with low  $\delta^{34}\text{S}$  values was exported from the catchment as reduced inorganic phases (Johnson et al., 2014), although it is possible but speculative that product  $\text{H}_2\text{S}$  with low  $\delta^{34}\text{S}$  values degassed into the atmosphere. It is also possible that the sediment samples we analyzed are not representative of the sites where MSR occurs because sediment was collected from the floodplain surrounding Huslia while elevated values of  $\delta^{18}\text{O}_{\text{SO}_4}$  were also measured in the headwater samples (Figure 5). Even in this case, however, the fractional substrate consumption required to increase  $\delta^{34}\text{S}_{\text{SO}_4}$  by 7.5–30‰ also argues against MSR substantially impacting the isotopic ratios of  $\text{SO}_4^{2-}$  in our samples.

When evaluating isotopic fractionation within rivers, it is important to account for the fact that individual samples reflect mixtures of different waters sampling a distribution of landscape transit times (Druhan & Maher, 2014, 2017). In the distillation equation of Druhan and Maher (2017) that accounts for mixing of partially reacted reservoirs (Equation 20 in their paper), the magnitude of the fractionation factor ( $\alpha$ ) and the initial isotope ratio ( $R_{\text{initial}}$ ) relative to the isotopic standard ( $R_{\text{standard}}$ ) set the maximum attainable isotopic difference between the initial and final substrate ( $\Delta\delta$ ) as  $10^3 \times (R_{\text{initial}}/R_{\text{standard}}) \times (1/\alpha - 1)$ . In the case of sulfur, the difference in  $\delta^{34}\text{S}$  between sources of sulfuric acid and  $\delta^{34}\text{S}_{\text{SO}_4}$  is closely approximated as  $-f \times \epsilon_{\text{MSR}}$ , where  $f$  is the fractional utilization of  $\text{SO}_4^{2-}$  and  $\epsilon_{\text{MSR}}$  is the relevant isotope effect; this formulation is unlike a standard Rayleigh distillation wherein the isotopic difference between a substrate's initial and final compositions is unbounded (Druhan & Maher, 2017; Hayes, 2004). At the highest observed MSR isotope effects of  $\epsilon_{\text{MSR}} \sim -70\text{‰}$  (Sim, Bosak, & Ono, 2011) and for  $\Delta\delta^{34}\text{S}_{\text{SO}_4}/\Delta\delta^{18}\text{O}_{\text{SO}_4}$  ratios between 1 and 4, between 11% and 43% of fluvial  $\text{SO}_4^{2-}$  would need to be reduced to generate a 7.5‰ increase in  $\delta^{18}\text{O}_{\text{SO}_4\text{-H}_2\text{O}}$ . However, such large isotope fractionations are generally expressed only in quiescent environments at low sulfate reduction rates (Fike et al., 2015; Leavitt et al., 2013; Sim, Ono, et al., 2011), conditions that are unlikely to be met in highly energetic eroding headwater catchments. At moderate isotope effects, such as  $-35\text{‰}$ , between 21% and 86% of fluvial  $\text{SO}_4^{2-}$  would need to be reduced to generate a 7.5‰ increase in  $\delta^{18}\text{O}_{\text{SO}_4\text{-H}_2\text{O}}$ . The upper portion of this range is implausible given the extremely high  $\text{SO}_4^{2-}$  concentrations still present in the headwater samples.

Overall, the observations of  $\delta^{34}\text{S}_{\text{sediment}}$  values comparable to mainstem  $\delta^{34}\text{S}_{\text{SO}_4}$  and the required fraction of substrate consumption indicate that biological processes are not likely responsible for observed values of  $\delta^{18}\text{O}_{\text{SO}_4\text{-H}_2\text{O}}$ . The small amount of  $\text{SO}_4^{2-}$  reduction permitted by the data is not of the magnitude required to increase mainstem  $\delta^{34}\text{S}_{\text{SO}_4}$  values by 7.5–30‰. Rather, we conclude that elevated  $\delta^{18}\text{O}_{\text{SO}_4\text{-H}_2\text{O}}$  values more likely reflect a  $\text{SO}_4^{2-}$  contribution from dissolution of sulfate salts. This interpretation is also more conservative than attributing all river  $\text{SO}_4^{2-}$  to sulfide oxidation; the calculated influence of sulfide oxidation on  $p\text{CO}_2$  would be larger if elevated  $\delta^{18}\text{O}_{\text{SO}_4\text{-H}_2\text{O}}$  values were due to microbial sulfur cycling.

#### 4.1.2. Sulfur Isotope Variation and Sulfur Cycling Within the Koyukuk River Catchment

Values of  $\delta^{34}\text{S}_{\text{SO}_4}$  and  $\delta^{18}\text{O}_{\text{SO}_4}$  in mainstem samples were comparable to those in the MF sample but differed from values in samples from the other headwater catchments. Moreover, the isotopic distinctions among headwater sites were unusual in that the MF sample had higher  $\delta^{34}\text{S}_{\text{SO}_4}$  but lower  $\delta^{18}\text{O}_{\text{SO}_4}$  values than the other headwater samples (Figure 5). Although microbial processes could increase  $\delta^{34}\text{S}_{\text{SO}_4}$  and  $\delta^{18}\text{O}_{\text{SO}_4}$  together or impact the  $^{18}\text{O}/^{16}\text{O}$  ratio independent from  $^{34}\text{S}/^{32}\text{S}$  (Mills et al., 2016), we are not aware of processes that could increase  $^{34}\text{S}/^{32}\text{S}$  while decreasing  $^{18}\text{O}/^{16}\text{O}$  at the measured values of  $\delta^{18}\text{O}_{\text{H}_2\text{O}}$ . A more parsimonious explanation of these observations is likely that the four headwater catchments differ isotopically because they are weathering distinct materials. A quarry within pyrite-rich gabbro exists several miles south of the SC sampling site and is reported to contain centimeter-scale pyrite cubes. We suggest that waters collected near this mine might not represent the headwater areas but instead reflect local weathering of an isotopically distinct bedrock. Because the MF sample has the largest upstream area and highest concentrations of dissolved  $\text{Ca}^{2+}$ ,  $\text{Mg}^{2+}$ , and  $\text{SO}_4^{2-}$  among the sampled headwater sites (Figure 1c), we considered this sample as the best description of weathering in the headwaters.

Consistent with the interpretation that the MF sample captures the most representative headwater conditions, values of  $\delta^{34}\text{S}_{\text{SO}_4}$  in the Koyukuk mainstem samples fall on a mixing line between the MF sample and the four precipitation samples (Figure 4a, Figures S3 and S4 in Supporting Information S1). Within this mixing framework, the  $\delta^{34}\text{S}_{\text{SO}_4}$  values of slough samples were higher than expected based on  $\text{Cl}^-/\text{SO}_4^{2-}$  ratios and the  $\delta^{34}\text{S}_{\text{SO}_4}$  values of pore fluid were mostly lower than expected based on  $\text{Cl}^-/\text{SO}_4^{2-}$  ratios (Figure 4a). We attribute these deviations to a combination of mixing and biological processing through assimilatory and dissimilatory  $\text{SO}_4^{2-}$  reduction. Mixing between the mainstem river and precipitation would generate large variation in  $\text{Cl}^-/\text{SO}_4^{2-}$

but only minor changes in  $\delta^{34}\text{S}_{\text{SO}_4}$ . For example, sourcing 2% of  $\text{SO}_4^{2-}$  from precipitation would modify  $\text{Cl}^-/\text{SO}_4^{2-}$  by nearly an order of magnitude from the ratio in the MF sample while the shift in  $\delta^{34}\text{S}_{\text{SO}_4}$  would be within analytical uncertainty. Conversely, partial consumption of  $\text{SO}_4^{2-}$  through a fractionating process could modify  $\delta^{34}\text{S}_{\text{SO}_4}$  values but would only minimally impact the  $\text{Cl}^-/\text{SO}_4^{2-}$  ratio relative to the multiple order-of-magnitude observed range (Figure 4a).

The  $\delta^{34}\text{S}_{\text{SO}_4}$  offset between slough and mainstem samples could be due to assimilatory  $\text{SO}_4^{2-}$  reduction, which carries only a small fractionation, rather than the highly fractionating process of dissimilatory MSR (Sim, Bosak, & Ono, 2011; Trust & Fry, 1992). Assimilatory  $\text{SO}_4^{2-}$  reduction in plants, in which environmental  $\text{SO}_4^{2-}$  is taken up into biomass, has a variable but small fractionation around  $-1.5\%$  (Tcherkez & Tea, 2013; Trust & Fry, 1992). Modest amounts of assimilatory  $\text{SO}_4^{2-}$  reduction in the sloughs are also supported by XANES observations of common organic sulfur phases within both floodplain sediment and suspended sediment (Figure 8). Conversely, the observation that slough samples with elevated  $\delta^{34}\text{S}_{\text{SO}_4}$  values also have lower  $\delta^{13}\text{C}_{\text{DIC}}$  values and reduced  $\text{SO}_4^{2-}/\text{DIC}$  ratios suggests a modest amount of dissimilatory  $\text{SO}_4^{2-}$  reduction (Figure 6c). The intermediate  $\text{Cl}^-/\text{SO}_4^{2-}$  and  $\delta^{34}\text{S}_{\text{SO}_4}$  values of the slough samples are thus interpreted to result both from mixing of the mainstem river with precipitation and a combination of assimilatory and dissimilatory biological  $\text{SO}_4^{2-}$  reduction. Note that the suggested magnitude of MSR is much smaller than the catchment-scale expression which would be required to explain elevated values of  $\delta^{18}\text{O}_{\text{SO}_4\text{-H}_2\text{O}}$ .

Opposite the slough samples, pore fluid  $\delta^{34}\text{S}_{\text{SO}_4}$  values tended to be lower than expected from  $\text{Cl}^-/\text{SO}_4^{2-}$  ratios (Figure 4a). These low values likely also result from biological sulfate reduction in the floodplain subsurface but reflect the product sulfur rather than the reactant  $\text{SO}_4^{2-}$ . That is, we interpret the low pore fluid  $\delta^{34}\text{S}_{\text{SO}_4}$  values as reflecting the oxidized product of either sulfide formed through dissimilatory  $\text{SO}_4^{2-}$  reduction or  $\text{S}_{\text{org}}$  produced through assimilatory  $\text{SO}_4^{2-}$  reduction.

In addition, pore fluid observations across a transect orthogonal to the active channel reveal relationships among  $\text{SO}_4^{2-}$  concentration,  $\delta^{34}\text{S}_{\text{SO}_4}$  values, and proximity to the river. Pore fluid samples from this transect ranged from a  $\text{SO}_4^{2-}$  concentration of 24  $\mu\text{M}$  at a  $\delta^{34}\text{S}_{\text{SO}_4}$  value of 0.1‰ furthest from the active channel to a  $\text{SO}_4^{2-}$  concentration of 1,591  $\mu\text{M}$  at a  $\delta^{34}\text{S}_{\text{SO}_4}$  value of  $-6.0\%$  closest to the active channel (Figure S6 in Supporting Information S1). The accumulation of  $\text{SO}_4^{2-}$  and decline of  $\delta^{34}\text{S}_{\text{SO}_4}$  values close to the channel suggests sulfur cycling, potentially linked to seasonal changes in the supply of  $\text{SO}_4^{2-}$ ,  $\text{O}_2$ , and  $\text{C}_{\text{org}}$  due to changes in river stage and floodplain hydrology. Conversely, the lower  $\text{SO}_4^{2-}$  concentrations and higher  $\delta^{34}\text{S}_{\text{SO}_4}$  values in pore fluids far from the channel suggest more complete  $\text{SO}_4^{2-}$  consumption and relative chemical isolation from direct fluvial influences.

Mixing and sulfate reduction, while consistent with observations of  $\delta^{34}\text{S}_{\text{SO}_4}$  and  $\text{Cl}^-/\text{SO}_4^{2-}$ , are insufficient to explain relationships between  $\delta^{34}\text{S}_{\text{SO}_4}$  and  $(\text{Ca}^{2+} + \text{Mg}^{2+})/\text{SO}_4^{2-}$  (Figure 4b). The ratios of  $\text{Ca}^{2+}/\text{SO}_4^{2-}$  and  $\text{Mg}^{2+}/\text{SO}_4^{2-}$  in samples from both sloughs and pore fluids exceed those in mainstem and precipitation samples and suggest another source of alkaline cations. This source is unlikely to be evaporite dissolution, which has  $(\text{Ca}^{2+} + \text{Mg}^{2+})/\text{SO}_4^{2-} = 1$ . Rather, we interpret the observations as reflecting the input of carbonate and silicate weathering products, the former of which is also constrained by the relationship of  $\delta^{13}\text{C}_{\text{DIC}}$  to  $(\text{Ca}^{2+} + \text{Mg}^{2+})/\text{DIC}$  (Figure 6b).

#### 4.2. Timescale-Dependent Impacts of Koyukuk River Weathering on the Global Carbon Cycle

The MEANDIR model was used to quantify the relative contributions to river dissolved load from carbonate weathering, silicate weathering, sulfide oxidation, organic carbon oxidation, gypsum dissolution, meteoric precipitation, and carbon degassing (Figure 9). While many of these processes are associated with gross inversion-constrained fluxes of ALK and/or IC, calculating the net impact of the fluxes on  $p\text{CO}_2$  requires making assumptions regarding additional and unquantified biogeochemical processes within the weathering system. In particular, if the inversion-constrained  $\text{C}_{\text{org}}$  oxidation represents oxidation of recently fixed biospheric  $\text{C}_{\text{org}}$ , rather than petrogenic  $\text{C}_{\text{org}}$ , the flux would not constitute a meaningful part of the landscape's net weathering budget. Including the inversion-constrained DIC flux from  $\text{C}_{\text{org}}$  oxidation in the calculation of  $\Delta\text{ALK}/\Delta\text{IC}$  would implicitly categorize that carbon as a new flux to the ocean-atmosphere system (i.e., from aged carbon in rocks or floodplain deposits) and not account for any component merely returning IC that was only recently fixed from atmospheric  $\text{CO}_2$  (Hilton et al., 2014; Horan et al., 2017, 2019). Because the observed values of  $F_{\text{mod-DIC}}$  in the Koyukuk River are nearly modern, ranging from 0.9432 to 1.0191, for simplicity we assume the entire  $\text{C}_{\text{org}}$  reservoir was fixed recently and do not include its oxidation when calculating the net flux of IC to the ocean-atmosphere system. Notably, this



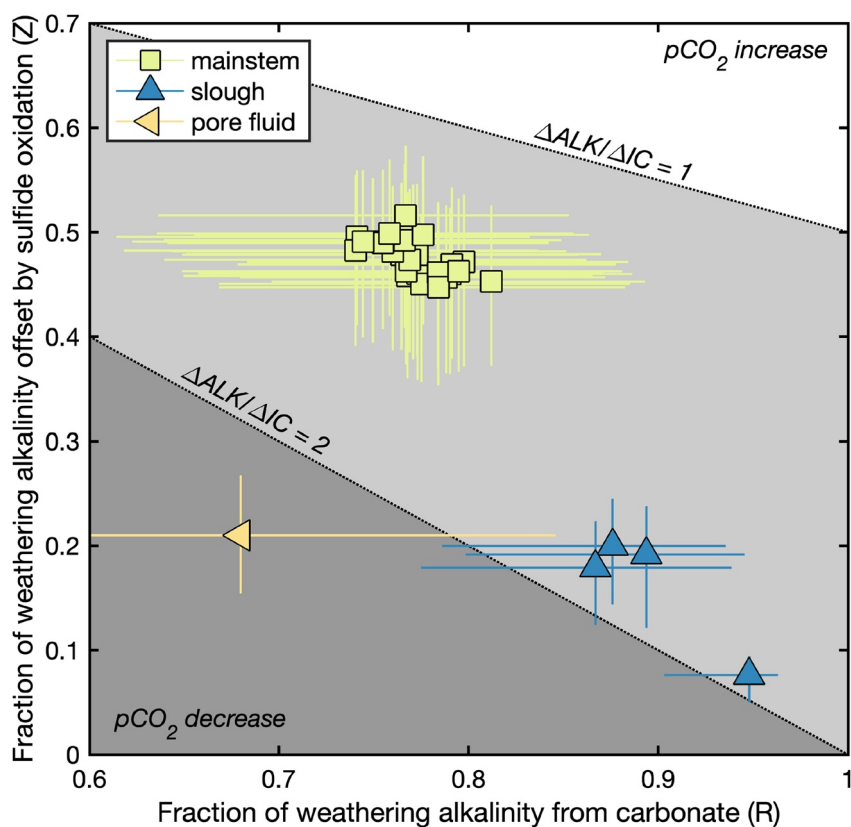


**Figure 11.** Carbon cycle impacts of chemical weathering in the Koyukuk River catchment. Inversion-constrained median fraction of weathering ALK offset by sulfide oxidation ( $Z$ ) against the median fraction of weathering ALK from carbonate weathering ( $R$ ). Reference lines and shading are shown for  $\Delta\text{ALK}/\Delta\text{IC} = 1$  and  $\Delta\text{ALK}/\Delta\text{IC} = 2$ . Inversion results show that  $\Delta\text{ALK}/\Delta\text{IC}$  is  $>1$  for samples from both the mainstem and the sloughs, corresponding to weathering that decreases  $p\text{CO}_2$  on timescales shorter than the  $\sim 10$  Kyr timescale of carbonate compensation. Error bars range from 5th to 95th percentiles of inversion results.

simplification does not account for aged carbon subject to rapid oxidation upon thaw (Drake et al., 2015; Vonk et al., 2013). Under this assumption, our  $\Delta\text{ALK}/\Delta\text{IC}$  calculations represent maximum estimates with respect to  $\text{C}_{\text{org}}$  oxidation; if we included a petrogenic source in the calculation, as possibly suggested by measurements of  $^{14}\text{C}$  activity in sedimentary  $\text{C}_{\text{org}}$  (Douglas et al., 2022), it would result in lower  $\Delta\text{ALK}/\Delta\text{IC}$  ratios.

The inversion found that mainstem samples had lower median fractions of carbonate weathering and higher median fractions of sulfuric acid weathering than the slough samples (Figure 11), corresponding to lower median  $R$  values and higher median  $Z$  values. The inversion-constrained  $\Delta\text{ALK}/\Delta\text{IC}$  ratio of weathering was between 1 and 2 in mainstem samples and nearly 2 in slough samples. These ratios were insensitive to removing degassing from the inversion or allowing for degassing to remove up to 25 times measured DIC concentrations (Figure S15 in Supporting Information S1), and the ratios in mainstem samples were insensitive to changes in the range of allowable degassing fractionation factors (Figure S16 in Supporting Information S1). Because modern  $p\text{CO}_2$  decreases for sets of weathering processes with  $\Delta\text{ALK}/\Delta\text{IC} > 1$ , the results illustrate that inorganic chemical weathering throughout the Koyukuk River acts to decrease  $p\text{CO}_2$  on timescales shorter than the  $\sim 5$ – $10$  kyr timescale expected of carbonate compensation. For the Koyukuk River system at present, chemical weathering viewed over human timescales constitutes a  $\text{CO}_2$  sink. In other words, the contribution from sulfuric acid production to the dissolved load is significant, but not so significant as to tilt the mineral weathering system to be a net  $\text{CO}_2$  source over decadal-centennial timescales.

When considered over a longer timescale (e.g.,  $>10$  kyrs), the burden of weathering on the ocean-atmosphere systems depends on the value of  $\Delta\text{ALK}/\Delta\text{IC}$  relative to the 2:1 ALK:DIC ratio of marine carbonate formation. Because the ALK consumed during sulfide oxidation is approximately equal to the ALK produced during silicate weathering in sloughs, these samples record chemical weathering that is  $\text{CO}_2$ -neutral on the longer timescale

(Figure 11). Conversely, in mainstem samples, ALK consumed during sulfide oxidation exceeds ALK produced during silicate weathering and chemical denudation is a source of  $\text{CO}_2$ . This type of carbon cycle response, which occurs when  $\Delta\text{ALK}/\Delta\text{IC}$  is greater than 1, but less than 2, tends to characterize weathering in systems of high erosion like mountain-front sites in the Peruvian Andes (Torres et al., 2016) and the Nepal Himalaya (Kemeny et al., 2021a), rather than floodplains that often serve as sites of intense silicate weathering with carbonic acid (Lupker et al., 2012). Although still a net  $\text{CO}_2$  sink over short timescales, the  $\Delta\text{ALK}/\Delta\text{IC}$  ratios of the Koyukuk River mainstem samples are relatively low for their topographic setting (a lowland floodplain). Such low  $\Delta\text{ALK}/\Delta\text{IC}$  ratios may indicate that the development of thermokarst and associated rapid exposure of sediment may be important in the Koyukuk River catchment (Zolkos et al., 2018, 2019).

We were not able to uniquely establish the fraction of DIC sourced from petrogenic  $\text{C}_{\text{org}}$  in the Koyukuk River and this remains a target for future research (Drake et al., 2018a). If the inversion-constrained  $\text{C}_{\text{org}}$  oxidation derives from petrogenic material, the DIC flux would be comparable but slightly lower than the sulfide-derived  $\text{SO}_4^{2-}$  flux in mainstem samples and would greatly exceed the sulfide-derived  $\text{SO}_4^{2-}$  flux in slough samples (Figure 9). Understanding the balance of biospheric  $\text{C}_{\text{org}}$  is likewise important (Lininger et al., 2018). If modern particulate  $\text{C}_{\text{org}}$  fluxes are approximately balanced (Douglas et al., 2022), the dominant influence of chemical weathering on  $p\text{CO}_2$  would derive from sulfide oxidation and petrogenic  $\text{C}_{\text{org}}$  oxidation. Alternatively, when considering Arctic greening or shrubification as a net sink for  $\text{CO}_2$ , the growth of new biomass would need to compensate for ALK lost through sulfide oxidation to result in net  $p\text{CO}_2$  decrease (Liu et al., 2020; Myers-Smith et al., 2020; Tape et al., 2006).

### 4.3. Temporal Trends in the Koyukuk River and Yukon River

We hypothesize that the decade-scale increases in the concentration of fluvial  $\text{SO}_4^{2-}$  and  $\text{Mg}^{2+}$ , as well as the increasing ratios of  $\text{SO}_4^{2-}/\Sigma^+$  and  $\text{Mg}^{2+}/\Sigma^+$  (Figure 10), likely reflect shifts in weathering dynamics within the Koyukuk River. Evaluating seasonal weathering dynamics in the Yukon River can provide useful context for understanding decadal changes in the dissolved chemistry of the Koyukuk River. On decadal timescales, the Yukon River at Pilot Station also shows increases in  $\text{SO}_4^{2-}/\Sigma^+$  and  $\text{Mg}^{2+}/\Sigma^+$  ratios (Figure 12; Toohey et al., 2016). Moreover, the data exhibit seasonal variations in which the  $\text{SO}_4^{2-}/\Sigma^+$  and  $\text{Mg}^{2+}/\Sigma^+$  ratios rise during summer and decline during winter. Although there are important distinctions between seasonal and long-term changes in chemical weathering dynamics, with the former reflecting the position of the water or frost tables and the latter the availability of weatherable material and large-scale hydrology, we speculate that seasonal changes within permafrost landscapes might be comparable to decadal weathering patterns because both timescales are governed by thaw rather than tectonic uplift.

During winter months, low discharge in the Yukon River at Pilot Station is sustained by groundwater with low  $\text{SO}_4^{2-}/\Sigma^+$  and moderate  $\text{Ca}^{2+}/\Sigma^+$  and  $\text{Mg}^{2+}/\Sigma^+$  ratios (Figure 13). These waters are thought to reflect longer flow paths with extended residence times that, as indicated by their elevated  $\text{Si}/\Sigma^+$  ratios, have sufficient time to accumulate silicate weathering products (Tipper et al., 2006). Discharge then rapidly rises in May and June and the  $\text{Ca}^{2+}/\Sigma^+$  and  $\text{SO}_4^{2-}/\Sigma^+$  ratios increase as the absolute concentrations of  $\text{Ca}^{2+}$ ,  $\text{Mg}^{2+}$ , and  $\text{SO}_4^{2-}$  decline (Figure 13b). During these months, water in the active channel is thought to follow shallower flow paths with short residence times that favor kinetically rapid reactions such as carbonate weathering, sulfide oxidation, and salt dissolution (Lehn et al., 2017; Tipper et al., 2006). Enhanced carbonate weathering during this interval is also consistent with decreases in the  $\text{DIC}/\Sigma^+$  and  $\text{Si}/\Sigma^+$  ratios (Figures 12g and 12h). The summer months display discharge intermediate between winter and spring, and water in the active channel is expected to derive from flow paths with intermediate residence times. Counterintuitively, the relative abundances of  $\text{Mg}^{2+}$  and  $\text{SO}_4^{2-}$  are higher during the summer than in any other season. Moreover, despite the higher summer discharge, the concentration of  $\text{SO}_4^{2-}$  during the summer is comparable or elevated relative to wintertime  $\text{SO}_4^{2-}$  concentrations. A spring-to-summer shift from elevated  $\text{Ca}^{2+}/\Sigma^+$  ratios to elevated  $\text{Mg}^{2+}/\Sigma^+$  ratios is also seen in other timeseries sites within the Yukon River Basin (Figures S20–S25 in Supporting Information S1).

Our interpretation of the summertime increases in  $\text{SO}_4^{2-}/\Sigma^+$  and  $\text{Mg}^{2+}/\Sigma^+$  is that, due to the seasonal thaw of the active layer, summertime flow paths are able to access mineral phases that were previously frozen in the deeper portion of the active layer and that were previously weathered out of the surface layer (Barker et al., 2014; Keller et al., 2007, 2010; Kokelj & Burn, 2003, 2005). The large shifts in  $\text{Ca}^{2+}/\Sigma^+$  and  $\text{Mg}^{2+}/\Sigma^+$  ratios with only minor shifts in  $\text{Si}/\Sigma^+$  suggest that these changes could be related to dolomite weathering, rather than shifts in weathering of Mg-silicate, although the varying and time-dependent  $\text{Mg}^{2+}/\text{Si}$  ratios of tributaries contributing solutes to the

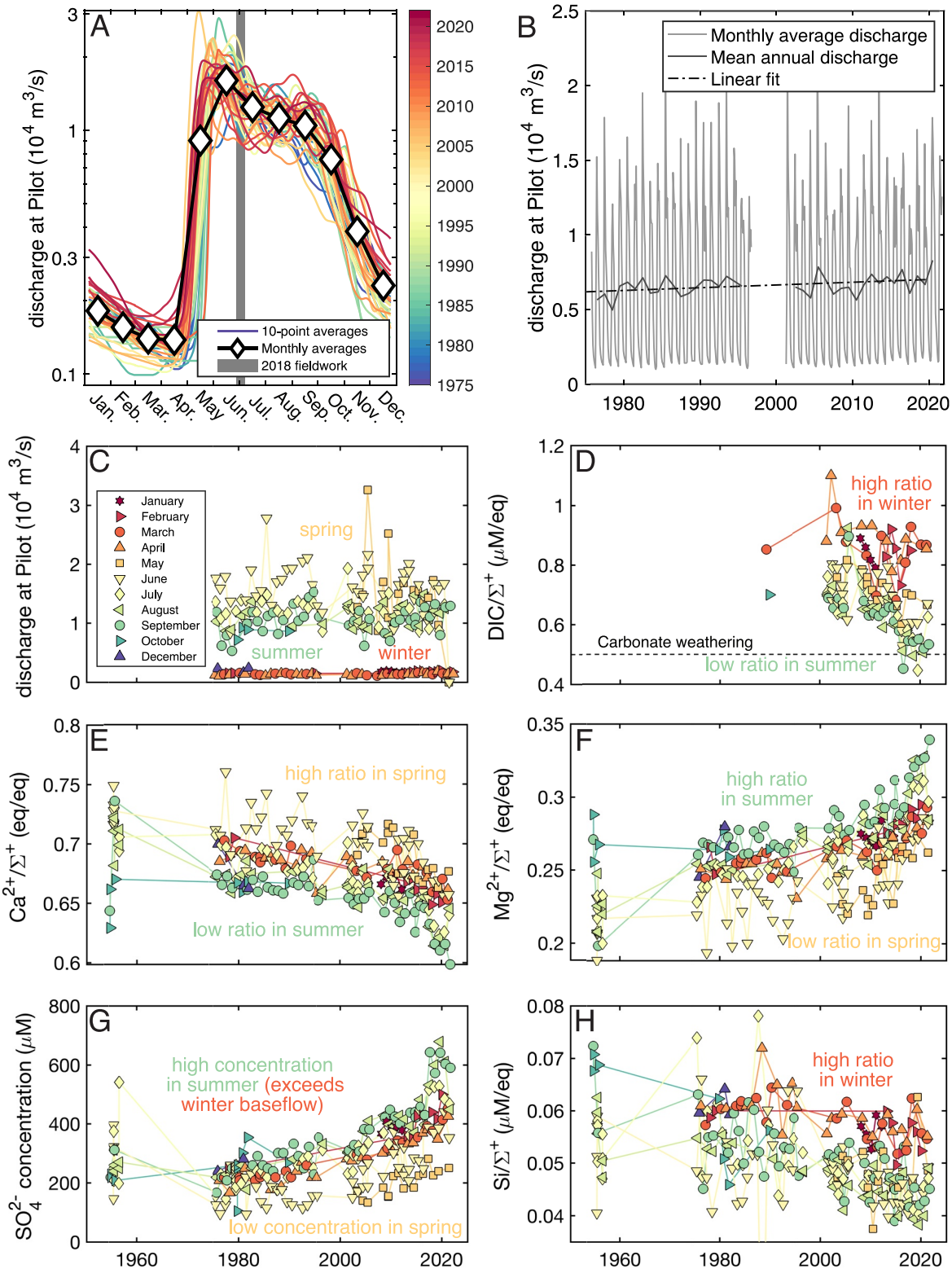


**Figure 12.** Major ion chemistry in the Yukon River at Pilot Station. (a) Monthly averages and 10-point moving averages for discharge between 1975 and 2021, (b) continuous discharge, and (c) discharge during sample collection. Discharge was typically highest in June and elevated for July through October before dropping to base flow. (d) DIC/ $\Sigma^+$ , (e)  $\text{Ca}^{2+}/\Sigma^+$ , (f)  $\text{Mg}^{2+}/\Sigma^+$ , (g)  $\text{SO}_4^{2-}$  concentration, and (h)  $\text{Si}/\Sigma^+$ .  $\text{Ca}^{2+}/\Sigma^+$  is typically highest during the period of elevated discharge in June and lowest during the summer.  $\text{Mg}^{2+}/\Sigma^+$  exhibits the opposite behavior and is lowest during May and June and highest during September.  $\text{SO}_4^{2-}$  concentration is lowest during the spring but is elevated above winter values during the summer months.

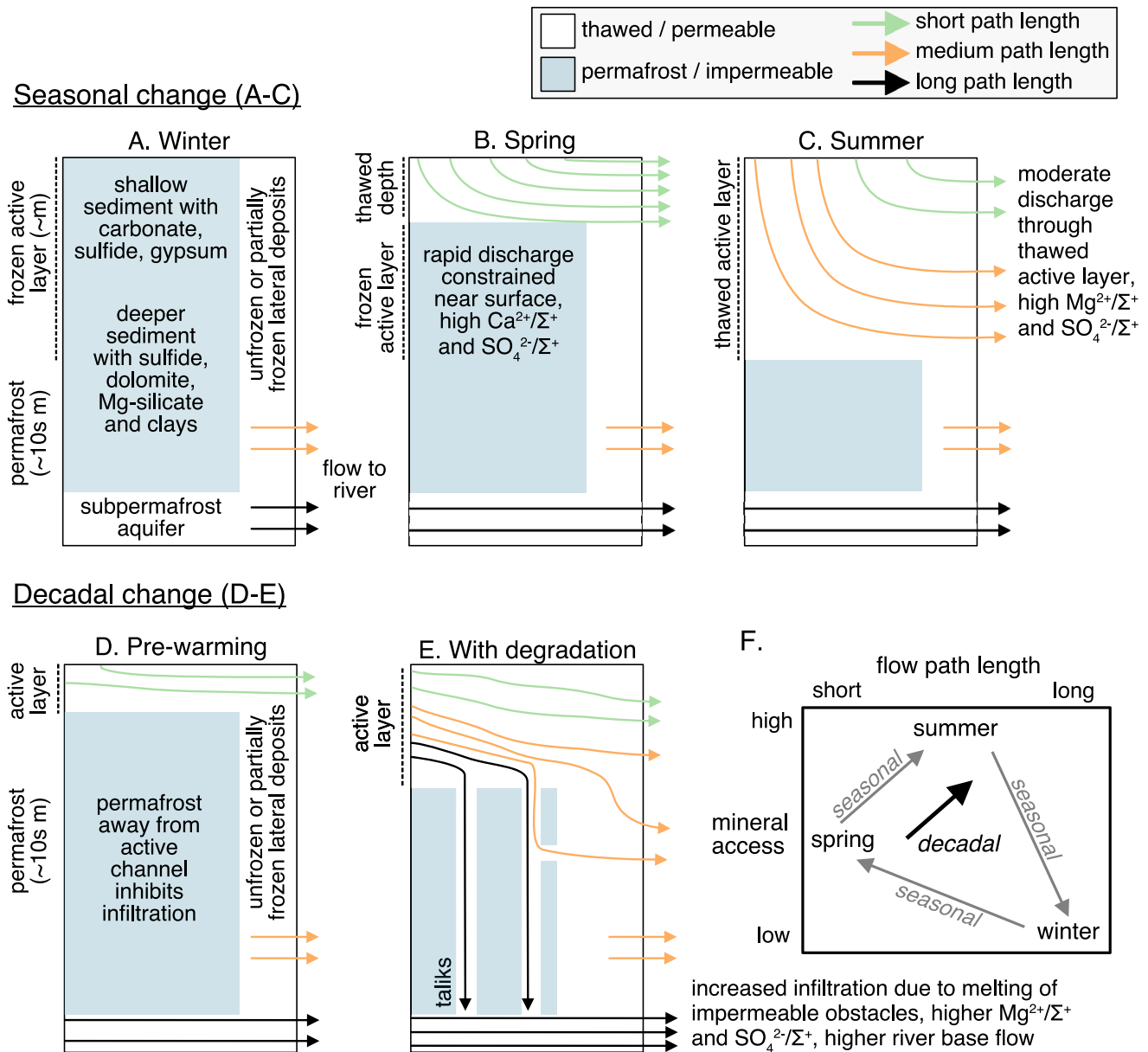


**Figure 13.** Schematic of seasonal and decadal changes due to permafrost thaw. (a) Base flow in permafrost landscapes is low during the winter months. (b) Spring flooding in May and June is focused near the thawed shallow surface. The spring flow paths have short residence times and result in lower  $\text{Ca}^{2+}$ ,  $\text{Mg}^{2+}$ , and  $\text{SO}_4^{2-}$  concentrations than during the winter but higher  $\text{Ca}^{2+}/\Sigma^+$  and  $\text{SO}_4^{2-}/\Sigma^+$  ratios. (c) Flow in the late summer passes through the full thickness of the active layer. These flow paths have longer residence times and access to minerals that have already been removed from shallower layers of the profile (Keller et al., 2007, 2010), resulting in  $\text{SO}_4^{2-}$  concentrations comparable to the wintertime concentrations and  $\text{Mg}^{2+}/\Sigma^+$  ratios exceeding  $\text{Ca}^{2+}/\Sigma^+$  ratios. (d) Prior to warming, river base flow was impeded by impermeable permafrost. (e) Base flow is now increasing due to the removal of impermeable permafrost and has elevated ratios of  $\text{Mg}^{2+}/\Sigma^+$  and  $\text{SO}_4^{2-}/\Sigma^+$ . (f) The data from Pilot Station indicate a seasonal cycle with variations between flow path length and mineral access. On decadal timescales, dissolved chemistry is trending toward the summertime condition.

Yukon River complicates this interpretation. Alternatively, the rise in  $\text{Mg}^{2+}/\Sigma^+$  and reduction in  $\text{Ca}^{2+}/\Sigma^+$  might indicate release of  $\text{Mg}^{2+}$  and uptake of  $\text{Ca}^{2+}$  from the ion exchange pool as discharge and temperature evolve throughout the summer, or potentially changes in weathering of salt (Cleve et al., 1993; Dyrness & Cleve, 1993).

Analogous to seasonal processes, increases in  $\text{SO}_4^{2-}/\Sigma^+$  and  $\text{Mg}^{2+}/\Sigma^+$  on decadal timescales within the Yukon River and Koyukuk River likely reflect changes in flow paths, enhanced subsurface connectivity, exposure of previously inaccessible phases, and/or clay-mediated ion exchange reactions (Figures 13d and 13e; Woo, 1986; Tipper et al., 2006). Part of the elevated  $\text{SO}_4^{2-}$  flux and higher  $\text{SO}_4^{2-}/\Sigma^+$  ratio likely reflects enhanced



sulfide oxidation. However, we could not robustly distinguish between  $\text{SO}_4^{2-}$  sourced from the weathering of sulfide-bearing phases and the dissolution of deposits that contain sulfate salts. Future work to constrain changing base flow chemistry in rivers flowing through permafrost, as diagnosed through isotopic measurements of seasonal samples, could distinguish among different mechanisms for the increase in  $\text{SO}_4^{2-}$  flux and changing  $\text{SO}_4^{2-}/\Sigma^+$  and  $\text{Mg}^{2+}/\Sigma^+$  ratios.

While the observations from the Koyukuk River are consistent with changes in weathering dynamics secondary to permafrost thaw, it is also possible that mining activities over the preceding decades have exposed sulfide and carbonate minerals throughout the catchment (van Stempvoort et al., 2023). Indeed, both the MF and SF of the Koyukuk headwaters have hosted mines in the past (Brabets et al., 2000). The current observations have little power to discern between mining and thaw as both mechanisms impact fluvial chemistry by exposing previously inaccessible minerals to surface weathering conditions. Future work comparing dissolved trace element concentrations with known sites of anthropogenic disturbance might help to distinguish between these explanations. Alternatively, anthropogenic inputs of  $\text{SO}_4^{2-}$  through atmospheric deposition could theoretically explain part of the observed increases in  $\text{SO}_4^{2-}$  concentration and  $\text{SO}_4^{2-}/\Sigma^+$  (Berner, 1971). We consider such inputs unlikely, however, because anthropogenic  $\text{SO}_2$  emissions have been declining since approximately 1970 in the United States and since 1975 in Europe (Gislason & Torssander, 2006), because the magnitude of the  $\text{SO}_4^{2-}$  change is substantially larger than could reasonably be attributed to pollutants, and because anthropogenic inputs would not necessarily explain the changing relative abundances of  $\text{Ca}^{2+}$  and  $\text{Mg}^{2+}$ .

## 5. Conclusions

Permafrost landscapes include large reservoirs of organic carbon, sulfur, and silicate and carbonate minerals susceptible to weathering under a warming climate. Here we report geochemical observations of water and sediment samples collected from the Koyukuk River in central Alaska, a major tributary to the Yukon River that drains discontinuous permafrost. Using isotopic analysis and the MEANDIR inversion model, we find that sulfide oxidation sources the majority of  $\text{SO}_4^{2-}$  in mainstem samples and that assimilatory and dissimilatory sulfate reduction within the floodplain modestly impact  $\delta^{34}\text{S}_{\text{SO}_4}$  values, most notably in floodplain waters such as sloughs and pore fluids. ALK loss due to sulfide oxidation outpaces ALK generation through silicate weathering within mainstem samples but dominance of carbonate weathering results in  $\Delta\text{ALK}/\Delta\text{IC} > 1$ . Chemical weathering in the Koyukuk River catchment is thus a  $\text{CO}_2$  sink on timescales shorter than the 5–10 kyr timescale of carbonate compensation. Chemical weathering, as reflected in mainstem samples, is a  $\text{CO}_2$  source on timescales longer than carbonate compensation but shorter than the approximately 10 Myr residence time of marine  $\text{SO}_4^{2-}$ . Furthermore, comparison with prior data suggests that the absolute and relative importance of sulfide oxidation in the Koyukuk River has increased over the past five decades. In particular, the increase in  $\text{SO}_4^{2-}/\Sigma^+$  through time suggests thaw-induced sulfide oxidation and chemical weathering that increasingly acts as a source of  $\text{CO}_2$ . However, we also acknowledge the potential for changes in the extent of gypsum dissolution or anthropogenic contributions from mining activity. In the future, it will be fruitful to measure isotopic parameters in seasonal water samples to further interrogate annual and decadal changes in the  $\Delta\text{ALK}/\Delta\text{IC}$  weathering ratio.

## Conflict of Interest

The authors declare no conflicts of interest relevant to this study.

## Data Availability Statement

All chemical observations are available as supplementary materials. The MEANDIR inversion model used in this manuscript is archived with Zenodo (Kemeny, 2023) and new editions will be released through GitHub (<https://github.com/PrestonCosslettKemeny/MEANDIR>). USGS data was downloaded from the National Water Information System or digitized from reports.

### Acknowledgments

This research took place on the lands of the Koyukuk-hotana Athabascans and we are grateful to the Huslia Tribal Council for permitting field access. PCK was supported during this work by the Cohan-Jacobs and Stein Families Fellowship from the Fannie and John Hertz Foundation. This research was also conducted with government support under and awarded by DoD, Air Force Office of Scientific Research, National Defense Science and Engineering Graduate (NDSEG) Fellowship, 32 CFR 168a, to PCK and MD. We acknowledge support from Foster and Coco Stanback, the Linde Family, the Caltech Terrestrial Hazards Observation and Reporting (THOR) Center, NSF Award 2127442 to MPL and WWF, NSF award 2127444 to AJW, and the Caltech Resnick Sustainability Institute to MPL and WWF. We also acknowledge financial support from the Department of Energy (DOE) Office of Science, Biological and Environmental Research (BER), Earth and Environmental Systems Sciences Division (EESD), Subsurface Biogeochemical Research Program Early Career Award to JCR. Support was also provided by Interdisciplinary Research for Arctic Coastal Environments (InterFACE) project through the DOE BER EESSD Regional and Global Model Analysis program. Use of the Stanford Synchrotron Radiation Lightsource, SLAC National Accelerator Laboratory, was supported under Contract No. DE-AC02-76SF00515 by the U.S. Department of Energy, Office of Science, Office of Basic Energy Sciences, and we acknowledge the Polar Geospatial Center for providing a digital elevation model through NSF awards 1043681, 1559691, and 1542736. We thank S. Huffman, A. Atlla, and V. Umphenour for assistance in the field, A. Sessions, F. Wu, and A. Phillips for assistance with EA-IRMS measurements, E. Eitel, S. Bone, N. Edwards, C. Roach, and J. Richardson for assistance with synchrotron measurements, G. Lopez for assistance with MC-ICP-MS measurements, X. Zhang and D. Dettman for measuring the oxygen isotope ratio of sulfate, and the AMS facility at the University of Arizona for measuring dissolved organic carbon isotope ratios. S. Tank and one anonymous reviewer provided insightful critiques on an earlier draft of this article, and the analysis benefited from discussions with J. Adkins.

### References

- Abbott, B. W., Jones, J. B., Schuur, E. A., Chapin, F. S., III, Bowden, W. B., Bret-Harte, M. S., et al. (2016). Biomass offsets little or none of permafrost carbon release from soils, streams, and wildfire: An expert assessment. *Environmental Research Letters*, *11*(3), 034014. <https://doi.org/10.1088/1748-9326/11/3/034014>
- Aharon, P., & Fu, B. (2000). Microbial sulfate reduction rates and sulfur and oxygen isotope fractionations at oil and gas seeps in deepwater Gulf of Mexico. *Geochimica et Cosmochimica Acta*, *64*(2), 233–246. [https://doi.org/10.1016/S0016-7037\(99\)00292-6](https://doi.org/10.1016/S0016-7037(99)00292-6)
- Anisimov, O. A., Shiklomanov, N. I., & Nelson, F. E. (1997). Global warming and active-layer thickness: Results from transient general circulation models. *Global and Planetary Change*, *15*(3–4), 61–77. [https://doi.org/10.1016/S0921-8181\(97\)00009-X](https://doi.org/10.1016/S0921-8181(97)00009-X)
- Antler, G., Turchyn, A. V., Ono, S., Sivan, O., & Bosak, T. (2017). Combined  $^{34}\text{S}$ ,  $^{33}\text{S}$  and  $^{18}\text{O}$  isotope fractionations record different intracellular steps of microbial sulfate reduction. *Geochimica et Cosmochimica Acta*, *203*, 364–380. <https://doi.org/10.1016/j.gca.2017.01.015>
- Antler, G., Turchyn, A. V., Rennie, V., Herut, B., & Sivan, O. (2013). Coupled sulfur and oxygen isotope insight into bacterial sulfate reduction in the natural environment. *Geochimica et Cosmochimica Acta*, *118*, 98–117. <https://doi.org/10.1016/j.gca.2013.05.005>
- Archer, D., Khesghi, H., & Maier-Reimer, E. (1997). Multiple timescales for neutralization of fossil fuel  $\text{CO}_2$ . *Geophysical Research Letters*, *24*(4), 405–408. <https://doi.org/10.1029/97GL00168>
- Aurela, M., Laurila, T., & Tuovinen, J. P. (2004). The timing of snow melt controls the annual  $\text{CO}_2$  balance in a subarctic fen. *Geophysical Research Letters*, *31*(16), L16119. <https://doi.org/10.1029/2004GL020315>
- Balci, N., Shanks, W. C., III, Mayer, B., & Mandernack, K. W. (2007). Oxygen and sulfur isotope systematics of sulfate produced by bacterial and abiotic oxidation of pyrite. *Geochimica et Cosmochimica Acta*, *71*(15), 3796–3811. <https://doi.org/10.1016/j.gca.2007.04.017>
- Barker, A. J., Douglas, T. A., Jacobson, A. D., McClelland, J. W., Ilgen, A. G., Khosh, M. S., et al. (2014). Late season mobilization of trace metals in two small Alaskan arctic watersheds as a proxy for landscape scale permafrost active layer dynamics. *Chemical Geology*, *381*, 180–193. <https://doi.org/10.1016/j.chemgeo.2014.05.012>
- Barnes, R. T., Butman, D. E., Wilson, H. F., & Raymond, P. A. (2018). Riverine export of aged carbon driven by flow path depth and residence time. *Environmental Science & Technology*, *52*(3), 1028–1035. <https://doi.org/10.1021/acs.est.7b04717>
- Beikman, H. M. (1980). Geologic map of Alaska: U.S. Geological Survey, 1 sheet, scale 1:2,500,000.
- Benner, R., Benitez-Nelson, B., Kaiser, K., & Amon, R. M. (2004). Export of young terrigenous dissolved organic carbon from rivers to the Arctic Ocean. *Geophysical Research Letters*, *31*(5). <https://doi.org/10.1029/2003GL019251>
- Bense, V. F., Ferguson, G., & Kooi, H. (2009). Evolution of shallow groundwater flow systems in areas of degrading permafrost. *Geophysical Research Letters*, *36*(22), L22401. <https://doi.org/10.1029/2009GL039225>
- Berner, R. A. (1971). Worldwide sulfur pollution of rivers. *Journal of Geophysical Research*, *76*(27), 6597–6600. <https://doi.org/10.1029/JC076i027p06597>
- Billings, W. D., Luken, J. O., Mortensen, D. A., & Peterson, K. M. (1982). Arctic tundra: A source or sink for atmospheric carbon dioxide in a changing environment? *Oecologia*, *53*(1), 7–11. <https://doi.org/10.1007/BF00377129>
- Biskaborn, B. K., Smith, S. L., Noetzi, J., Matthes, H., Vieira, G., Streletskiy, D. A., et al. (2019). Permafrost is warming at a global scale. *Nature Communications*, *10*(1), 1–11. <https://doi.org/10.1038/s41467-018-08240-4>
- Bohic, S., Murphy, K., Paulus, W., Cloetens, P., Salome, M., Susini, J., & Double, K. (2008). Intracellular chemical imaging of the developmental phases of human neuromelanin using synchrotron X-ray microspectroscopy. *Analytical Chemistry*, *80*(24), 9557–9566. <https://doi.org/10.1021/ac801817k>
- Brabets, T. P., Wang, B., & Meade, R. H. (2000). Environmental and hydrologic overview of the Yukon River Basin, Alaska and Canada. *Water-Resources Investigations Report*, *99*, 4204.
- Broecker, W. S., & Sanyal, A. (1998). Does atmospheric  $\text{CO}_2$  police the rate of chemical weathering? *Global Biogeochemical Cycles*, *12*(3), 403–408. <https://doi.org/10.1029/98GB01927>
- Brown, J., Hinkel, K. M., & Nelson, F. E. (2000). The circumpolar active layer monitoring (CALM) program: Research designs and initial results. *Polar Geography*, *24*(3), 166–258. <https://doi.org/10.1080/10889370009377698>
- Brunner, B., Bernasconi, S. M., Kleikemper, J., & Schroth, M. H. (2005). A model for oxygen and sulfur isotope fractionation in sulfate during bacterial sulfate reduction processes. *Geochimica et Cosmochimica Acta*, *69*(20), 4773–4785. <https://doi.org/10.1016/j.gca.2005.04.017>
- Burke, A., Present, T. M., Paris, G., Rae, E. C., Sandilands, B. H., Gaillardet, J., et al. (2018). Sulfur isotopes in rivers: Insights into global weathering budgets, pyrite oxidation, and the modern sulfur cycle. *Earth and Planetary Science Letters*, *496*, 168–177. <https://doi.org/10.1016/j.epsl.2018.05.022>
- Burt, E. I., Bill, M., Conrad, M. E., Quispe, A. J. C., Christensen, J. N., Hilton, R. G., et al. (2021). Conservative transport of dissolved sulfate across the Rio Madre de Dios floodplain in Peru. *Geology*, *49*(9), 1064–1068. <https://doi.org/10.1130/G48997.1>
- Calmels, D., Gaillardet, J., Brenot, A., & France-Lanord, C. (2007). Sustained sulfide oxidation by physical erosion processes in the Mackenzie River basin: Climatic perspectives. *Geology*, *35*(11), 1003–1006. <https://doi.org/10.1130/G24132A.1>
- Canadell, J. G., Monteiro, P. M. S., Costa, M. H., Cotrim da Cunha, L., Cox, P. M., Eliseev, A. V., et al. (2021). Global carbon and other biogeochemical cycles and feedbacks. In V. Masson-Delmotte, P. Zhai, A. Pirani, S. L. Connors, C. Péan, S. Berger, et al. (Eds.), *Climate change 2021: The physical science basis. Contribution of working group I to the sixth assessment report of the intergovernmental panel on climate change* (pp. 673–816). Cambridge University Press. <https://doi.org/10.1017/9781009157896.007>
- Chapin, F. S., III, Sturm, M., Serreze, M. C., McFadden, J. P., Key, J. R., Lloyd, A. H., et al. (2005). Role of land-surface changes in Arctic summer warming. *Science*, *310*(5748), 657–660. <https://doi.org/10.1126/science.1117368>
- Claudice, K. H., & Mowatt, T. C. (1981). *Trona occurrences within the Yukon Flats Basin, Alaska*. Bureau of Mines, US Department of the Interior. Open File Report No. 69-81.
- Claypool, G. E., Holser, W. T., Kaplan, I. R., Sakai, H., & Zak, I. (1980). The age curves of sulfur and oxygen isotopes in marine sulfate and their mutual interpretation. *Chemical Geology*, *28*, 199–260. [https://doi.org/10.1016/0009-2541\(80\)90047-9](https://doi.org/10.1016/0009-2541(80)90047-9)
- Cleve, K. V., Viereck, L. A., & Marion, G. M. (1993). Introduction and overview of a study dealing with the role of salt-affected soils in primary succession on the Tanana River floodplain, interior Alaska. *Canadian Journal of Forest Research*, *23*(5), 879–888. <https://doi.org/10.1139/x93-116>
- Cole, T. L., Torres, M. A., & Kemeny, P. C. (2022). The hydrochemical signature of incongruent weathering in Iceland. *JGR Earth Surface*, *127*(6), e2021JF006450. <https://doi.org/10.1029/2021JF006450>
- Dornblaser, M. M., & Halm, D. R. (Eds.). (2006). *Water and sediment quality of the Yukon River and its tributaries, from Eagle to St. Marys, Alaska, 2002–2003*. U.S. Geological Survey Open-File Report 2006-1228.

- Douglas, M. M., Li, G. K., Fischer, W. W., Rowland, J. C., Kemeny, P. C., West, A. J., et al. (2022). Organic carbon burial by river meandering partially offsets bank erosion carbon fluxes in a discontinuous permafrost floodplain. *Earth Surface Dynamics*, *10*(3), 421–435. <https://doi.org/10.5194/esurf-10-421-2022>
- Douglas, M. M., Lingappa, U. F., Lamb, M. P., Rowland, J. C., West, A. J., Li, G., et al. (2021). Impact of river channel lateral migration on microbial communities across a discontinuous permafrost floodplain. *Applied and Environmental Microbiology*, *87*(20), e01339-21. <https://doi.org/10.1128/AEM.01339-21>
- Drake, T. W., Guillemette, F., Hemingway, J. D., Chanton, J. P., Podgorski, D. C., Zimov, N. S., & Spencer, R. G. (2018a). The ephemeral signature of permafrost carbon in an Arctic fluvial network. *Journal of Geophysical Research: Biogeosciences*, *123*(5), 1475–1485. <https://doi.org/10.1029/2017JG004311>
- Drake, T. W., Tank, S. E., Zhulidov, A. V., Holmes, R. M., Gurtovaya, T., & Spencer, R. G. (2018b). Increasing alkalinity export from large Russian Arctic rivers. *Environmental Science & Technology*, *52*(15), 8302–8308. <https://doi.org/10.1021/acs.est.8b01051>
- Drake, T. W., Wickland, K. P., Spencer, R. G., McKnight, D. M., & Striegl, R. G. (2015). Ancient low-molecular-weight organic acids in permafrost fuel rapid carbon dioxide production upon thaw. *Proceedings of the National Academy of Sciences*, *112*(45), 13946–13951. <https://doi.org/10.1073/pnas.1511705112>
- Druhan, J. L., & Maher, K. (2014). A model linking stable isotope fractionation to water flux and transit times in heterogeneous porous media. *Procedia Earth and Planetary Science*, *10*, 179–188. <https://doi.org/10.1016/j.proeps.2014.08.054>
- Druhan, J. L., & Maher, K. (2017). The influence of mixing on stable isotope ratios in porous media: A revised Rayleigh model. *Water Resources Research*, *53*(2), 1101–1124. <https://doi.org/10.1002/2016WR019666>
- Drury, W. H. (1956). *Bog flats and physiographic processes in the upper Kuskokwim River region, Alaska* (Vol. 178, pp. 1–130). Contributions from the Gray Herbarium of Harvard University. Retrieved from <https://www.jstor.org/stable/41764811>
- Dyrness, C. T., & Cleve, K. V. (1993). Control of surface soil chemistry in early-successional floodplain soils along the Tanana River, interior Alaska. *Canadian Journal of Forest Research*, *23*(5), 979–994. <https://doi.org/10.1139/x93-126>
- Fike, D. A., Bradley, A. S., & Rose, C. V. (2015). Rethinking the ancient sulfur cycle. *Annual Review of Earth and Planetary Sciences*, *43*(1), 593–622. <https://doi.org/10.1146/annurev-earth-060313-054802>
- Foks, S. S., Dornblaser, M. M., Bogard, M. J., Butman, D., Campbell, D. A., Johnston, S. E., et al. (2020). Water quality and gas fluxes of Interior Alaska (2014–2018): U.S. Geological Survey data release. <https://doi.org/10.5066/P9C6BDBQ>
- Frey, K. E., & McClelland, J. W. (2009). Impacts of permafrost degradation on arctic river biogeochemistry. *Hydrological Processes: An International Journal*, *23*(1), 169–182. <https://doi.org/10.1002/hyp.7196>
- Fritz, P., Basharmal, G. M., Drimmie, R. J., Ibsen, J., & Qureshi, R. M. (1989). Oxygen isotope exchange between sulphate and water during bacterial reduction of sulphate. *Chemical Geology: Isotope Geoscience section*, *79*(2), 99–105. [https://doi.org/10.1016/0168-9622\(89\)90012-2](https://doi.org/10.1016/0168-9622(89)90012-2)
- Gaillardet, J., Dupré, B., Louvat, P., & Allegre, C. J. (1999). Global silicate weathering and CO<sub>2</sub> consumption rates deduced from the chemistry of large rivers. *Chemical Geology*, *159*(1–4), 3–30. [https://doi.org/10.1016/S0009-2541\(99\)00031-5](https://doi.org/10.1016/S0009-2541(99)00031-5)
- Garrels, R. M., & Mackenzie, F. T. (1967). Origin of the chemical compositions of some springs and lakes. <https://doi.org/10.1021/ba-1967-0067.ch010>
- Gislason, S. R., & Torssander, P. (2006). Response of sulfate concentration and isotope composition in Icelandic rivers to the decline in global atmospheric SO<sub>2</sub> emissions into the North Atlantic region. *Environmental Science & Technology*, *40*(3), 680–686. <https://doi.org/10.1021/es051325o>
- Grinenko, V. A., & Ustinov, V. I. (1990). Dynamics of sulfur and oxygen isotope fractionation during bacterial sulfate reduction. *Geokhimiya*, *9*, 1241–1251.
- Grosse, G., Goetz, S., McGuire, A. D., Romanovsky, V. E., & Schuur, E. A. (2016). Changing permafrost in a warming world and feedbacks to the Earth system. *Environmental Research Letters*, *11*(4), 040201. <https://doi.org/10.1088/1748-9326/11/4/040201>
- Halm, D. R., & Dornblaser, M. M. (2007). *Water and sediment quality in the Yukon River and its tributaries between Atlin, British Columbia, Canada, and Eagle, Alaska, USA, 2004. No. 2007-1197*. Geological Survey (US). <https://doi.org/10.3133/ofr20071197>
- Harrison, J. C., St-Onge, M. R., Petrov, O. V., Strel'nikov, S. L., Lopatin, B. G., Wilson, F. H., et al. (2011). Geological map of the Arctic: Geological Survey of Canada Map 2159A. <https://doi.org/10.4095/287868.2/651662>
- Hayes, J. M. (2004). *An introduction to isotopic calculations* (p. 2543). Woods Hole Oceanographic Institution.
- Heijmans, M. M., Magnússon, R. Í., Lara, M. J., Frost, G. V., Myers-Smith, I. H., van Huissteden, J., et al. (2022). Tundra vegetation change and impacts on permafrost. *Nature Reviews Earth & Environment*, *3*(1), 68–84. <https://doi.org/10.1038/s43017-021-00233-0>
- Hemingway, J. D., Olson, H., Turchyn, A. V., Tipper, E. T., Bickle, M. J., & Johnston, D. T. (2020). Triple oxygen isotope insight into terrestrial pyrite oxidation. *Proceedings of the National Academy of Sciences*, *117*(14), 7650–7657. <https://doi.org/10.1073/pnas.1917518117>
- Herman-Mercer, N. M. (2016). Water-quality data from the Yukon River Basin in Alaska and Canada: U.S. Geological Survey data release. <https://doi.org/10.5066/F77D2S7B>
- Hilton, R. G., Gaillardet, J., Calmels, D., & Birck, J. L. (2014). Geological respiration of a mountain belt revealed by the trace element rhenium. *Earth and Planetary Science Letters*, *403*, 27–36. <https://doi.org/10.1016/j.epsl.2014.06.021>
- Hilton, R. G., & West, A. J. (2020). Mountains, erosion and the carbon cycle. *Nature Reviews Earth & Environment*, *1*(6), 284–299. <https://doi.org/10.1038/s43017-020-0058-6>
- Hinkel, K. M., & Nelson, F. E. (2003). Spatial and temporal patterns of active layer thickness at Circumpolar Active Layer Monitoring (CALM) sites in northern Alaska, 1995–2000. *Journal of Geophysical Research*, *108*(D2), 8168. <https://doi.org/10.1029/2001JD000927>
- Hinzman, L. D., Bettez, N. D., Bolton, W. R., Chapin, F. S., Dyurgerov, M. B., Fastie, C. L., et al. (2005). Evidence and implications of recent climate change in northern Alaska and other arctic regions. *Climatic Change*, *72*(3), 251–298. <https://doi.org/10.1007/s10584-005-5352-2>
- Horan, K., Hilton, R. G., Dellinger, M., Tipper, E., Galy, V., Calmels, D., et al. (2019). Carbon dioxide emissions by rock organic carbon oxidation and the net geochemical carbon budget of the Mackenzie River Basin. *American Journal of Science*, *319*(6), 473–499. <https://doi.org/10.2475/06.2019.02>
- Horan, K., Hilton, R. G., Selby, D., Ottley, C. J., Gröcke, D. R., Hicks, M., & Burton, K. W. (2017). Mountain glaciation drives rapid oxidation of rock-bound organic carbon. *Science Advances*, *3*(10), e1701107. <https://doi.org/10.1126/sciadv.1701107>
- Ielpi, A., Lapôtre, M. G., Finotello, A., & Roy-Léveillé, P. (2023). Large sinuous rivers are slowing down in a warming Arctic. *Nature Climate Change*, *13*(4), 1–7. <https://doi.org/10.1038/s41558-023-01620-9>
- Jiang, Y., Zhuang, Q., & O'Donnell, J. A. (2012). Modeling thermal dynamics of active layer soils and near-surface permafrost using a fully coupled water and heat transport model. *Journal of Geophysical Research*, *117*(D11), 1158. <https://doi.org/10.1029/2012JD017512>
- John, S. G., & Adkins, J. F. (2010). Analysis of dissolved iron isotopes in seawater. *Marine Chemistry*, *119*(1–4), 65–76. <https://doi.org/10.1016/j.marchem.2010.01.001>

- Johnson, J. E., Gerpheide, A., Lamb, M. P., & Fischer, W. W. (2014). O<sub>2</sub> constraints from Paleoproterozoic detrital pyrite and uraninite. *Bulletin*, 126(5–6), 813–830. <https://doi.org/10.1130/B30949.1>
- Jones, E. L., Hodson, A. J., Thornton, S. F., Redeker, K. R., Rogers, J., Wynn, P. M., et al. (2020). Biogeochemical processes in the active layer and permafrost of a high Arctic fjord valley. *Frontiers in Earth Science*, 8, 342. <https://doi.org/10.3389/feart.2020.00342>
- Joo, Y. J., Sim, M. S., Elwood Madden, M. E., & Soreghan, G. S. (2022). Significance of the terrestrial sink in the biogeochemical sulfur cycle. *Geophysical Research Letters*, 49(4), e2021GL097009. <https://doi.org/10.1029/2021GL097009>
- Jorgenson, M. T., Douglas, T. A., Liljedahl, A. K., Roth, J. E., Cater, T. C., Davis, W. A., et al. (2020). The roles of climate extremes, ecological succession, and hydrology in repeated permafrost aggradation and degradation in fens on the Tanana Flats, Alaska. *Journal of Geophysical Research: Biogeosciences*, 125(12), e2020JG005824. <https://doi.org/10.1029/2020JG005824>
- Jorgenson, M. T., Harden, J., Kanevskiy, M., O'Donnell, J., Wickland, K., Ewing, S., et al. (2013). Reorganization of vegetation, hydrology and soil carbon after permafrost degradation across heterogeneous boreal landscapes. *Environmental Research Letters*, 8(3), 035017. <https://doi.org/10.1088/1748-9326/8/3/035017>
- Jorgenson, M. T., Racine, C. H., Walters, J. C., & Osterkamp, T. E. (2001). Permafrost degradation and ecological changes associated with a warming climate in central Alaska. *Climatic Change*, 48(4), 551–579. <https://doi.org/10.1023/A:1005667424292>
- Jorgenson, M. T., Shur, Y. L., & Pullman, E. R. (2006). Abrupt increase in permafrost degradation in Arctic Alaska. *Geophysical Research Letters*, 33(2), L02503. <https://doi.org/10.1029/2005GL024960>
- Kanevskiy, M., Jorgenson, T., Shur, Y., O'Donnell, J. A., Harden, J. W., Zhuang, Q., & Fortier, D. (2014). Cryostratigraphy and permafrost evolution in the lacustrine lowlands of west-Central Alaska. *Permafrost and Periglacial Processes*, 25(1), 14–34. <https://doi.org/10.1002/ppp.1800>
- Kang, M., Skierszkan, E., Brennan, S., Fernandez, D. P., Yang, Z., Girard, I., et al. (2022). Controls of lithium isotope spatial variability across the Yukon River: Implications for weathering processes in a warming subarctic basin. *Geochimica et Cosmochimica Acta*, 323, 1–19. <https://doi.org/10.1016/j.gca.2022.02.016>
- Keeling, R. F., Graven, H. D., Welp, L. R., Resplandy, L., Bi, J., Piper, S. C., et al. (2017). Atmospheric evidence for a global secular increase in carbon isotopic discrimination of land photosynthesis. *Proceedings of the National Academy of Sciences*, 114(39), 10361–10366. <https://doi.org/10.1073/pnas.1619240114>
- Keller, K., Blum, J. D., & Kling, G. W. (2007). Geochemistry of soils and streams on surfaces of varying ages in arctic Alaska. *Arctic Antarctic and Alpine Research*, 39(1), 84–98. [https://doi.org/10.1657/1523-0430\(2007\)39\[84:GOSASO\]2.0.CO;2](https://doi.org/10.1657/1523-0430(2007)39[84:GOSASO]2.0.CO;2)
- Keller, K., Blum, J. D., & Kling, G. W. (2010). Stream geochemistry as an indicator of increasing permafrost thaw depth in an arctic watershed. *Chemical Geology*, 273(1–2), 76–81. <https://doi.org/10.1016/j.chemgeo.2010.02.013>
- Kemeny, P. C. (2023). PrestonCosslettKemeny/MEANDIR: September 6, 2023 release (version 1.3) [Software]. Zenodo. <https://doi.org/10.5281/zenodo.8321937>
- Kemeny, P. C., Lopez, G. I., Dalleska, N. F., Torres, M., Burke, A., Bhatt, M. P., et al. (2021a). Sulfate sulfur isotopes and major ion chemistry reveal that pyrite oxidation counteracts CO<sub>2</sub> drawdown from silicate weathering in the Langtang-Trisuli-Narayani River system, Nepal Himalaya. *Geochimica et Cosmochimica Acta*, 294, 43–69. <https://doi.org/10.1016/j.gca.2020.11.009>
- Kemeny, P. C., & Torres, M. A. (2021). Presentation and applications of mixing elements and dissolved isotopes in rivers (MEANDIR), a customizable MATLAB model for Monte Carlo inversion of dissolved river chemistry. *American Journal of Science*, 321(5), 579–642. <https://doi.org/10.2475/05.2021.03>
- Kemeny, P. C., Torres, M. A., Lamb, M. P., Webb, S. M., Dalleska, N., Cole, T., et al. (2021b). Organic sulfur fluxes and geomorphic control of sulfur isotope ratios in rivers. *Earth and Planetary Science Letters*, 562, 116838. <https://doi.org/10.1016/j.epsl.2021.116838>
- Killingsworth, B. A., Bao, H., & Kohl, I. E. (2018). Assessing pyrite-derived sulfate in the Mississippi River with four years of sulfur and triple-oxygen isotope data. *Environmental Science & Technology*, 52(11), 6126–6136. <https://doi.org/10.1021/acs.est.7b05792>
- Kim, H., Stinchcomb, G., & Brantley, S. L. (2017). Feedbacks among O<sub>2</sub> and CO<sub>2</sub> in deep soil gas, oxidation of ferrous minerals, and fractures: A hypothesis for steady-state regolith thickness. *Earth and Planetary Science Letters*, 460, 29–40. <https://doi.org/10.1016/j.epsl.2016.12.003>
- Kokelj, S. V., & Burn, C. R. (2003). Ground ice and soluble cations in near-surface permafrost, Inuvik, Northwest Territories, Canada. *Permafrost and Periglacial Processes*, 14(3), 275–289. <https://doi.org/10.1002/ppp.458>
- Kokelj, S. V., & Burn, C. R. (2005). Geochemistry of the active layer and near-surface permafrost, Mackenzie delta region, Northwest Territories, Canada. *Canadian Journal of Earth Sciences*, 42(1), 37–48. <https://doi.org/10.1139/e04-089>
- Koven, C. D., Riley, W. J., & Stern, A. (2013). Analysis of permafrost thermal dynamics and response to climate change in the CMIP5 Earth System Models. *Journal of Climate*, 26(6), 1877–1900. <https://doi.org/10.1175/JCLI-D-12-00228.1>
- Koven, C. D., Ringeval, B., Friedlingstein, P., Ciais, P., Cadule, P., Khvorostyanov, D., et al. (2011). Permafrost carbon-climate feedbacks accelerate global warming. *Proceedings of the National Academy of Sciences*, 108(36), 14769–14774. <https://doi.org/10.1073/pnas.110391010>
- Kreig, R. A., & Reger, R. D. (1982). *Air-photo analysis and summary of landform soil properties along the route of the Trans-Alaska Pipeline System*. Division of Geological & Geophysical Surveys.
- Lachenbruch, A. H., & Marshall, B. V. (1986). Changing climate: Geothermal evidence from permafrost in the Alaskan Arctic. *Science*, 234(4777), 689–696. <https://doi.org/10.1126/science.234.4777.689>
- Lamontagne-Hallé, P., McKenzie, J. M., Kurylyk, B. L., & Zipper, S. C. (2018). Changing groundwater discharge dynamics in permafrost regions. *Environmental Research Letters*, 13(8), 084017. <https://doi.org/10.1088/1748-9326/aad404>
- Leavitt, W. D., Halevy, I., Bradley, A. S., & Johnston, D. T. (2013). Influence of sulfate reduction rates on the Phanerozoic sulfur isotope record. *Proceedings of the National Academy of Sciences*, 110(28), 11244–11249. <https://doi.org/10.1073/pnas.1218874110>
- Lehn, G. O., Jacobson, A. D., Douglas, T. A., McClelland, J. W., Barker, A. J., & Khosh, M. S. (2017). Constraining seasonal active layer dynamics and chemical weathering reactions occurring in North Slope Alaskan watersheds with major ion and isotope ( $\delta^{34}\text{S}_{\text{SO}_4}$ ,  $\delta^{13}\text{C}_{\text{DIC}}$ ,  $^{87}\text{Sr}/^{86}\text{Sr}$ ,  $\delta^{44/40}\text{Ca}$ , and  $\delta^{44/42}\text{Ca}$ ) measurements. *Geochimica et Cosmochimica Acta*, 217, 399–420. <https://doi.org/10.1016/j.gca.2017.07.042>
- Leonard, A., Castle, S., Burr, G. S., Lange, T., & Thomas, J. (2013). A wet oxidation method for AMS radiocarbon analysis of dissolved organic carbon in water. *Radiocarbon*, 55(2), 545–552. <https://doi.org/10.1017/S003822200057672>
- Lerman, A., Wu, L., & Mackenzie, F. T. (2007). CO<sub>2</sub> and H<sub>2</sub>SO<sub>4</sub> consumption in weathering and material transport to the ocean, and their role in the global carbon balance. *Marine Chemistry*, 106(1–2), 326–350. <https://doi.org/10.1016/j.marchem.2006.04.004>
- Linger, K. B., Wohl, E., & Rose, J. R. (2018). Geomorphic controls on floodplain soil organic carbon in the Yukon Flats, interior Alaska, from reach to river basin scales. *Water Resources Research*, 54(3), 1934–1951. <https://doi.org/10.1002/2017WR022042>
- Liu, J., Wennberg, P. O., Parazoo, N. C., Yin, Y., & Frankenberg, C. (2020). Observational constraints on the response of high-latitude northern forests to warming. *AGU Advances*, 1(4), e2020AV000228. <https://doi.org/10.1029/2020AV000228>
- Lloyd, R. M. (1967). Oxygen-18 composition of oceanic sulfate. *Science*, 156(3779), 1228–1231. <https://doi.org/10.1126/science.156.3779.1228>
- Lloyd, R. M. (1968). Oxygen isotope behavior in the sulfate-water system. *Journal of Geophysical Research*, 73(18), 6099–6110. <https://doi.org/10.1029/JB073i018p06099>



- Lowenstein, T. K., Hardie, L. A., Timofeeff, M. N., & Demicco, R. V. (2003). Secular variation in seawater chemistry and the origin of calcium chloride basinal brines. *Geology*, *31*(10), 857–860. <https://doi.org/10.1130/G19728R.1>
- Lupker, M., France-Lanord, C., Galy, V., Lavé, J., Gaillardet, J., Gajurel, A. P., et al. (2012). Predominant floodplain over mountain weathering of Himalayan sediments (Ganga basin). *Geochimica et Cosmochimica Acta*, *84*, 410–432. <https://doi.org/10.1016/j.gca.2012.02.001>
- Manceau, A., & Nagy, K. L. (2012). Quantitative analysis of sulfur functional groups in natural organic matter by XANES spectroscopy. *Geochimica et Cosmochimica Acta*, *99*, 206–223. <https://doi.org/10.1016/j.gca.2012.09.033>
- Mandernack, K. W., Krouse, H. R., & Skei, J. M. (2003). A stable sulfur and oxygen isotopic investigation of sulfur cycling in an anoxic marine basin, Framvaren Fjord, Norway. *Chemical Geology*, *195*(1–4), 181–200. [https://doi.org/10.1016/S0009-2541\(02\)00394-7](https://doi.org/10.1016/S0009-2541(02)00394-7)
- Mann, D. H., Fastie, C. L., Rowland, E. L., & Bigelow, N. H. (1995). Spruce succession, disturbance, and geomorphology on the Tanana River floodplain, Alaska. *Écoscience*, *2*(2), 184–199. <https://doi.org/10.1080/11956860.1995.11682283>
- Mast, M. A. (2013). Evaluation of stream chemistry trends in US Geological Survey reference watersheds, 1970–2010. *Environmental Monitoring and Assessment*, *185*(11), 9343–9359. <https://doi.org/10.1007/s10661-013-3256-6>
- McGuire, A. D., Lawrence, D. M., Koven, C., Clein, J. S., Burke, E., Chen, G., et al. (2018). Dependence of the evolution of carbon dynamics in the northern permafrost region on the trajectory of climate change. *Proceedings of the National Academy of Sciences*, *115*(15), 3882–3887. <https://doi.org/10.1073/pnas.1719903115>
- Mills, J. V., Antler, G., & Turchyn, A. V. (2016). Geochemical evidence for cryptic sulfur cycling in salt marsh sediments. *Earth and Planetary Science Letters*, *453*, 23–32. <https://doi.org/10.1016/j.epsl.2016.08.001>
- Miner, K. R., Turetsky, M. R., Malina, E., Bartsch, A., Tamminen, J., McGuire, A. D., et al. (2022). Permafrost carbon emissions in a changing Arctic. *Nature Reviews Earth & Environment*, *3*(1), 55–67. <https://doi.org/10.1038/s43017-021-00230-3>
- Mizutani, Y., & Rafter, T. A. (1969). Bacterial fractionation of oxygen isotopes in the reduction of sulphate and in the oxidation of sulphur. *NZJ Sci*, *12*, 60–68.
- Mizutani, Y., & Rafter, T. A. (1973). Isotopic behaviour of sulphate oxygen in the bacterial reduction of sulphate. *Geochemical Journal*, *6*(4), 183–191. <https://doi.org/10.2343/geochemj.6.183>
- Mook, W. G. (1986). <sup>13</sup>C in atmospheric CO<sub>2</sub>. *Netherlands Journal of Sea Research*, *20*(2–3), 211–223. [https://doi.org/10.1016/0077-7579\(86\)90043-8](https://doi.org/10.1016/0077-7579(86)90043-8)
- Myers-Smith, I. H., Kerby, J. T., Phoenix, G. K., Bjerke, J. W., Epstein, H. E., Assmann, J. J., et al. (2020). Complexity revealed in the greening of the Arctic. *Nature Climate Change*, *10*(2), 106–117. <https://doi.org/10.1038/s41558-019-0688-1>
- Myneni, R. B., Keeling, C. D., Tucker, C. J., Asrar, G., & Nemani, R. R. (1997). Increased plant growth in the northern high latitudes from 1981 to 1991. *Nature*, *386*(6626), 698–702. <https://doi.org/10.1038/386698a0>
- Neff, J. C., Finlay, J. C., Zimov, S. A., Davydov, S. P., Carrasco, J. J., Schuur, E. A. G., & Davydova, A. I. (2006). Seasonal changes in the age and structure of dissolved organic carbon in Siberian rivers and streams. *Geophysical Research Letters*, *33*(23), L23401. <https://doi.org/10.1029/2006GL028222>
- Négrel, P., Allègre, C. J., Dupré, B., & Lewin, E. (1993). Erosion sources determined by inversion of major and trace element ratios and strontium isotopic ratios in river water: The Congo basin case. *Earth and Planetary Science Letters*, *120*(1–2), 59–76. [https://doi.org/10.1016/0012-821X\(93\)90023-3](https://doi.org/10.1016/0012-821X(93)90023-3)
- Nelson, F. E., Shiklomanov, N. I., & Nyland, K. E. (2021). Cool, CALM, collected: The circumpolar active layer monitoring program and network. *Polar Geography*, *44*(3), 155–166. <https://doi.org/10.1080/1088937X.2021.1988001>
- Obu, J. (2021). How much of the earth's surface is underlain by permafrost? *Journal of Geophysical Research: Earth Surface*, *126*(5), e2021JF006123. <https://doi.org/10.1029/2021JF006123>
- Obu, J., Westermann, S., Bartsch, A., Berdnikov, N., Christiansen, H. H., Dashtseren, A., et al. (2019). Northern Hemisphere permafrost map based on TTOP modelling for 2000–2016 at 1 km<sup>2</sup> scale. *Earth-Science Reviews*, *193*, 299–316. <https://doi.org/10.1016/j.earscirev.2019.04.023>
- O'Donnell, J. A., Jorgenson, M. T., Harden, J. W., McGuire, A. D., Kanevskiy, M. Z., & Wickland, K. P. (2012). The effects of permafrost thaw on soil hydrologic, thermal, and carbon dynamics in an Alaskan peatland. *Ecosystems*, *15*(2), 213–229. <https://doi.org/10.1007/s10021-011-9504-0>
- Oechel, W. C., Hastings, S. J., Vourlitis, G., Jenkins, M., Riechers, G., & Grulke, N. (1993). Recent change of Arctic tundra ecosystems from a net carbon dioxide sink to a source. *Nature*, *361*(6412), 520–523. <https://doi.org/10.1038/361520a0>
- Olefeldt, D., Goswami, S., Grosse, G., Hayes, D., Hugelius, G., Kuhry, P., et al. (2016). Circumpolar distribution and carbon storage of thermokarst landscapes. *Nature Communications*, *7*(1), 1–11. <https://doi.org/10.1038/ncomms13043>
- Osterkamp, T. E., & Romanovsky, V. E. (1999). Evidence for warming and thawing of discontinuous permafrost in Alaska. *Permafrost and Periglacial Processes*, *10*(1), 17–37. [https://doi.org/10.1002/\(SICI\)1099-1530\(199901/03\)10:1<17::AID-PPP303>3.0.CO;2-4](https://doi.org/10.1002/(SICI)1099-1530(199901/03)10:1<17::AID-PPP303>3.0.CO;2-4)
- Osterkamp, T. E., Viereck, L., Shur, Y., Jorgenson, M. T., Racine, C., Doyle, A., & Boone, R. D. (2000). Observations of thermokarst and its impact on boreal forests in Alaska, USA. *Arctic Antarctic and Alpine Research*, *32*(3), 303–315. <https://doi.org/10.1080/15230430.2000.12003368>
- Paris, G., Adkins, J. F., Sessions, A. L., Webb, S. M., & Fischer, W. W. (2014). Neoproterozoic carbonate-associated sulfate records positive  $\Delta^{33}\text{S}$  anomalies. *Science*, *346*(6210), 739–741. <https://doi.org/10.1126/science.1258211>
- Paris, G., Sessions, A. L., Subhas, A. V., & Adkins, J. F. (2013). MC-ICP-MS measurement of  $\delta^{34}\text{S}$  and  $\Delta^{33}\text{S}$  in small amounts of dissolved sulfate. *Chemical Geology*, *345*, 50–61. <https://doi.org/10.1016/j.chemgeo.2013.02.022>
- Parkhurst, D. L., & Appelo, C. A. J. (2013). Description of input and examples for PHREEQC version 3—A computer program for speciation, batch-reaction, one-dimensional transport, and inverse geochemical calculations. *US Geological Survey Techniques and Methods*, *6*(A43), 497.
- Patton, W. W., Wilson, F. H., Labay, K. A., & Shew, N. (2009). *Geologic map of the Yukon-Koyukuk basin, Alaska*. US Department of the Interior, US Geological Survey.
- Polsenaere, P., & Abril, G. (2012). Modelling CO<sub>2</sub> degassing from small acidic rivers using water pCO<sub>2</sub>, DIC and  $\delta^{13}\text{C}$ -DIC data. *Geochimica et Cosmochimica Acta*, *91*, 220–239. <https://doi.org/10.1016/j.gca.2012.05.030>
- Prietzl, J., Botzaki, A., Tyufekchieva, N., Brettholle, M., Thieme, J., & Klysubun, W. (2011). Sulfur speciation in soil by S K-edge XANES spectroscopy: Comparison of spectral deconvolution and linear combination fitting. *Environmental Science & Technology*, *45*(7), 2878–2886. <https://doi.org/10.1021/es102180a>
- Rafter, T. A., & Mizutani, Y. (1967). Oxygen isotopic composition of sulphates. Part 2. Preliminary results on oxygen isotopic variation in sulphates and the relationship to their environment and to their  $\delta^{34}\text{S}$  values. *NZJ Science*, *10*, 816–840.
- Randerson, J. T., Liu, H., Flanner, M. G., Chambers, S. D., Jin, Y., Hess, P. G., et al. (2006). The impact of boreal forest fire on climate warming. *Science*, *314*(5802), 1130–1132. <https://doi.org/10.1126/science.1132075>
- Reeburgh, W. S., & Whalen, S. C. (1992). *High-latitude ecosystems as CH<sub>4</sub> sources* (pp. 62–70). Ecological Bulletins. Retrieved from <https://www.jstor.org/stable/20113106>

- Rolph, K. E., Stevenson, E. I., Turchyn, A. V., Antler, G., Bickle, M. J., Baronas, J. J., et al. (2021). Partitioning riverine sulfate sources using oxygen and sulfur isotopes: Implications for carbon budgets of large rivers. *Earth and Planetary Science Letters*, 567, 116957. <https://doi.org/10.1016/j.epsl.2021.116957>
- Rowland, J., Stauffer, S., & Schwenk, J. (2019). Pan-arctic river bank erosion and accretion, and planform metrics measured over intervals ranging from 1973 to 2016. In *Environmental system science data infrastructure for a virtual ecosystem; incorporating the hydrological controls on carbon cycling in floodplain ecosystems into Earth system models (ESMs)*. <https://doi.org/10.15485/1571527>
- Rowland, J. C., Schwenk, J. P., Shelef, E., Muss, J., Ahrens, D., Stauffer, S., et al. (2023). Scale-dependent influence of permafrost on riverbank erosion rates. *Journal of Geophysical Research: Earth Surface*, 128(7), e2023JF007101. <https://doi.org/10.1029/2023JF007101>
- Schuster, P. F. (2003). Water and sediment quality in the Yukon River Basin, Alaska, during water year 2001: U.S. Geological Survey Open-File Report 03-427 (p. 120). Retrieved from <https://pubs.usgs.gov/of/2003/of03427/>
- Schuster, P. F. (2005a). Water and sediment quality in the Yukon River Basin, Alaska, during water year 2002: U.S. Geological Survey Open-File Report 2005-1199 (p. 82). Retrieved from <https://pubs.usgs.gov/of/2005/1199/>
- Schuster, P. F. (2005b). Water and sediment quality in the Yukon River Basin, Alaska, during water year 2003: U.S. Geological Survey Open-File Report 2005-1397 (p. 74). Retrieved from <https://pubs.usgs.gov/of/2005/1397/>
- Schuster, P. F. (2006). Water and sediment quality in the Yukon River Basin, Alaska, during water year 2004: U.S. Geological Survey Open-File Report 2006-1258 (p. 67). Retrieved from <https://pubs.usgs.gov/of/2006/1258/>
- Schuster, P. F. (2007). Water and sediment quality in the Yukon River Basin, Alaska, during water year 2005: U.S. Geological Survey Open-File Report 2007-1037 (p. 65). Retrieved from <https://pubs.usgs.gov/of/2007/1037/>
- Schuster, P. F., Maracle, K. T. B., & Herman-Mercer, N. (2010). *Water quality in the Yukon River Basin, Alaska, water years 2006–2008*. U. S. Geological Survey Open-File Report 2010-1241. Retrieved from <https://pubs.usgs.gov/of/2010/1241/>
- Schuur, E. A., Abbott, B. W., Bowden, W. B., Brovkin, V., Camill, P., Canadell, J. G., et al. (2013). Expert assessment of vulnerability of permafrost carbon to climate change. *Climatic Change*, 119(2), 359–374. <https://doi.org/10.1007/s10584-013-0730-7>
- Schuur, E. A., Bockheim, J., Canadell, J. G., Euskirchen, E., Field, C. B., Goryachkin, S. V., et al. (2008). Vulnerability of permafrost carbon to climate change: Implications for the global carbon cycle. *BioScience*, 58(8), 701–714. <https://doi.org/10.1641/B580807>
- Schuur, E. A., Bracho, R., Celis, G., Belshe, E. F., Ebert, C., Ledman, J., et al. (2021). Tundra underlain by thawing permafrost persistently emits carbon to the atmosphere over 15 years of measurements. *Journal of Geophysical Research: Biogeosciences*, 126(6), e2020JG006044. <https://doi.org/10.1029/2020JG006044>
- Schuur, E. A., McGuire, A. D., Schädel, C., Grosse, G., Harden, J. W., Hayes, D. J., et al. (2015). Climate change and the permafrost carbon feedback. *Nature*, 520(7546), 171–179. <https://doi.org/10.1038/nature14338>
- Schuur, E. A., Vogel, J. G., Crummer, K. G., Lee, H., Sickman, J. O., & Osterkamp, T. E. (2009). The effect of permafrost thaw on old carbon release and net carbon exchange from tundra. *Nature*, 459(7246), 556–559. <https://doi.org/10.1038/nature08031>
- Schwab, M. S., Hilton, R. G., Raymond, P. A., Haghpor, N., Amos, E., Tank, S. E., et al. (2020). An abrupt aging of dissolved organic carbon in large Arctic rivers. *Geophysical Research Letters*, 47(23), e2020GL088823. <https://doi.org/10.1029/2020GL088823>
- Serreze, M. C., Walsh, J. E., Chapin, F. S., Osterkamp, T., Dyurgerov, M., Romanovsky, V., et al. (2000). Observational evidence of recent change in the northern high-latitude environment. *Climatic Change*, 46(1), 159–207. <https://doi.org/10.1023/A:1005504031923>
- Shiklomanov, N. I., Streletskiy, D. A., & Nelson, F. E. (2012). Northern hemisphere component of the global circumpolar active layer monitoring (CALM) program. In *Proceedings of the 10th international conference on permafrost* (Vol. 1, pp. 377–382).
- Sim, M. S., Bosak, T., & Ono, S. (2011). Large sulfur isotope fractionation does not require disproportionation. *Science*, 333(6038), 74–77. <https://doi.org/10.1126/science.1205103>
- Sim, M. S., Ono, S., Donovan, K., Templer, S. P., & Bosak, T. (2011). Effect of electron donors on the fractionation of sulfur isotopes by a marine *Desulfovibrio* sp. *Geochimica et Cosmochimica Acta*, 75(15), 4244–4259. <https://doi.org/10.1016/j.gca.2011.05.021>
- Spence, J., & Telmer, K. (2005). The role of sulfur in chemical weathering and atmospheric CO<sub>2</sub> fluxes: Evidence from major ions, δ<sup>13</sup>C<sub>DIC</sub>, and δ<sup>34</sup>S<sub>SO<sub>4</sub></sub> in rivers of the Canadian Cordillera. *Geochimica et Cosmochimica Acta*, 69(23), 5441–5458. <https://doi.org/10.1016/j.gca.2005.07.011>
- Streletskiy, D. A., Shiklomanov, N. I., Nelson, F. E., & Klene, A. E. (2008). Thirteen years of observations at Alaskan CALM sites: Long-term active layer and ground surface temperature trends. In *Proceedings of the ninth international conference on permafrost, June 29–July 3, 2008, Fairbanks, Alaska* (Vol. 2, pp. 1727–1732). Institute of Northern Engineering, University of Alaska Fairbanks.
- Striegl, R. G., Dornblaser, M. M., Aiken, G. R., Wickland, K. P., & Raymond, P. A. (2007). Carbon export and cycling by the Yukon, Tanana, and Porcupine rivers, Alaska, 2001–2005. *Water Resources Research*, 43(2), W02411. <https://doi.org/10.1029/2006WR005201>
- Sturm, M., Racine, C., & Tape, K. (2001). Increasing shrub abundance in the Arctic. *Nature*, 411(6837), 546–547. <https://doi.org/10.1038/35079180>
- Subhas, A. V., Rollins, N. E., Berelson, W. M., Dong, S., Erez, J., & Adkins, J. F. (2015). A novel determination of calcite dissolution kinetics in seawater. *Geochimica et Cosmochimica Acta*, 170, 51–68. <https://doi.org/10.1016/j.gca.2015.08.011>
- Tank, S. E., Frey, K. E., Striegl, R. G., Raymond, P. A., Holmes, R. M., McClelland, J. W., & Peterson, B. J. (2012a). Landscape-level controls on dissolved carbon flux from diverse catchments of the circumboreal. *Global Biogeochemical Cycles*, 26(4), GB0E02. <https://doi.org/10.1029/2012GB004299>
- Tank, S. E., McClelland, J. W., Spencer, R. G., Shiklomanov, A. I., Suslova, A., Moatar, F., et al. (2023). Recent trends in the chemistry of major northern rivers signal widespread Arctic change. *Nature Geoscience*, 16(9), 1–8. <https://doi.org/10.1038/s41561-023-01247-7>
- Tank, S. E., Raymond, P. A., Striegl, R. G., McClelland, J. W., Holmes, R. M., Fiske, G. J., & Peterson, B. J. (2012b). A land-to-ocean perspective on the magnitude, source and implication of DIC flux from major Arctic rivers to the Arctic Ocean. *Global Biogeochemical Cycles*, 26(4), GB4018. <https://doi.org/10.1029/2011GB004192>
- Tank, S. E., Striegl, R. G., McClelland, J. W., & Kokelj, S. V. (2016). Multi-decadal increases in dissolved organic carbon and alkalinity flux from the Mackenzie drainage basin to the Arctic Ocean. *Environmental Research Letters*, 11(5), 054015. <https://doi.org/10.1088/1748-9326/11/5/054015>
- Tape, K. E. N., Sturm, M., & Racine, C. (2006). The evidence for shrub expansion in Northern Alaska and the Pan-Arctic. *Global Change Biology*, 12(4), 686–702. <https://doi.org/10.1111/j.1365-2486.2006.01128.x>
- Taylor, B. E., Wheeler, M. C., & Nordstrom, D. K. (1984a). Isotope composition of sulphate in acid mine drainage as measure of bacterial oxidation. *Nature*, 308(5959), 538–541. <https://doi.org/10.1038/308538a0>
- Taylor, B. E., Wheeler, M. C., & Nordstrom, D. K. (1984b). Stable isotope geochemistry of acid mine drainage: Experimental oxidation of pyrite. *Geochimica et Cosmochimica Acta*, 48(12), 2669–2678. [https://doi.org/10.1016/0016-7037\(84\)90315-6](https://doi.org/10.1016/0016-7037(84)90315-6)
- Tcherkez, G., & Tea, I. (2013). <sup>32</sup>S/<sup>34</sup>S isotope fractionation in plant sulphur metabolism. *New Phytologist*, 200(1), 44–53. <https://doi.org/10.1111/nph.12314>
- Till, A. B., Dumoulin, J. A., Harris, A. G., Moore, T. E., Bleick, H. A., & Siwec, B. R. (2008). Bedrock geologic map of the southern Brooks Range, Alaska, and accompanying conodont data: U.S. Geological Survey Open-File Report 2008-1149, 88 p., 2 sheets, sheet 1-scale 1:500,000, sheet 2-scale 1:600,000.

- Tipper, E. T., Bickle, M. J., Galy, A., West, A. J., Pomiès, C., & Chapman, H. J. (2006). The short term climatic sensitivity of carbonate and silicate weathering fluxes: Insight from seasonal variations in river chemistry. *Geochimica et Cosmochimica Acta*, 70(11), 2737–2754. <https://doi.org/10.1016/j.gca.2006.03.005>
- Toohey, R. C., Herman-Mercer, N. M., Schuster, P. F., Mutter, E. A., & Koch, J. C. (2016). Multidecadal increases in the Yukon River Basin of chemical fluxes as indicators of changing flowpaths, groundwater, and permafrost. *Geophysical Research Letters*, 43(23), 12–120. <https://doi.org/10.1002/2016GL070817>
- Torres, M. A., Kemeny, P. C., Lamb, M. P., Cole, T. L., & Fischer, W. W. (2020). Long-term storage and age-biased export of fluvial organic carbon: Field evidence from west Iceland. *Geochemistry, Geophysics, Geosystems*, 21(4), e2019GC008632. <https://doi.org/10.1029/2019GC008632>
- Torres, M. A., West, A. J., & Clark, K. E. (2015). Geomorphic regime modulates hydrologic control of chemical weathering in the Andes–Amazon. *Geochimica et Cosmochimica Acta*, 166, 105–128. <https://doi.org/10.1016/j.gca.2015.06.007>
- Torres, M. A., West, A. J., Clark, K. E., Paris, G., Bouchez, J., Ponton, C., et al. (2016). The acid and alkalinity budgets of weathering in the Andes–Amazon system: Insights into the erosional control of global biogeochemical cycles. *Earth and Planetary Science Letters*, 450, 381–391. <https://doi.org/10.1016/j.epsl.2016.06.012>
- Torres, M. A., West, A. J., & Li, G. (2014). Sulphide oxidation and carbonate dissolution as a source of CO<sub>2</sub> over geological timescales. *Nature*, 507(7492), 346–349. <https://doi.org/10.1038/nature13030>
- Trust, B. A., & Fry, B. (1992). Stable sulphur isotopes in plants: A review. *Plant, Cell and Environment*, 15(9), 1105–1110. <https://doi.org/10.1111/j.1365-3040.1992.tb01661.x>
- Turchyn, A. V., Brüchert, V., Lyons, T. W., Engel, G. S., Balci, N., Schrag, D. P., & Brunner, B. (2010). Kinetic oxygen isotope effects during dissimilatory sulfate reduction: A combined theoretical and experimental approach. *Geochimica et Cosmochimica Acta*, 74(7), 2011–2024. <https://doi.org/10.1016/j.gca.2010.01.004>
- Turchyn, A. V., Tipper, E. T., Galy, A., Lo, J. K., & Bickle, M. J. (2013). Isotope evidence for secondary sulfide precipitation along the Marsyandi River, Nepal, Himalayas. *Earth and Planetary Science Letters*, 374, 36–46. <https://doi.org/10.1016/j.epsl.2013.04.033>
- Turetsky, M. R., Abbott, B. W., Jones, M. C., Anthony, K. W., Olefeldt, D., Schuur, E. A., et al. (2020). Carbon release through abrupt permafrost thaw. *Nature Geoscience*, 13(2), 138–143. <https://doi.org/10.1038/s41561-019-0526-0>
- van Everdingen, R. O., & Krouse, H. R. (1985). Isotope composition of sulphates generated by bacterial and abiological oxidation. *Nature*, 315(6018), 395–396. <https://doi.org/10.1038/315395a0>
- van Geldern, R., & Barth, J. A. (2012). Optimization of instrument setup and post-run corrections for oxygen and hydrogen stable isotope measurements of water by isotope ratio infrared spectroscopy (IRIS). *Limnology and Oceanography: Methods*, 10(12), 1024–1036. <https://doi.org/10.4319/lom.2012.10.1024>
- van Stempvoort, D. R., Spoelstra, J., Bickerton, G., Koehler, G., Mayer, B., Nightingale, M., & Miller, J. (2023). Sulfate in streams and groundwater in a cold region (Yukon Territory, Canada): Evidence of weathering processes in a changing climate. *Chemical Geology*, 631, 121510. <https://doi.org/10.1016/j.chemgeo.2023.121510>
- Vonk, J. E., Mann, P. J., Davydov, S., Davydova, A., Spencer, R. G., Schade, J., et al. (2013). High biolability of ancient permafrost carbon upon thaw. *Geophysical Research Letters*, 40(11), 2689–2693. <https://doi.org/10.1002/grl.50348>
- Waelbroeck, C., Monfray, P., Oechel, W. C., Hastings, S., & Vourlitis, G. (1997). The impact of permafrost thawing on the carbon dynamics of tundra. *Geophysical Research Letters*, 24(3), 229–232. <https://doi.org/10.1029/97GL00071>
- Waldeck, A. R., Cowie, B. R., Bertran, E., Wing, B. A., Halevy, I., & Johnston, D. T. (2019). Deciphering the atmospheric signal in marine sulfate oxygen isotope composition. *Earth and Planetary Science Letters*, 522, 12–19. <https://doi.org/10.1016/j.epsl.2019.06.013>
- Walker, M. D., Wahren, C. H., Hollister, R. D., Henry, G. H., Ahlquist, L. E., Alatalo, J. M., et al. (2006). Plant community responses to experimental warming across the tundra biome. *Proceedings of the National Academy of Sciences*, 103(5), 1342–1346. <https://doi.org/10.1073/pnas.0503198103>
- Walvoord, M. A., & Kurylyk, B. L. (2016). Hydrologic impacts of thawing permafrost—A review. *Vadose Zone Journal*, 15(6), 1–20. <https://doi.org/10.2136/vzj2016.01.0010>
- Walvoord, M. A., & Striegl, R. G. (2007). Increased groundwater to stream discharge from permafrost thawing in the Yukon River basin: Potential impacts on lateral export of carbon and nitrogen. *Geophysical Research Letters*, 34(12), L12402. <https://doi.org/10.1029/2007GL030216>
- Webb, S. M. (2005). SIXpack: A graphical user interface for XAS analysis using IFEFFIT. *Physica Scripta*, 2005(T115), 1011. <https://doi.org/10.1238/physica.topical.115a01011>
- Webb, S. M. (2020). SIXPACK: A graphical user interface for XAS analysis. *International Tables for Crystallography*. <https://doi.org/10.1107/S1574870720003456>
- Wilson, F. H., Hults, C. P., Mull, C. G., & Karl, S. M. (2015). Geologic map of Alaska: U.S. Geological Survey Scientific Investigations Map 3340, pamphlet 196 p., 2 sheets, scale 1:1,584,000. <https://doi.org/10.3133/sim3340>
- Wolfe, S., Bond, J., & Lamothe, M. (2011). Dune stabilization in central and southern Yukon in relation to early Holocene environmental change, northwestern North America. *Quaternary Science Reviews*, 30(3–4), 324–334. <https://doi.org/10.1016/j.quascirev.2010.11.010>
- Woo, M. K. (1986). Permafrost hydrology in North America. *Atmosphere-Ocean*, 24(3), 201–234. <https://doi.org/10.1080/07055900.1986.9649248>
- Yi, Y., Kimball, J. S., Chen, R. H., Moghaddam, M., Reichle, R. H., Mishra, U., et al. (2018). Characterizing permafrost active layer dynamics and sensitivity to landscape spatial heterogeneity in Alaska. *The Cryosphere*, 12(1), 145–161. <https://doi.org/10.5194/tc-12-145-2018>
- Zeebe, R. E., & Wolf-Gladrow, D. (2001). *CO<sub>2</sub> in seawater: Equilibrium, kinetics, isotopes (no. 65)*. Gulf Professional Publishing.
- Zolkos, S., Tank, S. E., & Kokelj, S. V. (2018). Mineral weathering and the permafrost carbon-climate feedback. *Geophysical Research Letters*, 45(18), 9623–9632. <https://doi.org/10.1029/2018GL078748>
- Zolkos, S., Tank, S. E., Striegl, R. G., & Kokelj, S. V. (2019). Thermokarst effects on carbon dioxide and methane fluxes in streams on the Peel Plateau (NWT, Canada). *Journal of Geophysical Research: Biogeosciences*, 124(7), 1781–1798. <https://doi.org/10.1029/2019JG005038>

## References From the Supporting Information

- Bataille, C. P., Brennan, S. R., Hartmann, J., Moosdorf, N., Wooller, M. J., & Bowen, G. J. (2014). A geostatistical framework for predicting variations in strontium concentrations and isotope ratios in Alaskan rivers. *Chemical Geology*, 389, 1–15. <https://doi.org/10.1016/j.chemgeo.2014.08.030>
- Blum, J. D., Gazis, C. A., Jacobson, A. D., & Page Chamberlain, C. (1998). Carbonate versus silicate weathering in the Raikhot watershed within the high himalayan crystalline series. *Geology*, 26(5), 411–414. [https://doi.org/10.1130/0091-7613\(1998\)0262.3.CO;2](https://doi.org/10.1130/0091-7613(1998)0262.3.CO;2)

- Brennan, S. R., Fernandez, D. P., Mackey, G., Cerling, T. E., Bataille, C. P., Bowen, G. J., & Wooller, M. J. (2014). Strontium isotope variation and carbonate versus silicate weathering in rivers from across Alaska: Implications for provenance studies. *Chemical Geology*, 389, 167–181. <https://doi.org/10.1016/j.chemgeo.2014.08.018>
- Cooper, R. J., Wadham, J. L., Tranter, M., Hodgkins, R., & Peters, N. E. (2002). Groundwater hydrochemistry in the active layer of the proglacial zone, Finsterwalderbreen, Svalbard. *Journal of Hydrology*, 269(3–4), 208–223. [https://doi.org/10.1016/S0022-1694\(02\)00279-2](https://doi.org/10.1016/S0022-1694(02)00279-2)
- Douglas, T. A., Blum, J. D., Guo, L., Keller, K., & Gleason, J. D. (2013). Hydrogeochemistry of seasonal flow regimes in the Chena River, a subarctic watershed draining discontinuous permafrost in interior Alaska (USA). *Chemical Geology*, 335, 48–62. <https://doi.org/10.1016/j.chemgeo.2012.10.045>
- Edmond, J. M. (1992). Himalayan tectonics, weathering processes, and the strontium isotope record in marine limestones. *Science*, 258(5088), 1594–1597. <https://doi.org/10.1126/science.258.5088.1594>
- Gooseff, M. N., McKnight, D. M., Lyons, W. B., & Blum, A. E. (2002). Weathering reactions and hyporheic exchange controls on stream water chemistry in a glacial meltwater stream in the McMurdo Dry Valleys. *Water Resources Research*, 38(12), 15-1–15-17. <https://doi.org/10.1029/2001WR000834>
- Lopez, C. L., Brouchkov, A., Nakayama, H., Takakai, F., Fedorov, A. N., & Fukuda, M. (2007). Epigenetic salt accumulation and water movement in the active layer of central Yakutia in eastern Siberia. *Hydrological Processes: An International Journal*, 21(1), 103–109. <https://doi.org/10.1002/hyp.6224>
- MacLean, R., Oswood, M. W., Irons, J. G., & McDowell, W. H. (1999). The effect of permafrost on stream biogeochemistry: A case study of two streams in the Alaskan (USA) taiga. *Biogeochemistry*, 47(3), 239–267. <https://doi.org/10.1007/BF00992909>
- Maher, K., & Chamberlain, C. P. (2014). Hydrologic regulation of chemical weathering and the geologic carbon cycle. *Science*, 343(6178), 1502–1504. <https://doi.org/10.1126/science.1250770>
- Maher, K., & Druhan, J. (2014). Relationships between the transit time of water and the fluxes of weathered elements through the critical zone. *Procedia Earth and Planetary Science*, 10, 16–22. <https://doi.org/10.1016/j.proeps.2014.08.004>
- Petrone, K. C., Jones, J. B., Hinzman, L. D., & Boone, R. D. (2006). Seasonal export of carbon, nitrogen, and major solutes from Alaskan catchments with discontinuous permafrost. *Journal of Geophysical Research*, 111(G2), G04003. <https://doi.org/10.1029/2005JG000055>
- Petrone, K. C., Hinzman, L. D., Shibata, H., Jones, J. B., & Boone, R. D. (2007). The influence of fire and permafrost on sub-arctic stream chemistry during storms. *Hydrological Processes: An International Journal*, 21(4), 423–434. <https://doi.org/10.1002/hyp.6247>
- Rutter, N., Hodson, A., Irvine-Fynn, T., & Solås, M. K. (2011). Hydrology and hydrochemistry of a deglaciating high-Arctic catchment, Svalbard. *Journal of Hydrology*, 410(1–2), 39–50. <https://doi.org/10.1016/j.jhydrol.2011.09.001>
- Shields, G. A., & Mills, B. J. (2021). Evaporite weathering and deposition as a long-term climate forcing mechanism. *Geology*, 49(3), 299–303. <https://doi.org/10.1130/G48146.1>
- Wadham, J. L., Cooper, R. J., Tranter, M., & Hodgkins, R. (2001). Enhancement of glacial solute fluxes in the proglacial zone of a polythermal glacier. *Journal of Glaciology*, 47(158), 378–386. <https://doi.org/10.3189/172756501781832188>
- West, A. J., Galy, A., & Bickle, M. (2005). Tectonic and climatic controls on silicate weathering. *Earth and Planetary Science Letters*, 235(1–2), 211–228. <https://doi.org/10.1016/j.epsl.2005.03.020>
- White, A. F., Bullen, T. D., Vivit, D. V., Schulz, M. S., & Clow, D. W. (1999). The role of disseminated calcite in the chemical weathering of granitoid rocks. *Geochimica et Cosmochimica Acta*, 63(13–14), 1939–1953. [https://doi.org/10.1016/S0016-7037\(99\)00082-4](https://doi.org/10.1016/S0016-7037(99)00082-4)